

# Two-phase flow phenomena in hydraulic turbines and pump-turbines operating in synchronous condenser mode

THÈSE N° 8740 (2018)

PRÉSENTÉE LE 31 AOÛT 2018

À LA FACULTÉ DES SCIENCES ET TECHNIQUES DE L'INGÉNIEUR  
LABORATOIRE DE MACHINES HYDRAULIQUES  
PROGRAMME DOCTORAL EN MÉCANIQUE

ÉCOLE POLYTECHNIQUE FÉDÉRALE DE LAUSANNE

POUR L'OBTENTION DU GRADE DE DOCTEUR ÈS SCIENCES

PAR

Elena VAGNONI

acceptée sur proposition du jury:

Prof. D. Pioletti, président du jury  
Prof. F. Avellan, Dr L. Andolfatto, directeurs de thèse  
Prof. J. Katz, rapporteur  
Prof. G. Cavazzini, rapporteuse  
Prof. F. Gallaire, rapporteur



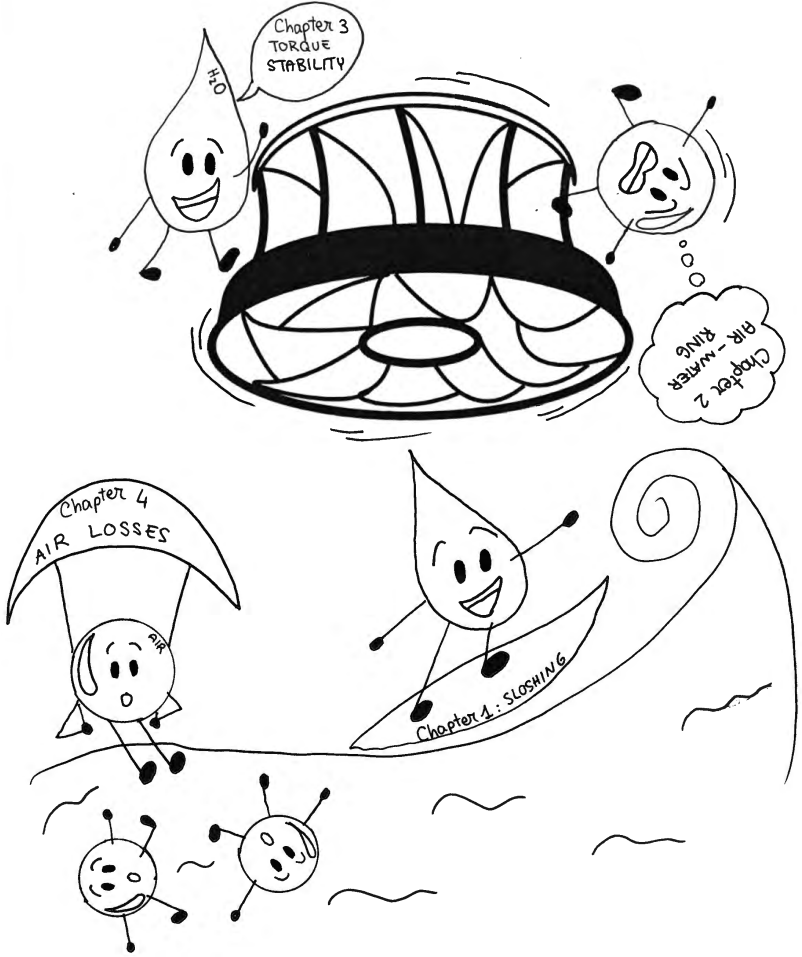
ÉCOLE POLYTECHNIQUE  
FÉDÉRALE DE LAUSANNE

Suisse  
2018



*There is a vitality, a life force, an energy, a quickening that is translated through you into action,  
and because there is only one of you in all time, this expression is unique.  
If you block it, it will never exist through any other medium and will be lost.*

— Martha Graham







# Acknowledgements

Everybody says, "*The first impression is the last impression*". When I first arrived in Lausanne it was a rainy day, and I didn't have an umbrella; I was sick, and I had my job interview to get the PhD position; it was late night, and I didn't find the road of the place where I was staying. But actually, Lausanne turned out to be one of the best places where I have ever lived, especially thanks to the wonderful people I met here.

I'm sincerely grateful to my thesis director, Prof. François Avellan, for giving me the opportunity of conducting my doctoral thesis under his supervision and for granting me his support and trust. Your knowledge and incentives have been a driving force for my thesis.

My profound gratitude to my thesis co-director Dr. Loïc Andolfatto, for his significant contribution to my PhD thesis. Loïc, thank you very much for your precious advice which step by step guides my improvements in research.

It is my pleasure to thank the jury members of my thesis defense, Prof. François Gallaire, Prof. Giovanna Cavazzini, Prof. Joseph Katz and Prof. Dominique Pioletti, for the time and dedication they spent in reading my thesis, for the constructive suggestions and the enriching discussions held during the defense.

Thanks to GE Renewable Energy for the financial support and for giving me the opportunity to perform my thesis work within their industrial projects. In particular, I would like to thank Renaud Guillaume, Pierre Leroy and Pierre Yves Lowys for their professional guidance in conducting the experimental tests. Thanks to Eric Gaudin for his essential work in designing the experimental facility and a special thanks to Yann Heratchian for his time and patient spent in running with me the experimental facility, and for his enthusiasm in discovering new achievements.

A nice work environment is one of the most important things to succeed a PhD, and I have never missed it at LMH.

I would like to thank Mohamed for his energy and passion in discussing science: thanks for the inspiring conversations we had, they have been precious for my progress in research.

I'm grateful to Isabelle for her efficient administrative support and her kindness in giving life and travel tips.

## Acknowledgements

---

Thanks to Philippe C., Philippe F., Alain and Vincent, the engineers of the design office, for their priceless skills in problem solving and in finding quick and efficient engineering solutions to any idea I could have, or disaster I could have done!

Thanks to Maxime, Louis, Christian, David, Raymond, and Victor, the technicians of our laboratory, for their impressive capability in building up the experimental set-up in a short time and their patient in fixing every problem could come up. Thanks also to the engineers of the group GEM, in particular to Alberto for his availability in helping me in running the experiments.

I could write an entire thesis in describing how much I admire Outi and in thanking her for the exceptional and timeless friendship we built during our years of PhD. Thanks to my office mates, João Brazil and João Portugal, for the mutual help and the fun conversations to recharge our energies. Thanks also to the other PhD students in the lab, Alexis, Ali, Sebastian and Siamak, for the great laughs and the sometimes absurd but really interesting conversations we had, I wish to all of them the best luck for their doctoral thesis. Thanks to Simon for his support, for his patient in teaching me some basics in numerical simulations and for the amazing adventures we had in the hot but wonderful Californian natural parks. To Keita, for the nice time we spent during the conference and after-conference in Slovenia. Thanks to Audrey, Ebrahim, Federico and Pascal for sharing pleasant lunch time and coffee breaks. Thanks also to the visiting PhD students, in particular Xiaoran and Qin, for having brought to our lab a bit of their culture by sharing nice experiences and preparing tasty dinners.

If I reevaluated so quickly the first impression I had of Lausanne, it has been also thanks to the previous PhD students at LMH who warmly welcomed me not only in the laboratory but also in their after-work time in Lausanne. Andres, travel agency and beers sponsor, I really appreciated how you helped me integrating with the group. Arthur, thanks for the many beers and spritz at the Great Escape, and for the almost successful trip to Prague! Big body, thanks for the several meals you prepared for me even if sometimes I forgot to come to eat them! Matthieu (aka radio couloir) and Christian, thanks for the many laughs we shared and that we keep on sharing also now that you have a "real job".

By dealing with hydraulics machines, I had the opportunity to strike up a friendship with several people working in the lab of hydraulics constructions at EPFL: thanks Davide for the trips we enjoyed together and for the future ones coming up! Irene and Elena, I really enjoyed the time spent with you during conferences, PhD schools, lunchtime and fun evenings; Pali, I will be always grateful to you for having introduced me to aerial silk!

Lausanne didn't offer me only a nice place to work on my thesis but it also gave me the chance to meet wonderful people outside the working time and to start new activities. Stefano, thanks for having forgiven my "little" catastrophes at home (since finally I'm still alive!) and for being the best flatmate and friend I could ever wish for. Thanks also for having adopted me in your lab IPESE, sharing with me the nice activities, such as Vivapoly or the ski weekends, and introducing me to your lovable colleagues: Sophia, Victor, Raman, Nils, Steph, ... (you are too many!), a big thanks to all of you for the fun evenings and weekends spent together!

## Acknowledgements

---

A big thanks to Irene, Selma, Anna and Dominique who made my after-work time really pleasant and truly become a reference point for my life in Lausanne.

I would like to thank all the members of the dance troupe of ArtMonica who let me keep alive my passion for dancing.

And then there are some people you meet in your life and you build up timeless friendships which you could never do without. Deborah, my primary source of motivation and inspiration: thanks for the inestimable time spent together, the uncountable laughs and unforgettable experiences we shared. Thanks to all my friends, in particular Sara, Valeria, Giamma, Gigi, Ella, Pamela, Silvia, Giorgio, Francesca, Veronica, Signi, Luchino, Beatrice and Loïse: even if we live far away from each other, we always found a way to keep posted about our lives. You all let me feel closer to home.

Valentin, I don't have enough words to thank you for all the support and happiness you have been giving me during these years. I love you.

Last but not at least, I'm sincerely grateful to my extraordinary family, my parents Luciana and Paolo, and my adorable sister Sara. Thanks for your love, your education and your fundamental presence in my life. Without your constant support I could never have achieved a doctorate.

*Lausanne, August 2018*

Elena





# Abstract

Hydraulic turbines and pump-turbines are often required to operate in particular conditions at which they consume active power. To keep the power consumption at a minimum, it is necessary to dewater the runner to reduce the mechanical torque. One of these operating conditions is the synchronous condenser mode for the reactive power regulation of the grid. This operating mode requires the guide vanes closure and the lowering of the tail water below the runner by injecting pressurized air in the machine. Due to the air-water mixing, torque instabilities and air losses are observed in this operating mode causing the increase of the power consumption.

In this thesis, *the two-phase flow phenomena characterizing the operation in synchronous condenser mode are experimentally investigated; additionally, a theoretical framework is proposed to analytically describe and predict the observed flow phenomena and the corresponding power and air losses.* These research challenges are addressed by means of four different contributions.

First, the development of the sloshing motion of the air-water free-surface below the runner is qualitatively and quantitatively described by using high-speed visualization, pressure fluctuations measurements and automated image processing methods.

Second, the development of an air-water ring in the vaneless gap between the runner and the guide vanes is studied by means of image processing and pressure fluctuations measurements to assess both the velocity and the pressure flow field. The pressure measurements in the vaneless gap make apparent a fluctuation due to the interaction of the rotating and stationary components and of the rotating two-phase flow. This interaction is revealed by the development of the Fourier series applied to the harmonic components of the system and the modal decomposition of the pressure signal.

Third, the influence of the two-phase flow phenomena on the torque swings is investigated. Measurements of the resisting mechanical torque transmitted through the coupling of the runner and the shaft and corresponding to the absorbed mechanical power of the runner in the hydraulic turbine are performed; in addition, a study on the influencing operating parameters allows building an empirical predictive model of the torque.

Finally, a study on the oxygen mass transfer in the water volume is performed by measuring the oxygen concentration in the spiral case and in the draft tube of the hydraulic turbine. A theoretical framework is developed on the equations governing the diffusion of oxygen in water and the diffusion coefficients are computed and validated with experimental results. Moreover, this study allows quantifying the air losses due to the diffusion of air in water and to

## Abstract

---

model the diffusion process as a function of the operating parameters of the machine. The results allow the understanding of the two-phase flow mechanism in a turbine or pump-turbine operating in synchronous condenser mode causing instabilities and air losses. Furthermore, the predictive model of the power losses due to both torque and air consumption represents a novel achievement for the study of the two-phase flow in a turbine operating in condenser mode or, more in general, in dewatered condition, and for the control of the machine behavior and consumption on the full scale prototype.

**Keywords:** Francis-type turbines and pump-turbines, synchronous condenser mode, two-phase flow, sloshing free-surface, fluid-structure interactions, air mass transfer, oxygen concentration.

# Résumé

Les turbines et les pompes-turbines hydrauliques doivent souvent fonctionner en conditions dans lesquelles elles consomment de la puissance active. Pour minimiser la consommation d'énergie, il est nécessaire de dénoyer la roue pour diminuer le couple mécanique. Un mode de fonctionnement qui nécessite une telle configuration correspond à la marche en compensateur synchrone afin de régler la puissance réactive du réseau. Dans ce mode, il est nécessaire de fermer les directrices et d'abaisser le niveau d'eau sous la roue grâce aux injections d'air sous pression dans la turbine hydraulique. En raison du mélange de l'air et de l'eau, les variations de couple et les fuites d'air sont enregistrées dans ce mode de fonctionnement, provoquant l'augmentation de la consommation de la puissance active.

Dans la présente thèse, *les phénomènes diphasiques qui caractérisent l'écoulement dans une turbine hydraulique en mode compensateur synchrone sont étudiés expérimentalement et le développement d'une étude théorique est proposé pour décrire analytiquement les phénomènes diphasiques observés et la consommation d'énergie*. Cette étude est abordée suivant de quatre approches différents.

Premièrement, le développement du mouvement oscillatoire non-linéaire de la surface libre sous la roue est qualitativement et quantitativement étudié en utilisant l'acquisition d'images à haute vitesse, les mesures de pression et le développement d'une méthode d'analyse d'image automatique.

Deuxièmement, la formation d'un anneau liquide constitué d'un mélange air-eau dans l'entrefer entre les directrices et la roue est étudié au moyen de traitements d'images et de mesures de fluctuations de pression pour évaluer les champs de vitesse et de pression du flux diphasique. Les mesures de pression dans l'entrefer permettent de mettre en évidence une fluctuation de l'anneau diphasique due à l'interaction rotor-stator entre les aubes de la roue et les directrices. Cette interaction est mise en évidence grâce une analyse en séries de Fourier, appliquée aux composants harmoniques du système et grâce à la décomposition modale des signaux de mesure de pression.

Troisièmement, l'influence des phénomènes diphasiques sur la variation du couple mécanique est évaluée à l'aide de tests expérimentaux. Les mesures du couple mécanique résistant sont effectués à l'arbre de la turbine hydraulique et une étude des paramètres de fonctionnement qui influencent l'écoulement a permis le développement d'un modèle théorique du couple mécanique.

Enfin, l'étude du transfert de masse d'oxygène dans le volume d'eau est effectuée en mesurant la variation de sa concentration dans l'eau dans la bêche et dans le diffuseur de la turbine

## Abstract

---

hydraulique. Un cadre théorique de la diffusion de l'air dans le volume d'eau est développé et les coefficients de diffusion sont calculés et validés sur des données expérimentales en fonction des paramètres de fonctionnement de la turbine. Grâce à cette étude, un modèle capable de prédire les fuites d'air en fonction des paramètres de fonctionnement de la turbine hydraulique a été validé.

Les résultats obtenus expliquent les mécanismes à l'origine du développement de phénomènes diphasiques dans une turbine en mode compensateur synchrone, des fluctuations du couple et des pertes d'air. De plus, l'étude théorique réalisée pour prédire la consommation de puissance constitue une nouvelle étape dans le dimensionnement des turbines exploitées en mode compensateur synchrone ou plus généralement en régimes roues dénoyées. Ceci permet le contrôle du comportement de la turbine sur le site du prototype.

**Mots clefs :** Turbines et pompes-turbines Francis, compensateur synchrone, écoulement diphasiques, mouvement oscillatoire de la surface libre, interaction fluide-structure, transfert de masse d'air, concentration d'oxygène.

# Abstract

Turbine e pompe-turbine idrauliche spesso operano in condizioni che richiedono il consumo di potenza attiva. Per minimizzare il consumo energetico è necessario che il livello d'acqua nella girante venga ridotto per diminuire la coppia meccanica. Una modalità di funzionamento che richiede tale riduzione è il compensatore sincrono, usato per regolare la potenza reattiva della rete elettrica. In tale modalità è necessaria la chiusura delle pale del distributore e l'abbassamento del livello d'acqua sotto la girante attraverso l'aggiunta di aria pressurizzata nella turbina idraulica. A causa della miscelazione di aria e acqua, variazioni della coppia meccanica e perdite d'aria vengono frequentemente riscontrate durante questa tipologia di funzionamento, generando l'aumento della potenza attiva assorbita.

In questa tesi sono studiati sperimentalmente *i fenomeni bifasici che caratterizzano il flusso nella turbina idraulica nella modalità di compensatore sincrono. Lo sviluppo di uno studio teorico è proposto per descrivere analiticamente i fenomeni osservati e il corrispondente consumo di potenza.* Quattro principali contributi scientifici sono sviluppati per rispondere alla domanda di ricerca.

In primo luogo, lo sviluppo del moto oscillatorio non lineare della superficie a pelo libero d'acqua sotto la girante è studiato qualitativamente e quantitativamente attraverso l'acquisizione d'immagini ad alta velocità, misure di pressione e sviluppando un metodo d'analisi d'immagini automatico.

In secondo luogo, la formazione di un anello d'acqua e aria nel traferro tra le pale della girante e del distributore è studiato attraverso analisi d'immagini e misure di pressione per determinare sia il campo di pressione sia quello di velocità del flusso. Le misure di pressione nel traferro evidenziano una fluttuazione dovuta all'interazione della componente rotante della turbina con quella statica e con l'anello bifasico. Questa interazione è dimostrata grazie allo sviluppo della serie di Fourier applicata alle componenti armoniche del sistema e grazie alla decomposizione modale dei segnali di misura di pressione.

Terzo, l'influenza dei fenomeni bifasici sulla variazione della coppia meccanica è valutata con test sperimentali. Misure della coppia meccanica resistente sono effettuate nella turbina idraulica e uno studio sui parametri operazionali che influenzano il flusso ha permesso lo sviluppo di un modello teorico della coppia meccanica.

Infine lo studio della diffusione d'ossigeno nel volume d'acqua è condotto misurando la variazione della sua concentrazione in acqua nel distributore a chiocciola e nel diffusore della turbina idraulica. Un quadro teorico della diffusione d'aria nel volume d'acqua è sviluppato e i coefficienti di diffusione sono calcolati e validati su dati sperimentali in funzione dei parametri

## Abstract

---

operazionali della turbina. Grazie a questo studio è validato un modello in grado di predire le perdite d'aria in funzione dei parametri operazionali della turbina idraulica.

I risultati ottenuti spiegano i meccanismi che portano allo sviluppo di fenomeni bifasici in una turbina che lavora come compensatore sincrono e la causa delle oscillazioni della coppia e delle perdite d'aria. Inoltre, lo studio teorico effettuato per predire il conseguente consumo di potenza rappresenta un'innovazione nello studio delle turbine idrauliche in modalità di compensatore sincrono o, più in generale, in regimi diversi rispetto alle condizioni di progettazione, e nel controllo del comportamento della turbina negli impianti idroelettrici in scala reale.

**Parole chiave:** Turbine e pompe-turbine Francis, compensatore sincrono, flusso bifasico, moto oscillatorio della superficie a pelo libero, interazione fluido-struttura, diffusione d'aria in acqua, concentrazione d'ossigeno.

# Contents

<b>Acknowledgements</b>	<b>v</b>
<b>Abstract (English/Français/Italiano)</b>	<b>ix</b>
<b>List of figures</b>	<b>xvii</b>
<b>List of tables</b>	<b>xxiii</b>
<b>Nomenclature</b>	<b>xxvii</b>
<b>Introduction</b>	<b>1</b>
Research context . . . . .	1
Operation in synchronous condenser mode of Francis-type turbines and reversible pump-turbines . . . . .	2
State of the art . . . . .	4
Thesis objective . . . . .	8
Thesis structure . . . . .	8
<b>1 Sloshing free-surface</b>	<b>11</b>
1.1 Experimental investigation of the sloshing motion of the water free-surface in the draft tube of a Francis turbine operating in synchronous condenser mode . . . . .	11
1.1.1 Introduction . . . . .	12
1.1.2 Methodology . . . . .	15
1.1.3 Results . . . . .	24
1.1.4 Discussion . . . . .	29
1.1.5 Summary and Conclusion . . . . .	32
1.2 Non-linear liquid sloshing in a cylindrical tank forced by a rotating fan . . . . .	34
1.2.1 Introduction . . . . .	34
1.2.2 Experimental set-up . . . . .	34
1.2.3 Characterization of the non-linear liquid sloshing . . . . .	35
1.2.4 Comparison with the sloshing motion of the air-water free-surface in a Francis turbine operating in condenser mode: cause and onset . . . . .	38
1.2.5 Conclusion . . . . .	39

## Contents

---

<b>2</b>	<b>Air-water ring</b>	<b>41</b>
2.1	Introduction . . . . .	42
2.2	Experimental set-up . . . . .	44
2.2.1	Facility . . . . .	44
2.2.2	Instrumentation . . . . .	44
2.2.3	Investigated operating points . . . . .	46
2.3	Method . . . . .	47
2.3.1	Image processing . . . . .	47
2.3.2	Pressure fluctuations and spectral analysis . . . . .	48
2.4	Results and discussion . . . . .	48
2.4.1	Size of the bubbles . . . . .	48
2.4.2	Influence of the cooling discharge on the velocity profiles . . . . .	51
2.4.3	Influence of the gauge pressures on the velocity profiles . . . . .	52
2.4.4	Angular distribution of the radial and tangential velocity components of bubbles in the air-water ring . . . . .	54
2.4.5	Pressure field in the vaneless gap . . . . .	54
2.4.6	Evidence of the rotor-stator interaction . . . . .	56
2.5	Conclusion . . . . .	59
<b>3</b>	<b>Torque stability</b>	<b>61</b>
3.1	Introduction . . . . .	62
3.2	Experimental set-up . . . . .	63
3.2.1	Facility . . . . .	63
3.2.2	Instrumentation . . . . .	65
3.2.3	Investigated operating points . . . . .	66
3.3	Study of the machine stability . . . . .	66
3.3.1	Spectral analysis . . . . .	66
3.3.2	Phase averaging procedure . . . . .	67
3.4	Results . . . . .	70
3.4.1	Flow visualization and correlation with the resisting mechanical torque and differential pressure cone - gap . . . . .	70
3.4.2	Characterization of the instability caused by the air-water ring . . . . .	71
3.4.3	Instability cause and onset . . . . .	75
3.5	Empirical modeling of the differential pressure at stable operating condition . . . . .	76
3.5.1	Variables definition . . . . .	76
3.5.2	Dimension reduction . . . . .	77
3.5.3	Prediction of the differential pressure . . . . .	78
3.6	Conclusion . . . . .	80
<b>4</b>	<b>Air diffusion in the liquid volume</b>	<b>83</b>
4.1	Introduction . . . . .	84
4.2	Experimental set-up . . . . .	85
4.2.1	Facility . . . . .	85



4.2.2 Instrumentation . . . . .	86
4.2.3 Investigated operating points . . . . .	87
4.3 Analytical solution . . . . .	88
4.4 Data processing method . . . . .	93
4.4.1 Estimation of the global diffusion coefficients in the vaneless gap and in the cone. . . . .	93
4.4.2 Estimation of the oxygen diffused in water in the cone of the draft tube by measuring the water level elevation . . . . .	93
4.5 Results . . . . .	94
4.5.1 Evolution of the oxygen concentration in the water volume . . . . .	94
4.5.2 Analytical solution: estimation of the global diffusion coefficients in the vaneless gap and in the cone of the draft tube . . . . .	96
4.5.3 Validation of the theoretical framework with the measurements of the oxygen concentration. . . . .	98
4.6 Discussion . . . . .	99
4.6.1 Influence of the densimetric Froude number on the oxygen concentration	99
4.6.2 Estimation of the air losses due to the diffusion through the free-surface in the draft tube cone . . . . .	99
4.7 Conclusion . . . . .	100
<b>5 Guideline for power consumption calculation</b>	<b>103</b>
5.1 Introduction . . . . .	103
5.2 Methodology . . . . .	103
5.2.1 Mechanical torque . . . . .	103
5.2.2 Air losses . . . . .	105
5.3 Example . . . . .	106
<b>Conclusion and perspectives</b>	<b>109</b>
Conclusion . . . . .	109
Perspectives . . . . .	112
<b>Bibliography</b>	<b>121</b>
<b>Curriculum Vitae</b>	<b>123</b>



# List of Figures

1	Mix of electricity sources in 2016 [5]. . . . .	2
2	Francis-type turbine or pump-turbine components. . . . .	3
3	Francis-type pump-turbine operating in synchronous condenser mode. . . . .	4
4	Behavior of the water surface. Reproduced from [100]. . . . .	5
1.1	Reduced scale physical model of the Francis turbine installed inn the test rig including the main instrumentation. . . . .	14
1.2	Horizontal cut view of the draft tube at the pressure sensor lower section together with the scheme of the acquisition chain. . . . .	16
1.3	Investigated operating conditions of the Francis turbine operating in condenser mode . . . . .	16
1.4	Extracted matrices of pixels, filtering for sloshing detection and perturbation of the image to apply the Monte Carlo method. . . . .	19
1.5	(a) Sequence of images of the water free-surface oscillating during the condenser mode operation of the Francis runner at $p = 2$ bar and $Fr_d = 0.75$ with high water level condition. (b) Time resolved signal of the difference in elevation of the two sides of the sloshing water free-surface measured with the image processing method. (c) Corresponding spectrum magnitude of the signal in (b). . . . .	20
1.6	Time history of the pressure coefficients C1 and C2 (a) and torque factor (b). Spectra in logarithmic scale of C1 and C2 (c) and of the torque signal (d). Coherence between the two pressure fluctuations measurements C1 and C2 (e) and coherence between the torque signal and C1 (f). All results are shown for $Fr_d = 1$ at $p = 1.5$ bar with high water level condition. . . . .	21
1.7	Typical images of the sloshing motion of the free-surface in the draft tube cone of a Francis turbine operating in condenser mode at $p = 2$ bar for the six investigated densimetric Froude number values. . . . .	22
1.8	Simultaneous time history of the difference in elevation of the two sides of the sloshing water free-surface extracted by the image processing and pressure coefficients derived from pressure measurements at the lower section of the draft tube cone at $p = 2$ bar, $Fr_d = 0.5$ . . . . .	23
1.9	(a) Time history of the frequency of the pressure fluctuations derived from pressure measurements at the lower section of the draft tube cone at $p = 2$ bar, $Fr_d = 0.5$ .(b) Spectrum magnitude in logarithmic scale of the pressure signal at different time interval. . . . .	24

## List of Figures

---

1.10 (a) Froude number of the sloshing free-surface.(b) Measured amplitude of the sloshing motion divided by the high pressure diameter of the Francis runner. . . . .	26
1.11 Influence of the densimetric Froude number on the RMS of the pressure coefficient at C2 at high water level condition. . . . .	27
1.12 Influence of the densimetric Froude number on the Froude number of the sloshing free-surface (a) and on the RMS of the pressure coefficient (b) for the three investigated water levels at $p = 1.5$ bar. . . . .	28
1.13 Influence of the densimetric Froude number on the frequency of the sloshing motion and torque oscillation at $p = 1.5$ bar and high water level condition. . . . .	29
1.14 (a) Coherence at the sloshing frequency. (b) Coherence at the dominant frequency of the torque oscillation. All results are shown for all the investigated $Fr_d$ values at $p = 1.5$ bar and high water level condition. . . . .	30
1.15 Natural frequency of the water volume and frequency of the sloshing motion as a function of the water level $l$ divided by the inner diameter of the cone $D$ at $p = 1.5$ bar for the investigated $Fr_d$ values. . . . .	32
1.16 Scheme of the test facility with the instrumentation. . . . .	35
1.17 Images of one rotation of the sloshing motion of the free-surface at $N = 1300 \text{ min}^{-1}$ , $l = 0.1$ m and $h = 0.25$ m. . . . .	36
1.18 a) Time history of the elevation of the free-surface during the sloshing motion. b) Power spectrum in frequency domain of the sloshing amplitude at $N = 1100 \text{ min}^{-1}$ , $l = 0.1$ m and $h = 0.15$ m . . . . .	37
1.19 Images of the maximum amplitude of the sloshing motion at the different rotational speed of the fan at $l = 0.1$ m and $h = 0.15$ m . . . . .	37
1.20 Amplitude (a) and frequency (b) of the sloshing motion as a function of the rotational speed of the fan for all the investigated operating conditions. . . . .	38
2.1 Test-rig layout with the instrumentation. . . . .	45
2.2 Top view of the 9 bladed impeller and the 20 guide vanes of the pump-turbine model. . . . .	45
2.3 Investigated operating points on the iso-Froude curve at $Fr_d = 0.5$ as a function of the rotational speed $N$ and the gauge pressure $p$ . . . . .	46
2.4 Flow chart of the image processing method for tracking bubbles at $p = 2$ bar. $x$ represents the perimeter of the black area of interest in the image to feature bubbles. . . . .	49
2.5 Sample image. . . . .	49
2.6 Steps of the image processing method to measure the velocity of the bubbles in the air-water ring. . . . .	50
2.7 Time history (a) and auto-spectrum (b) of the pressure measurements at the location C1 at $p = 5$ bar and $Q = 60 \text{ l}\cdot\text{h}^{-1}$ . . . . .	50
2.8 Cross-spectral analysis between the pressure measurements at the locations C1 and C3 at $p = 5$ bar and $Q = 60 \text{ l}\cdot\text{h}^{-1}$ . Cross-spectrum amplitude in logarithmic scale (top) and coherence (bottom). . . . .	51

2.9	Images of the air-water ring in the vaneless gap at $p = 5$ bar for the four cooling discharge conditions. . . . .	52
2.10	Images of the air-water ring in the vaneless gap at $Q = 60 \text{ l}\cdot\text{h}^{-1}$ for the five investigated gauge pressure conditions. . . . .	52
2.11	Equivalent diameter distribution statistics as a function of the gauge pressure at $Q = 60 \text{ l}\cdot\text{h}^{-1}$ . . . . .	53
2.12	Velocity profile of tangential (a) and radial (b) velocity at $p = 5$ bar. . . . .	53
2.13	Velocity profile of tangential (a) and radial (b) velocity at $Q = 60 \text{ l}\cdot\text{h}^{-1}$ . . . . .	54
2.14	Angular distribution of the tangential velocity component of the bubbles in the air-water ring at $Q = 60 \text{ l}\cdot\text{h}^{-1}$ and $p = 5$ bar. . . . .	55
2.15	Angular distribution of the radial velocity component of the bubbles in the air-water ring at $Q = 60 \text{ l}\cdot\text{h}^{-1}$ and $p = 5$ bar. . . . .	55
2.16	Frequency corresponding to the spectrum peak of the pressure fluctuation normalized to the frequency of the blades passage $f_b$ as a function of the cooling discharge at $p = 9$ bar (a) and as a function of the gauge pressure at $Q = 60 \text{ l}\cdot\text{h}^{-1}$ (b). Auto-spectrum of the pressure measurements as a function of the cooling discharge at $p = 9$ bar (c) and as a function of the gauge pressure at $Q = 60 \text{ l}\cdot\text{h}^{-1}$ (d). . . . .	56
2.17	Spectral analysis of the instantaneous pressure in the vaneless gap at a radius $r/R_e = 1.06$ and $p = 5$ bar. . . . .	58
3.1	Illustration of the air-water ring in vaneless gap between the closed guide vanes and the impeller blades of a reversible pump-turbine. . . . .	64
3.2	Scheme of the test facility with the instrumentation. . . . .	65
3.3	Investigated operating points and iso-Froude curves as a function of the rotational speed $N$ and the gauge pressure $p$ . . . . .	66
3.4	Auto-spectrum in logarithmic scale of the pressure coefficient (a), of the torque coefficient (b) and coherence between the torque and the differential pressure signals (c) at $Fr_d = 1.2$ , $p = 5$ bar and $Q = 60 \text{ l}\cdot\text{h}^{-1}$ . . . . .	68
3.5	Identification of the instability cycles in the differential pressure signal and the resisting torque signals synchronously measured at $Fr_d = 1.2$ , $p = 5$ bar and $Q = 60 \text{ l}\cdot\text{h}^{-1}$ . (a) Differential pressure coefficient. (b) Torque coefficient. . . . .	69
3.6	Phase-averaged signal of the resisting torque and its corresponding standard deviation together with the raw data corresponding to the successive cycles of the periodic instability. . . . .	70
3.7	Images of the air-water ring for each flow Regime. . . . .	72
3.8	Differential pressure coefficient as a function of the densimetric Froude number. . . . .	72
3.9	Torque coefficient as a function of the differential pressure coefficient. . . . .	72
3.10	Differential pressure coefficient as a function of the gauge pressure at $Fr_d = 0.5$ . . . . .	73
3.11	Time history of the air-water ring in the vaneless gap between the closed guide vanes and the impeller blades in one period of the instability in Regime 2 causing torque instability. . . . .	74

## List of Figures

---

3.12	Mean phase averaging of the torque and differential pressure signal together with the $GL$ values extracted from the high-speed visualization of the air-water ring in one period of the instability at $Fr_d = 1.2$ . . . . .	74
3.13	(a) Mean frequency of the periodic instability. (b) RMS of both torque coefficient and differential pressure coefficient as a function of the densimetric Froude number. . . . .	75
3.14	Time history of the water level and $C_{\Delta p}$ (a) and of the tap wall pressure sensors in the cone of the draft tube and in the vaneless gap at $Fr_d = 1.2$ and $Q = 70 \text{ l}\cdot\text{h}^{-1}$ . . . . .	77
3.15	Evaluation of the performance of the surrogate model by changing the maximum interpolation degree. . . . .	79
3.16	Data set and model of the differential pressure coefficient as a function of the densimetric Froude number validated for $Fr_d > 2$ . . . . .	80
3.17	Measured differential pressure coefficient as a function of the model given in eq. (3.10). . . . .	81
3.18	Residual difference between the measured differential coefficient and the model as a function of the densimetric Froude number (a), the gauge pressure (b), the cooling discharge (c) and the rotational speed of the impeller (d). . . . .	81
4.1	Scheme of the test facility with the instrumentation. . . . .	87
4.2	Investigated operating points on the iso-Froude curve as a function of the rotational speed $N$ and the gauge pressure $p$ . . . . .	88
4.3	Scheme of the water volumes and flows considered to perform the theoretical framework of the diffusion of air in water in the reduced scale physical model of a reversible pump-turbine. . . . .	89
4.4	Time history of the water level at $Fr_d = 4$ , $p = 10 \text{ bar}$ and $Q = 80 \text{ l}\cdot\text{h}^{-1}$ . . . . .	94
4.5	Averaged value of the measured oxygen concentration in the spiral case (a) and in the draft tube (b) as a function of the gauge pressure. . . . .	96
4.6	Time solved oxygen concentration divided by the concentration at the saturation condition in the three measurements locations at $Fr_d = 4$ , $p = 10 \text{ bar}$ and $Q = 40 \text{ l}\cdot\text{h}^{-1}$ . . . . .	96
4.7	Averaged value of the measured oxygen concentration, divided by the concentration at the saturation condition, in the spiral case (a) and in the draft tube (b) as a function of the gauge pressure. . . . .	97
4.8	Influence of the densimetric Froude number on the computed diffusion coefficients and interpolating functions. . . . .	98
4.9	Time history of the oxygen concentration as a result of the theoretical framework developed for $Fr_d = 2$ (a) and $Fr_d = 4$ (b), $p = 16 \text{ bar}$ and $Q = 80 \text{ l}\cdot\text{h}^{-1}$ . . . . .	98
4.10	Measured oxygen concentration as a function of the value of the oxygen concentration computed by solving eq. (4.17) at stable condition in the spiral case (a) and in the draft tube (b). . . . .	99
4.11	Computed mass flow rate of oxygen by solving eq. (4.22) as a function of the measured value of the oxygen mass flow rate as in eq. (4.23). . . . .	101

4.12	Air losses computed according to eq. (4.26) and iso-pressure line as a function of the densimetric Froude number for $Q = 40 \text{ l}\cdot\text{h}^{-1}$ (a) and $Q = 80 \text{ l}\cdot\text{h}^{-1}$ (b). . . .	102
5.1	Torque coefficient as a function of the gauge pressure in the draft tube cone and interpolating function for $Fr_d = 0.5$ . . . . .	104
5.2	Power consumption due to air losses on iso-pressure lines as a function of the densimetric Froude number. . . . .	107







## List of Tables

1.1	Range of the parameters during the experimental investigation. . . . .	35
2.1	Pressure sensors position in the vaneless gap. . . . .	46
3.1	Pressure sensors position to measure the gap-cone differential pressure. . . . .	65
3.2	Range of the input parameters to build the model. . . . .	76
3.3	Relative importance of the variables of the surrogate model of the differential pressure coefficient, measured thanks to the GCV error and the MSE. . . . .	80
3.4	Performance of the surrogate model. . . . .	80
4.1	Oxygen probes position. . . . .	88



# Nomenclature

## Acronyms

CFD	Computational Fluid Dynamics
EPFL	École Polytechnique Fédérale de Lausanne
GCV	Generalized Cross Validation error
GL	Gray Level
LDV	Laser Doppler Velocimetry
LMH	Laboratoire de Machine Hydraulique
MRV	Magnetic Resonance Velocimetry
MSE	Mean Squared Error
NRE	New Renewable Energy sources
PIV	Particle Image Velocimetry
PTV	Particle Tracking Velocimetry
RMS	Root Mean Square
RSI	Rotor Stator Interaction
rpm	revolutions per minute

## Superscripts

gas	gas phase
i	interface
liq	liquid phase
p	partial

## Subscripts

0	initial condition
air	air
cone	draft tube cone
computed	computed from theoretical framework
gap	vaneless gap
in	inlet

## Nomenclature

---

lab	labyrinth
lim	limit
measured	measured from experimental data
$N_2$	nitrogen
$O_2$	oxygen
out	outlet
rec	recycling pipe
sat	saturation

## Latin letters

$x, y$	Cartesian coordinates	(m)
$r, \theta, z$	Cylindrical coordinates	(m)
$A$	area	(m <sup>2</sup> )
$A_l$	amplitude of the $l^{th}$ harmonic in the water ring	(Pa)
$A_m$	amplitude of $m^{th}$ harmonic in the rotating system	(Pa)
$A_n$	amplitude of the $n^{th}$ harmonic in the stationary system	(Pa)
$a$	oblate spheroid minor axis	(m)
$b$	oblate spheroid major axis	(m)
$C_r$	radial velocity component	(m·s <sup>-1</sup> )
$C_u$	circumferential (azimuthal) velocity component	(m·s <sup>-1</sup> )
$C_{xy}$	Coherence	(-)
$c$	reduction coefficient	(-)
$d$	surface distance	(m)
$d_{eq}$	equivalent diameter; $d_{eq} = (8b^2a)^{1/3}$	(m)
$D$	inner cone diameter	(m)
$D_e$	external impeller diameter	(m)
$E$	specific energy	(J·kg <sup>-1</sup> )
$f$	frequency	(Hz)
$f_{inst}$	instability frequency	(Hz)
$f_0$	RSI frequency	(Hz)
$f_{sloshing}$	sloshing frequency	(Hz)
$f_{wave}$	wave frequency	(Hz)
$G_{xx}$	auto-spectrum	(s)
$G_{xy}$	cross-spectrum	(s)
$g$	gravity	(m·s <sup>-2</sup> )
He	Henry constant	(l·atm·mol <sup>-1</sup> )
$h$	sloshing amplitude	(m)
$h_{gap}$	height vaneless gap	(m)
$h_{peak}$	peak sloshing amplitude	(m)
$K$	global mass transfer coefficient	(m·s <sup>-1</sup> )
$K_G$	mass transfer coefficient gas phase	(m·s <sup>-1</sup> )

## Nomenclature

$K_L$	mass transfer coefficient liquid phase	$(\text{m}\cdot\text{s}^{-1})$
$k_{1,2,3,4}$	contribution to the diametrical pressure modes	(-)
$l$	water level	(m)
$MM$	molar mass	$(\text{mol}\cdot\text{g}^{-1})$
$m$	mass	(kg)
$\dot{m}$	mass flow rate	$(\text{kg}^{-1})$
$N$	rotational speed	$(\text{min}^{-1})$
$N_{\text{sp}}$	explored points	(-)
$n$	rotating frequency	(Hz)
$n_{\text{peak}}$	number of oscillations	(-)
$n_{\text{px}}$	number of pixels	(-)
$p$	gauge pressure	(Pa)
$p_r$	pressure field rotating system	(Pa)
$p_s$	pressure field stationary system	(Pa)
$p_{wr}$	pressure field water ring	(Pa)
$q$	molar flux	$(\text{mol}\cdot\text{s}^{-1}\cdot\text{m}^{-2})$
$Q$	cooling discharge	$(\text{m}^3\cdot\text{s}^{-1})$
$R$	gas constant	$(\text{J}\cdot(\text{mol}\cdot\text{K})^{-1})$
$R^2$	coefficient of determination	(-)
$R_e$	external impeller radius	(m)
$T$	period of the sloshing motion	$(\text{s}^{-1})$
$T_{\text{inst}}$	period of the instability	$(\text{s}^{-1})$
$T_m$	mechanical torque	$(\text{N}\cdot\text{m})$
$t$	time	(s)
$t_{\text{acq}}$	acquisition time	(s)
$U_{\text{tip}}$	peripheral blade tip velocity	$(\text{m}\cdot\text{s}^{-1})$
$V$	volume	$(\text{m}^3)$
$w$	width	(m)
$X$	gas fraction	$(\text{mol}\cdot\text{mol}_{\text{air}}^{-1})$
$x$	concentration	$(\text{mol}\cdot\text{l}^{-1})$
$z_M$	number of parameters	(-)
$z_b$	number of blades	(-)
$z_o$	number of guide vanes	(-)

### Greek letters

$\Theta$	temperature	(K)
$\theta_r^*$	angular position of the water ring	(rad)
$\theta_r$	angular position of the rotating system	(rad)
$\theta_s$	angular position of the stationary system	(rad)
$\nu$	kinematic viscosity	$(\text{m}^2\cdot\text{s})$
$\rho$	density	$(\text{kg}\cdot\text{m}^{-3})$

## Nomenclature

---

$\sigma_f$	standard deviation of the frequency	(Hz)
$\tau_0$	diffusion time	(s)
$\tau_1$	discharge diffusion time	(s)
$\tau$	temporal off-set	(s)
$\xi$	wave frequency constant	(-)
$\varphi_l$	phase for the $l^{th}$ harmonic in the water ring	(rad)
$\varphi_m$	phase for the $m^{th}$ harmonic in the rotating system	(rad)
$\varphi_n$	phase for the $n^{th}$ harmonic in the stationary system	(rad)
$\omega$	angular velocity	(rad·s <sup>-1</sup> )

## Dimensionless number

$C_p$	pressure coefficient; $C_p = (p - \bar{p}) / (g \cdot \rho_{\text{water}} \cdot l)$	(-)
$C_{\Delta p}$	differential pressure coefficient; $C_{\Delta p} = \Delta p / (\rho_{\text{water}} \cdot g \cdot D_e)$	(-)
$C_{\Delta p}^*$	model of the differential pressure coefficient	(-)
$C_T$	torque coefficient; $C_T = T_m / (\rho_{\text{water}} \cdot g \cdot D_e^4)$	(-)
$d_{\text{eq}}^*$	non-dimensional bubble diameter; $d_{\text{eq}}^* = d_{\text{eq}} / w$	(-)
$Fr_d$	densimetric Froude number; $Fr_d = \sqrt{\rho_{\text{air}} / \rho_{\text{water}}} \cdot \omega \cdot \sqrt{D_e / g}$	(-)
$Fr_{\text{sloshing}}$	sloshing Froude number; $Fr_{\text{sloshing}} = \pi \cdot f_{\text{sloshing}} \cdot D / \sqrt{g \cdot \pi \cdot D}$	(-)
$Fr_{T_m}$	Froude number of the torque oscillation; $Fr_{T_m} = \pi \cdot f_{T_m} \cdot D / \sqrt{g \cdot \pi \cdot D}$	(-)
$n_{QE}$	IEC specific speed; $n_{QE} = n \cdot Q^{1/2} / E^{3/4}$	(-)
$Re$	Reynolds number; $Re = \omega \cdot (D/2)^2 / \nu$	(-)
$T_{ED}$	IEC torque factor; $T_{ED} = (T_m - \bar{T}_m) / (0.5 \cdot D_e^3 \cdot \rho_{\text{air}} \cdot U_{\text{tip}}^2)$	(-)
$\nu$	specific speed; $\nu = \omega \cdot Q^{1/2} / (\pi^{1/2} \cdot (2 \cdot E)^{3/4})$	(-)

# Introduction

## Research context

Hydro-power is the most exploited renewable energy at a global scale. Nowadays, it accounts for 16.6 % of the world's electricity supply. Its production is expected to increase approximately 3.1 % each year in the next 25 years maintaining its share in the mix of electricity sources [6]. The world electricity supply is presented in Fig. 1.

In Europe, strong efforts are required to reach the goal planned for the 2020 to reduced the green house gas emission by 20 % of 1990 levels [4]. In particular, the development and promotion of new renewable energies (NRE) sources, such as solar and wind, are strengthened. On the other side, the production of energy from NRE sources is not permanently available due to the stochastic nature of these sources. They are seldom able to follow the energy demand.

Pumped storage and traditional hydro-power plants can compensate these fluctuations of the energy production by providing the required energy storage capacity. Moreover, hydraulic turbines feature a flexible power generation and a wide operating range even if in extended operating condition the machine experiences unsteady flow conditions and cavitation. Many successful studies contributed to improve the off-design conditions of a hydraulic turbine by investigating the instability of the flow and the development of cavitation [39, 77, 85, 119].

Another attribute of a hydraulic power plant is the capability of the generator of the hydraulic unit to operate as a synchronous condenser to supply or absorb reactive power and so to stabilize the voltage of the electric grid [50]. Reactive power establishes and sustains the electric and magnetic fields of alternating-current equipment and it must be supplied to most types of magnetic equipment, such as motors and transformers.

Reactive power shortage was the main cause for the blackout in the Northeast of Canada and United States on Aug. 14, 2003 [2, 73], according to a report from Cornell University's Engineering and Economics of Electricity Research Group [88, 104]. Also, Power Systems Engineering Research Center noted that reactive power shortages have been responsible for the 1996 US western electric grid blackouts [115]. It is indeed the necessary regulation of reactive power which ensures the grid reliability, efficiency, and security. As the grid evolves and load profiles change, stresses are being put onto transmission and distribution networks,

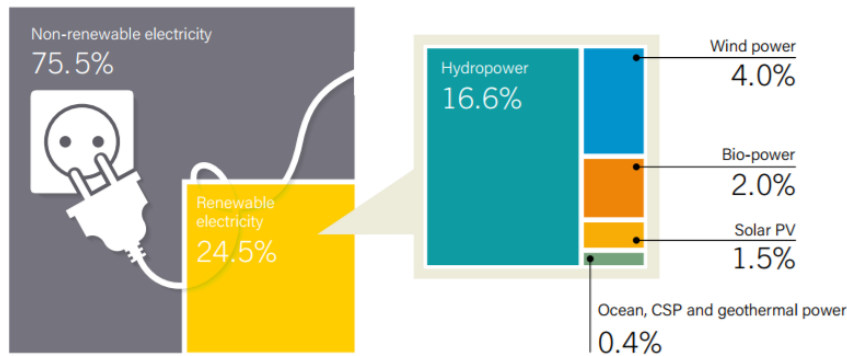


Figure 1 – Mix of electricity sources in 2016 [5].

making the need for voltage support and grid management much more challenging [1]. In particular, the changes in the generation mix, the decreases in conventional generation sources, the increases in NRE sources distribution and the environmental and regulatory policy changes, which are driving the retirement of traditional coal generating stations, entail an operational impact on the electrical infrastructure. This creates an overall deficiency in reactive compensation and voltage support, system inertia and low short circuit strength.

In this context, hydropower units have been drawing increasing attention for their capability to consume and supply reactive power as synchronous condenser for several hours a day and the demand of operating in this mode has increased in the last decades.

## Operation in synchronous condenser mode of Francis-type turbines and reversible pump-turbines

### Francis-type turbine and reversible pump-turbine

Francis-type turbines and reversible pump-turbines are reaction hydraulic machines, which are generally coupled to an electrical machine connected to the grid. They have the ability to convert hydraulic power into mechanical power, if it is used in turbine mode to generate electrical power. In case of a pump storage power plant, which features the storage of surplus electrical power, the reversible pump-turbine can also convert mechanical power into hydraulic power by operating in pump mode. Francis-type turbines and reversible pump-turbine are typically used from 50 m to 600 m of head value. The different components of a Francis-type turbine or pump-turbine are presented in Fig. 2. When operating in turbine mode, an angular momentum is created by the spiral case, stay vanes and guide vanes and recovered by the runner (Francis turbine) or impeller (reversible pump-turbine). Stay vanes are used also for structural stiffening as well as flow distribution. The opening angle of the guide vanes controls the value of the flow rate through the runner/impeller. The angular momentum of the flow is recovered by the blades and converted into mechanical momentum



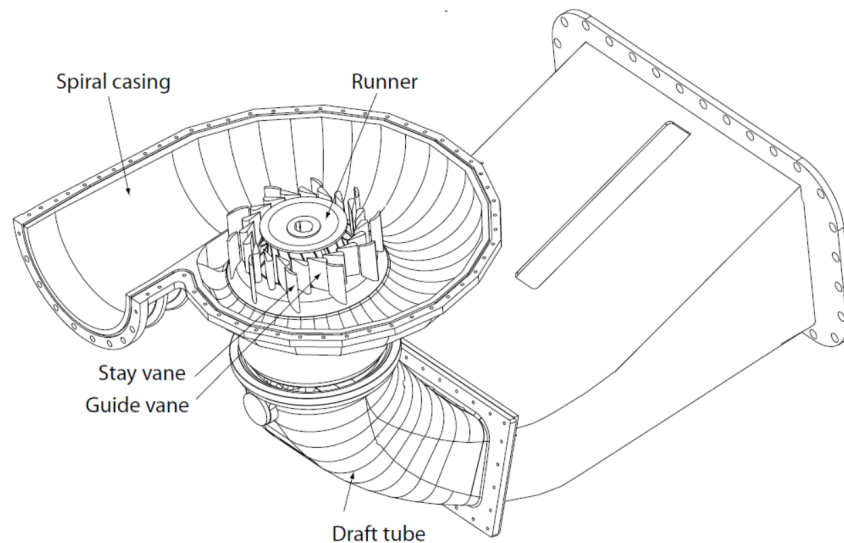


Figure 2 – Francis-type turbine or pump-turbine components.

on the shaft. The flow is then released into the draft tube, which recovers the residual kinetic energy of the flow by converting it into static pressure. For a reversible pump-turbine in pump mode, the impeller rotates in the opposite direction and the water flow reaches the impeller after passing through the draft tube. The stay and guide vanes as well as the spiral case play the role of the pump diffuser. In this mode, the impeller converts mechanical power into hydraulic power.

### **Synchronous condenser mode**

The synchronous condenser mode of a hydro-power unit allows adjusting the conditions on the electric power transmission grid. The generator is controlled by a voltage regulator to either generate or absorb reactive power as needed to adjust the voltage of the grid. Since the hydro-power unit works as a motor system, it consumes active power. The hydraulic machine is connected by a shaft to the generator. Its rotation contributes to the power consumption, mainly due to friction losses. To decrease these losses, Francis-type turbines and reversible pump turbines are rotating in dewatered condition. As illustrated in Fig. 3, the guide vanes are closed and pressurized air is injected in the cone of the draft tube to maintain the water level below the runner/impeller. Water is injected through the labyrinth seals for cooling purpose. A recycling pipe connects the spiral case to the draft tube cone to drain the incoming cooling water flowing from the runner/impeller to the spiral case through the backlash of the guide vanes closure.

The estimation of the compressed air required by this system is challenging: the operation in dewatered condition by injecting air has shown a significant amount of air losses. It is essential to maintain the tail water level below the runner/impeller to avoid friction losses. Indeed,

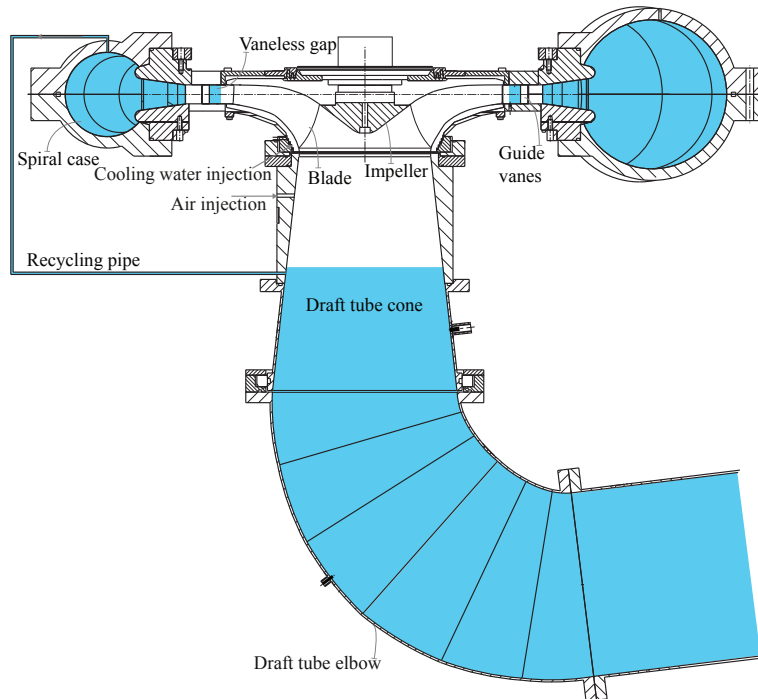


Figure 3 – Francis-type pump-turbine operating in synchronous condenser mode.

air losses must be compensated by additional air injections which cause the increase of the consumption of power. Air losses compensations require to supply an air volume higher than the designed value for the installed air compressor which indeed cannot further provide the required amount of pressurized air causing the dramatic increase of the water level in the draft tube until it interacts with the runner/impeller.

Furthermore, nevertheless the rotation of the runner/impeller in air, considerable torque values and torque swings are experienced whose origin is unclear. They cause significant power consumption which further impact on the total power consumption to operate in condenser mode. In addition, significant power oscillations represent a danger for the mechanical components of the hydraulic unit and for the stability of the electric grid. It has been also observed that these oscillations can make troublesome the switch to condenser mode operation from pumping or generating mode because of load rejection.

## State of the art

### Two-phase flows phenomena and stability of the operation in condenser mode

Francis turbines and pump-turbines operating in synchronous condenser mode experience several difficulties in performing a stable and efficient operation. Following the groundbreaking work begun by Tanaka [100] in applying the densimetric Froude similitude to reach the

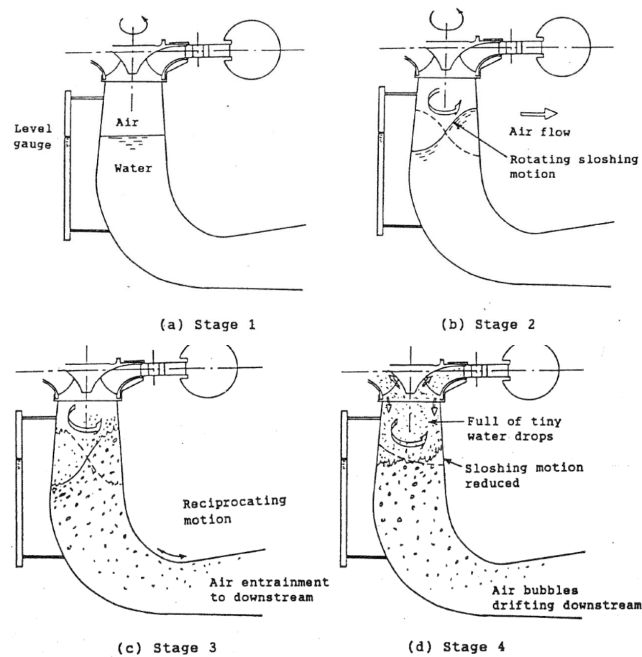


Figure 4 – Behavior of the water surface. Reproduced from [100].

similarity with the prototype, there has been lack of more extensive research related to the two-phase flow phenomena developing during the condenser mode operation. Thus, the reason to explain torque swings and air losses which are increasing the power consumption of the machine is unclear. During dewatered operation, many flow phenomena can be observed due to the mixing of the air and water flows, such as a sloshing motion of the free-surface, turbulent waves causing the formation and entrainment of bubbles diffusing in the water volume, and the formation of droplets interfering with the runner [49, 100].

**Sloshing motion-** The air-water free-surface below the runner/impeller develops a non-linear sloshing motion which can have a key role to understand the problems observed during the condenser mode operation. There are few works in literature which studied this phenomenon [24, 49, 100]. The sloshing motion is qualitatively described as a rotating wave induced by a wind whirl of air agitated by the rotating runner/impeller. The four main stages of the sloshing motion identified by Tanaka [100] are illustrated in Fig. 4. The sloshing motion causes a considerable increase of the air-water mixing when increasing the rotational speed of the runner/impeller. Moreover, it is observed that the amplitude of the wave crest decreases at the Stage 4 and, in this study, a variation of the sloshing frequency is highlighted as well. Several studies have been done to understand the dynamics of a free-surface subjected to harmonic forcing [89, 92], excited at the natural frequency [37, 91, 117], and to estimate the air entrainment caused by this motion [25, 32, 33, 69, 97].

**Air-water ring** - Another expected phenomenon is the development of a rotating air-water ring in the vaneless gap between the closed guide vanes and the blades due to the interaction

## Introduction

---

of the cooling water discharge coming from the labyrinth seals and water droplets which come from the oscillation of the air-water interface entrained by the runner/impeller. Tanaka observed that when the rotational speed is relatively low, the water free-surface in the draft tube cone sways around periodically and regularly with smooth wave crests. On the other hand, by increasing the rotational speed, the inclination of the water free-surface becomes steeper and for further increases of the rotational speed the wave crests begin to be blown away and tiny droplets are entrained by the runner/impeller [100]. The droplets sucked into the runner/impeller and the water cooling discharge are expelled from the outer periphery of the blades by the centrifugal force and form the air-water ring in the vaneless gap. The water ring interacts with the blades and it can cause torque oscillations and increase of power consumption.

**Air diffusion-** Both the sloshing motion and the rotating air-water ring are phenomena which promote air diffusion and air entrainment in water due to the increasing mixing of air and water. Mass transfer is one of the key concept for understanding the air diffusion in water which could be one of the causes of the air losses [31, 41, 71, 107].

Due to two-phase flow complexities which arise in experiments and numerical simulations, combined with the difficulties in making detailed observations within a turbomachine, the mechanism for air losses and torque swings in turbines and pump-turbines operating in condenser mode has been hard to pin down and is still not understood. Thus, to explain such losses and to properly predict both air and power budget in condenser mode operation, new experiments must be devised for the identification and characterization of the two-phase flow phenomena affecting the operation of the machine. And to meet this goal, the development of advanced experimental set-up must be fulfilled for performing optical measurement techniques which are well suited for the investigation of such phenomena with several phases and mechanical interactions.

### **Experimental optical measurement techniques applied to two-phase flow**

Multiple experimental techniques have been developed and performed to investigate the determinant parameters of two-phase flows. Time scale models were created by using point intrusive methods to compute two-phase flow [46, 90]. Since the intrusive techniques do not provide the spatial information, non-intrusive measurement methods have been developed. Thanks to the development of high-speed cameras and optical tools, visualization techniques represented powerful methods to achieve whole-field information in two-phase flows. Example of such non-intrusive experimental techniques are Particle Image Velocimetry (PIV), Laser Doppler Velocimetry (LDV), Particle Tracking Velocimetry (PTV), ultrafast X-ray tomography, Magnetic Resonance Velocimetry (MRV) and shadowgraphy.

PIV has been extensively reported in literature as an ideal tool for measuring the velocity distribution of dispersed particles in multiphase flow systems: bubbles transported in water [53], cavitation phenomena [101], fluid mechanics of multiphase mixing [106], entrainment of

bubbles by a vortex [99], and fluid-structure interaction in a turbo-machine [34, 78]. The major problems that can occur using PIV with two-phase flows are the strong attenuation and the distortion of the laser light due to the optical refraction of the laser beam going through one phase to the other. The second problem is related to the difference in the velocity distribution between the two phases. It is important to develop methods for separating the signals arising from the individual phases, otherwise the resulting velocity value of one phase will be affected by velocity value of the other phase.

X-ray measurement is another non-intrusive technique by means of measuring the attenuation of the X-rays in their passage through the object of measurement, as through liquid/vapor mixtures such as cavitating flows. The main advantage of this technique is that the void fraction of such a mixture can be estimated on a wide range, which is not always the case for optical measurement due to the light diffraction on bubbles in the flow. On the other side, the measurement error is related to the number of detected photons and so the sampling time cannot be as short as with laser based measurement method to increase accuracy [7, 56].

Previous experimental researches suggest combining similar visualization techniques for partially avoiding errors coming from the traditional application of 2D PIV to two-phase flows. For example PIV and shadowgraphy to simultaneously measure the velocity of the two phases are studied in [74], PIV and PTV in [21], PTV and high-speed shadowgraphy in [53]. The developed experimental methodology allowed measuring the velocity fields of the two phases and describing the simultaneous bubbles dynamics with good accuracy and repeatability.

Recent researches dealt with the measurement and uncertainty estimation of two-phase flows with a void fraction higher than 15 % [123]. 2D PIV and LDV with fluorescent particles is a novel successful technique to investigate two-phase flows in pump-turbines reducing the laser light reflection [58, 59, 78, 80, 89].

High-speed photography is another method widely used for studying two-phase flows by enabling their observation. Advanced experimental set-up and facility arrangement are essential to achieve undistorted and reliable images. There exist examples of complete optical access through the blades of a turbomachine thanks to index matching facilities [75, 109] and the employment of water boxes to mitigate the image distortion [77]. One of the major challenge for this technique is the development of an image processing method for the separation of the information coming from the two phases, especially if a high accuracy, as required for CFD validation, is sought. For instance, in the study of bubbly flows the interaction between bubbles often causes velocity fluctuations in the liquid flows that are highly dependent on the bubbles size and concentration. More problems come from the flow pattern identification. Nowadays, few automated signal interpretations have been developed and showed being independent on the experimental conditions. Moreover, increasing void fraction and turbulence generally leads to rise measurement uncertainties. Robust image processing methods are described in literature with successful applications on bubble columns [22, 31, 120], micro-channels [55, 82], vapour bubbles [28, 66] and for seabed investigations

[103].

### **Thesis objective**

The main objective of this thesis work is the experimental investigation and prediction of the power consumption in hydraulic turbines and pump/turbines when the generator of the unit is operating in synchronous condenser mode. This research challenge is addressed by means of four different contributions.

First and second goals of this research are to elucidate the hydrodynamics properties of the two main flow phenomena in Francis-type turbines and pump-turbines operating in synchronous condenser mode. These phenomena are the sloshing motion of the free-surface below the runner/impeller and the structures of the flow in the vaneless gap between the impeller blades and the closed guide vanes. Both phenomena are investigated by applying optical measurement techniques combined with pressure fluctuations measurements. Image processing is developed to determine the flow characteristics such as sloshing amplitude and frequency, bubbles dimension and velocity profiles. The experiments are performed at several operating conditions of the machine to evaluate the flow structures and their characteristics with respect to the operating parameters.

Third, the research seeks the quantification of the power consumption related to the flow interaction with the runner/impeller. Measurements of the resistant mechanical torque are performed to investigate the flow conditions at which a higher torque value is associated and to correlate the eventual torque instability to the flow structures. A model predicting the differential pressure coefficient, proportional to the mechanical torque, is built as a function of the operating parameters.

Fourth goal of this thesis is the prediction of the air losses. Measurements of the oxygen concentration in water and of the water level variation in time are performed to determine the air losses due to the mass transfer. A theoretical framework of the air diffusion is developed for the investigated system and the global diffusion coefficients for the free-surface in the vaneless gap and in the cone of the draft tube are experimentally determined. This analytical study allows predicting the air losses due to the diffusion in water over a broad range of operating parameters of the machine.

The study performed concerns the phenomena related to the hydraulic machine and neglects other electro-mechanical equipment such as bearing, generator, etc..

### **Thesis structure**

The present thesis work is a collection of peer-reviewed manuscripts published or submitted to international journals.

In **chapter 1**, the hydrodynamics of the sloshing motion of the air-water free-surface below the runner of a Francis turbine operating in synchronous condenser mode is investigated. The experimental facility and the operating conditions at which the tests are performed are illustrated. The image processing method developed to measure the amplitude and frequency of the sloshing motion and the results achieved are presented.

In **chapter 2**, the investigation of the air-water ring at  $Fr_d = 0.5$  characterized by a rotating bubbly flow is described. The experimental set-up and the image processing method for bubbles identification and tracking are presented and followed by the results achieved. A method based on the Fourier harmonic decomposition is illustrated to predict the pressure field.

In **chapter 3**, the perturbation of the resistant mechanical torque transmitted through the coupling of the impeller and the shaft is studied. In particular, this analysis focuses on the interaction of the impeller with the flow structures in the vaneless gap between the impeller blades and the closed guide vanes. The study of the torque oscillations correlated to the flow instabilities and the development of a surrogate model for the differential pressure coefficient prediction are detailed.

In **chapter 4**, the oxygen diffusion process in the water volume in the machine is investigated. The experimental method for measuring the variation of the oxygen concentration in both vaneless gap and draft tube of the hydraulic turbine and the theoretical framework describing the mass transfer process applied to the machine are presented. The determination and prediction of the air losses in the investigated system due to this phenomenon is described as well.

Finally, in **chapter 5**, a guideline is proposed as general methodology for the calculation of the power consumption in synchronous condenser operation. In particular, this guideline focuses on the computation of the power consumption due to the torque transmitted by the runner/impeller and to the air losses. An example of the application of this method to a full scale pump-turbine is provided.





# 1 Sloshing free-surface

## 1.1 Experimental investigation of the sloshing motion of the water free-surface in the draft tube of a Francis turbine operating in synchronous condenser mode

Reproduced version of:

E. Vagnoni, A. Favrel, L. Andolfatto, F. Avellan, (2018), *Experimental investigation of the sloshing motion of the water free-surface in the draft tube of a Francis turbine operating in synchronous condenser mode*, Experiments in Fluids 59(6):95. DOI:<https://doi.org/10.1007/s00348-018-2552-x>

with the permission of Springer Nature.

### **The author's contribution:**

The author performed the experiments, the data post-processing, and the development of the image processing method. She performed the data analysis for the study of the sloshing dynamics. She is the first author of this publication.

### **Abstract**

Hydropower units may be required to operate in condenser mode to supply reactive power. In this operating mode, the water level in the turbine or pump-turbine is decreased below the runner by closing the guide vanes and injecting pressurized air. While operating in condenser mode the machine experiences power losses due to several air-water interaction phenomena which cause air losses. One of such phenomena is the sloshing motion of the water free-surface below the runner in the draft tube cone of a Francis turbine. The objective of the present work is to experimentally investigate the sloshing motion of the water free-surface in the draft tube cone of a reduced scale physical model of a Francis turbine operating in condenser mode. Images acquisition and simultaneous pressure fluctuation measurements

are performed and an image processing method is developed to investigate amplitude and frequency of the sloshing motion of the free-surface. It is found that this motion is excited at the natural frequency of the water volume and corresponds to the azimuthal wavenumber  $m = 1$  of a rotating gravity wave. The amplitude of the motion is perturbed by wave breaking and it decreases by increasing the densimetric Froude number. The sloshing frequency slightly increases with respect to the natural frequency of the water volume by increasing the densimetric Froude number. Moreover, it results that this resonant phenomenon is not related to the torque perturbation.

**Keywords:** sloshing free-surface, gravity wave, image processing, pressure and torque fluctuations, Francis turbine, condenser mode.

### 1.1.1 Introduction

The penetration of intermittent renewable energies, such as wind and solar sources, in the electrical grid causes considerable power fluctuations which must be compensated to guarantee the grid stability. In this context, hydropower units can play a crucial role for the stabilization of the electrical grid by balancing consumption and production. Furthermore, they can provide reactive power for the grid stabilization by operating in condenser mode [49, 50]. In this specific operating mode, Francis turbines are operated in dewatered condition to minimize the runner resistant torque and the corresponding power losses.

The configuration of the turbine operating in condenser mode and the main components are illustrated in Fig. 1.1. In generating mode, an angular momentum is created at the runner inlet by the spiral case, stay vanes, which are used for structural stiffening as well as flow distribution, and guide vanes. The opening angle of the guide vanes controls the value of the flow rate through the runner. The angular momentum of the flow is recovered by the runner blades and yields a resulting torque acting on the shaft. The flow is then released into the draft tube, which recovers the residual kinetic energy of the flow by converting it into static pressure [35, 72]. In condenser mode, the guide vanes are closed to block the incoming discharge and pressurized air is injected in the draft tube of the machine from a storage tank to maintain the free-surface level in the draft tube below the runner. Thus, the interference of the runner with water is minimized. The evaluation of both air and power consumption is determining for the specification and proper design of the pressurizing system.

Tanaka et al. [100] described different two-phase flow phenomena observed in a reversible pump-turbine operating in synchronous condenser mode. In this work, the sloshing motion of the water free-surface and other air-water interaction phenomena such as turbulent waves causing the formation and entrainment of bubbles diffusing in the water volume and droplets interfering with the runner are observed. The sloshing motion is described as a rotating wave induced by a wind whirl of air agitated by the rotating runner. Four main stages of the sloshing motion depending on the rotational speed of the runner are described with respect to the operating conditions of the pump-turbine by applying the densimetric Froude similitude to

### 1.1. Experimental investigation of the sloshing motion of the water free-surface in the draft tube of a Francis turbine operating in synchronous condenser mode

reach the similarity with the prototype. The densimetric Froude number is defined as:

$$Fr_d = \sqrt{\frac{\rho_{\text{air}}}{\rho_{\text{water}}}} \times \frac{\omega \times \sqrt{D_e}}{\sqrt{g}} \quad (1.1)$$

where  $\omega$  is the angular speed of the runner ( $\text{rad}\cdot\text{s}^{-1}$ ),  $D_e$  (m) is the high pressure diameter of the Francis runner and  $g$  ( $\text{m}\cdot\text{s}^{-2}$ ) is the gravity.  $\rho_{\text{air}}$  and  $\rho_{\text{water}}$  ( $\text{kg}\cdot\text{m}^{-3}$ ) are the air and water density, respectively. The air density is computed from the ideal gas law by measuring the static air pressure in the cone of the draft tube and the temperature. It has been shown that the densimetric Froude number appears to be the most significant parameter in modeling many air-water interfaces [83, 96, 100, 113].

Ceravola et al. [24] investigated the free-surface wave occurring below the runner of a hydraulic machine operating in condenser mode for different geometries of the draft tube cone of a pump-turbine in both pump and turbine rotating direction. The sloshing motion is described as a rotating wave caused by dissymmetry in the water free-surface. The sloshing motion of the water free-surface below the runner can have a key role to partially understand the causes of the air losses during the dewatered operating condition of a Francis turbine.

More generally, studies were conducted to understand the behavior of an oscillating free-surface in partially filled vessels. Farid and Gendelman [37, 38] suggested a two-dimensional model to investigate moderately and strongly nonlinear two-dimensional liquid sloshing regimes; they studied the underlying dynamical mechanisms by developing a theoretical framework and comparing the results with numerical simulations. Song et al. [98] studied flow kinematics and impact pressure of a sloshing flow produced by the periodic motion of a rectangular tank. Royon-Lebeaud et al. [92] gave a thorough description of the sloshing motion in a vessel excited at different frequencies. They highlighted the interaction between different crests and evaluated the periodicity of the investigated phenomena. Komori et al. [69] showed the direct dependence of the mass transfer of a gas into water on the frequency and amplitude of the surface wave caused by a wind shear. The mass transfer plays a significant role for understanding the air diffusion in water which is one of the causes of the air losses.

As such, there has been a shortage of research into Francis turbine operating in condenser mode related to the determination of air losses and the description of the flow phenomena involved in the machine. To fulfill the qualitative and quantitative description of the sloshing motion, new experiments must be devised and applied to a Francis turbine operating in condenser mode.

Multiple experimental techniques were developed and performed to investigate the determinant parameters of water free-surfaces and, more generally, two-phase flows. In particular, high-speed photography is a non-intrusive method widely used for studying the dynamics of air-water interfaces. Proper experimental set-up and facility arrangement are essential to achieve undistorted and reliable images. Uzol et al. [109] constructed an index-matched facility, in which the refractive index of the fluid matches with the one of the transparent

## Chapter 1. Sloshing free-surface

blades to have a complete optical access through the blades of an impeller. Miorini et al. [75] used the same approach to examine flow in the tip region of a waterjet pump in cavitation conditions. Müller [78] designed a water box to mitigate the effects of optical distortion for flow visualizations in the investigation of the cavitation vortex rope in the draft tube cone of a Francis turbine operating at full load. Multiple studies performed high-speed photography in the investigation of a free-surface motion [12, 29, 122]. Reclari [89] applied high-speed photography and developed an experimental method based on the light intensity and contrast to study the physic of a gravity wave rotating in a partially filled cylindrical vessel subject to orbital shaking.

The present paper aims to describe the behavior of the sloshing motion of the water free-surface in a reduced scale physical model of a Francis turbine operating in synchronous condenser mode. Image acquisition and simultaneous pressure fluctuations measurements are performed to investigate the amplitude and the frequency of the sloshing motion and to evaluate the influence of the key parameters such as gauge pressure, densimetric Froude number and water level in the cone of the draft tube.

The experimental set-up and the image processing method to investigate the sloshing motion in a reduced scale physical model of Francis turbine operating in condenser mode are described in Sec. 1.1.2. The amplitude and frequency of the sloshing motion and the pressure measurements in both time and frequency domains are presented in Sec. 1.1.3. In particular, a study on the influence of the pressure, densimetric Froude number and water level in the draft tube on the amplitude and frequency of the sloshing motion is performed. The results are followed by a discussion in Sec. 1.1.4.

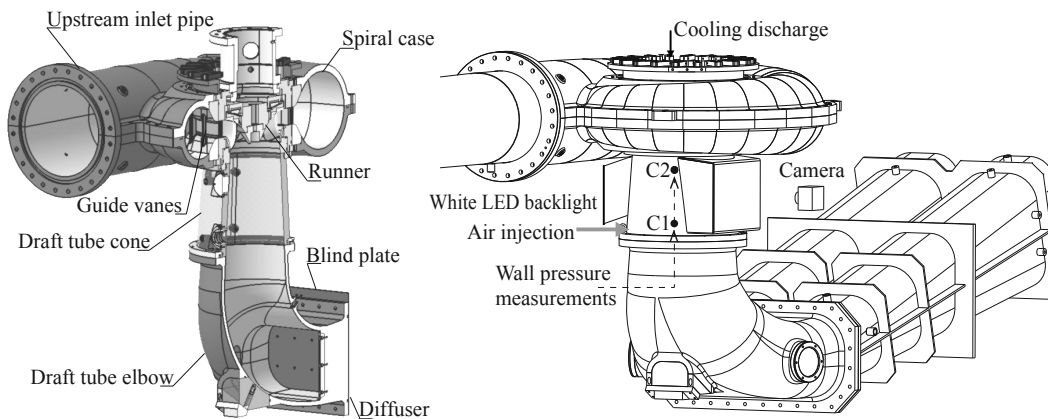


Figure 1.1 – Reduced scale physical model of the Francis turbine installed in the test rig including the main instrumentation.

## 1.1. Experimental investigation of the sloshing motion of the water free-surface in the draft tube of a Francis turbine operating in synchronous condenser mode

### 1.1.2 Methodology

#### Experimental set-up

The measurements are carried out on a 1:16 reduced scale physical model of a Francis turbine with a specific speed  $v = 0.27$  defined as follows:

$$v = \omega \cdot \frac{Q^{1/2}}{\pi^{1/2} \cdot (2 \cdot E)^{3/4}} \quad (1.2)$$

where  $Q$  the discharge and  $E$  the machine specific energy. As shown in Fig. 1.1, the reduced scale model includes the upstream inlet pipe, the spiral case, the 16 blades runner with an external diameter  $D_e = 0.405$  m and the draft tube consisting of the cone, the elbow and the diffuser. A generator connected to the model runner regulates the rotational speed. The test rig is operated in closed loop configuration and is equipped with two axial double-volute pumps to generate the specific hydraulic energy. A blind plate at the end of the draft tube is designed to reproduce the geometrical configuration of the prototype and the guide vanes are closed to operate in condenser mode. Water is injected through the labyrinth seals for cooling purpose. A system of pressurized air injection is placed in the cone of the draft tube as illustrated in Fig. 1.1, to keep the free-surface below the runner.

The visualization of the sloshing motion is performed through the transparent cone of the draft tube below the runner. The inner surface of the cone is divergent with an angle of  $\theta = 4.1^\circ$  with respect to the vertical axis. It has a diameter of 0.35 m at the inlet and 0.41 m at the outlet, is 0.39 m high and has 0.04 m thick walls. A flat water box window is installed as shown in Fig. 1.1 to minimize the optical distortion due to the conical shape. The videos of the sloshing motion inside the draft tube cone are recorded by using a camera (DFK23G445, IMAGINGSOURCE), at image acquisition rates of 30 frames per second for 60 s, and resolution of 960 pixels  $\times$  1'280 pixels. A 90% uniform LED screen (PHLOX LEDW-BL-550X400-MSLLUB-Q-1R-24V) of 500 mm  $\times$  400 mm size and 7'000 cd  $\cdot$  m<sup>-2</sup> luminescence is installed as a back light to enhance the contrast between gaseous and liquid phase.

Wall pressure measurements are performed in two sections of the draft tube cone at  $0.39 \times D_e$  (upper section) and  $1.02 \times D_e$  (lower section) downstream the runner outlet. One pressure sensor is installed in the lower section (C1) of the draft tube cone and one at the upper section (C2) as it is shown in Fig. 1.1. Both sensors are mounted on the horizontal plane at  $35^\circ$  with respect to the investigated focus plane of the camera. The dynamic wall pressure is measured by flush-mounted piezo-resistive pressure sensors. They allow for pressure measurements in the range of 0-5 bar with a maximum measurement uncertainty of 0.7 %. The sample frequency is set at 3'000 Hz and 60 s of measurements are recorded.

The acquisition chain is illustrated in Fig. 1.2: the camera triggers the pressure acquisition system (PXI) to start simultaneously photography with torque and pressure measurements.

## Chapter 1. Sloshing free-surface

Two values of gauge pressure  $p$  and six densimetric Froude numbers are tested by varying the pressure in the cone and the rotational speed of the runner  $N$  ( $\text{min}^{-1}$ ). The tested operating conditions of the machine are presented in Fig. 1.3. Moreover, all the investigated operating points are explored at three water level conditions in the draft tube cone: at  $0.91 \times D_e$  (low),  $0.77 \times D_e$  (mean) and  $0.66 \times D_e$  (high) downstream the runner outlet.

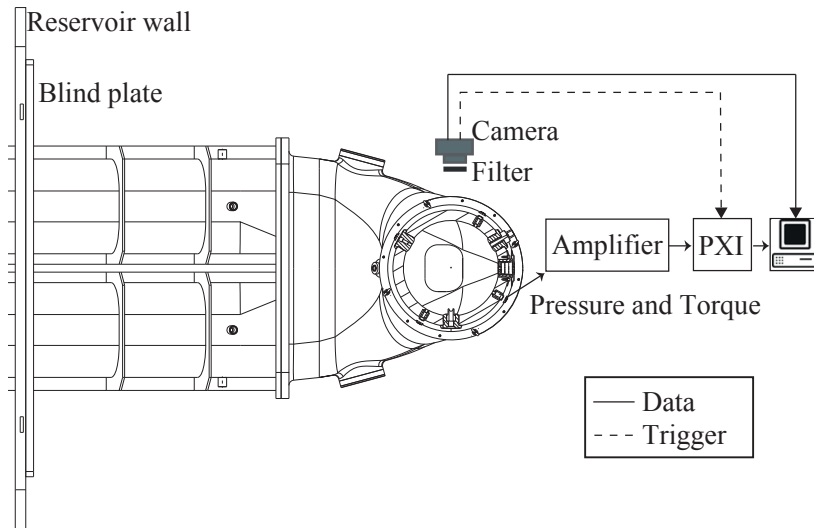


Figure 1.2 – Horizontal cut view of the draft tube at the pressure sensor lower section together with the scheme of the acquisition chain.

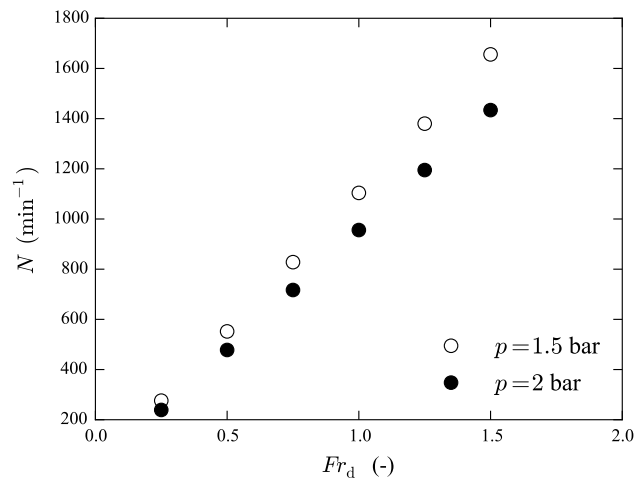


Figure 1.3 – Investigated operating conditions of the Francis turbine operating in condenser mode

## 1.1. Experimental investigation of the sloshing motion of the water free-surface in the draft tube of a Francis turbine operating in synchronous condenser mode

### Image processing method

An image processing method based on image filtering and contrast detection is developed. A similar method was employed by Müller et al. [80] to estimate the cavitation volume of the vortex rope in the cone of a Francis turbine. A calibration of the image acquisition is done before the actual measurements with a 200 mm × 200 mm dotted target located in the transparent cone and attached to the runner nose. The focus plane is centered on the central plane of the draft tube cone and a conversion ratio of 2 pixel · mm<sup>-1</sup> is derived from calibration.

The pixel discretization and the presence of bubbles and droplets induce errors in the identification of the sloshing amplitude since they can locally change the elevation of the free-surface. Instead considering the column of pixels corresponding to the wall of the draft tube cone to compute the elevation of the surface, a 30 pixels width image section close to the wall is considered to compute the inclination and finally the elevation of the free-surface. In this way, eventual perturbations which locally change the elevation of the free-surface are moderated by the trend of the surface inclination. The maximum size of the perturbation will be further discussed in the description of the method for the estimation of the uncertainty.

The image processing method applied to the images of the sloshing motion of the water free-surface is illustrated in Fig. 1.4. From each frame two matrices  $E(j, i)$  and  $F(j, i)$  of 30 pixels width are extracted at two fixed locations in the images of the draft tube cone. The matrices are optically aligned with the vertical axis of the machine thanks to the camera calibration. An adaptive threshold filter [48] is applied to identify the illuminated liquid phase in contrast with the dark background. The method to measure the difference in elevation of the two sides of the water free-surface consists in the identification of the segment  $AB$  and  $CD$  which correspond to the position and inclination of the free-surface in the extracted matrices of the image as illustrated in Fig. 1.4. As first step, the method computes for each column of pixel in the matrices the position of the free-surface on the vertical axis  $y$  introduced in the coordinate reference system in Fig. 1.4. This means solving eq. (1.3) and eq. (1.4) for each column  $i$  of the matrix of pixels  $E(j, i)$  and  $F(j, i)$ .

$$y_{AB,i} = \sum_j (E(j, i) = 255) \quad (1.3)$$

$$y_{CD,i} = \sum_j (F(j, i) = 255) \quad (1.4)$$

However, a bubble in the water volume can cause a black spot in the filtered image of the sloshing water free-surface and therefore perturb the estimation of the position of the free-

## Chapter 1. Sloshing free-surface

---

surface. To avoid this perturbation, a filling function [18] is used to ensure an uniform white liquid column. As second step, a linear regression of the data set of the computed positions of the water free-surface is performed by using the least squares best fit method. This leads to identify the segments  $AB$  and  $CD$  and the points  $B$  and  $C$  according to eq. (1.5).

$$y_B = ax_B + b \quad \text{and} \quad y_C = cx_C + d \quad (1.5)$$

In eq. (1.5),  $a$  and  $c$  are the slopes and  $b$  and  $d$  the intercepts on the  $y$ -axis of the linear equations computed by the linear regression. This leads the estimation of the difference in elevation of the two sides of the free-surface caused by the sloshing motion according to eq. (1.6):

$$h = y_B - y_C \quad (1.6)$$

The uncertainty on the measurement performed by the post-processing method is estimated by applying a Monte Carlo method [3]. A perturbation representing a droplet or a bubble which locally changes the elevation of the free-surface is introduced in the images to evaluate the influences of those physical patterns on the estimation of the amplitude of the sloshing motion.

Each image is perturbed with a 5 mm diameter black semi-circle with the center located on the estimated position of the free-surface on the  $y$ -axis and a random position on the  $x$ -axis, as it is shown in Fig. 1.4. Ten random positions on the  $x$ -axis for each original image are tested. The diameter of the black semi-circle is chosen by estimating the maximum dimension of the perturbing patterns with the visualization of the water free-surface. A series of 18'000 perturbed images for each operating point is obtained and tested by the image processing method for computing the amplitude of the free-surface. The perturbation in the images introduces a maximum uncertainty interval equal to  $\pm 3$  mm with respect to the computed difference in elevation of the two sides of the sloshing water free-surface in the images without perturbation. The maximum uncertainty is recorded at  $Fr_d = 1.5$  and  $p = 2$  bar.

### Spectral analysis

A frequency analysis of both the pressure measurement and the computed difference in elevation  $h$  is conducted to highlight the frequencies of interest related to the sloshing motion of the free-surface. This study enables the comparison of the sloshing frequency and the corresponding pressure fluctuation frequency for the investigated points and therefore, the identification of the influencing parameters on the sloshing motion. A Discrete Fourier Transform (DFT) is applied to the computed  $h$  and pressure signals to evaluate the amplitude and the frequency corresponding to the sloshing motion. Moreover, the DFT is applied to the torque signals to assess the dominant frequency of the torque oscillation and an eventual



### 1.1. Experimental investigation of the sloshing motion of the water free-surface in the draft tube of a Francis turbine operating in synchronous condenser mode

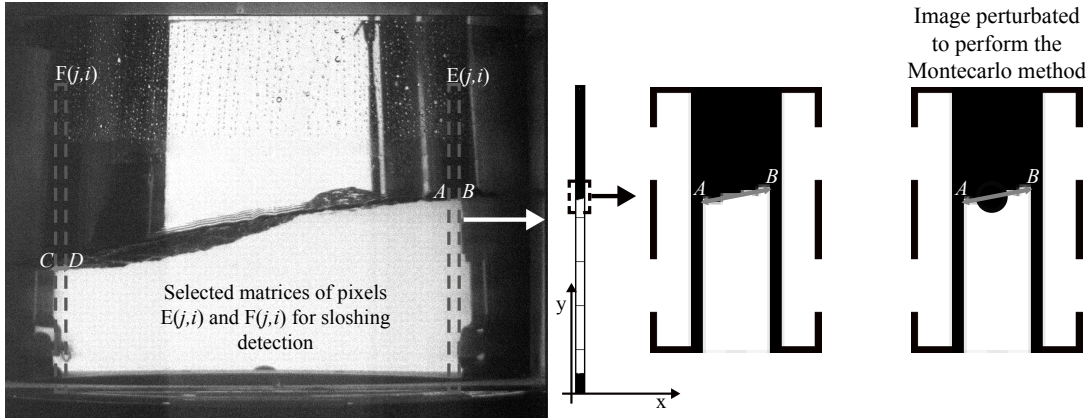


Figure 1.4 – Extracted matrices of pixels, filtering for sloshing detection and perturbation of the image to apply the Monte Carlo method.

correlation with the sloshing motion.

In Fig. 1.5(a), a sequence of images of the water free-surface during the sloshing motion is presented. The computed difference in elevation of the two sides of the sloshing water free-surface and the corresponding spectrum are presented in Fig. 1.5 as well. The frequencies of interest are below 10 Hz. The frequency of the sloshing motion, 1.78 Hz for the presented point in Fig. 1.5(c), justifies the frame rate of 30 Hz chosen for the image acquisition.

The frequency resolution of the DFT is computed as follows:

$$\sigma_f = \frac{1}{t_{\text{acq}}} \quad (1.7)$$

where  $t_{\text{acq}}$  is the time acquisition of the measurements.

The Froude number of the sloshing free-surface is introduced as a function of the measured frequency  $f$  and of the wave length  $\pi D$  of the sloshing motion as follows:

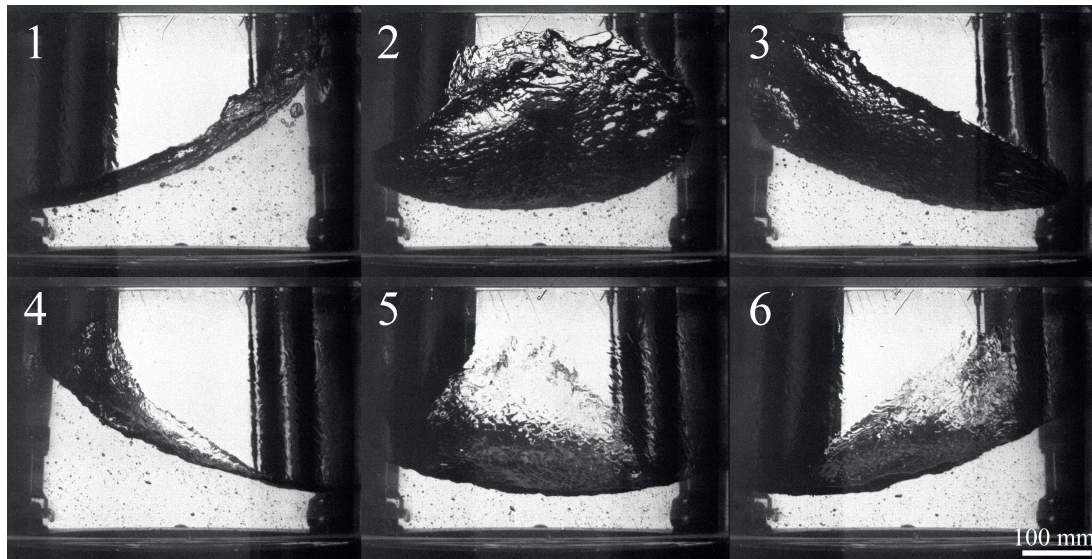
$$Fr_{\text{sloshing}} = \frac{\pi f \times D}{\sqrt{g \times \pi D}} \quad (1.8)$$

where  $D$  is the diameter of the section of the draft tube cone corresponding to the elevation of the water free-surface in steady condition.

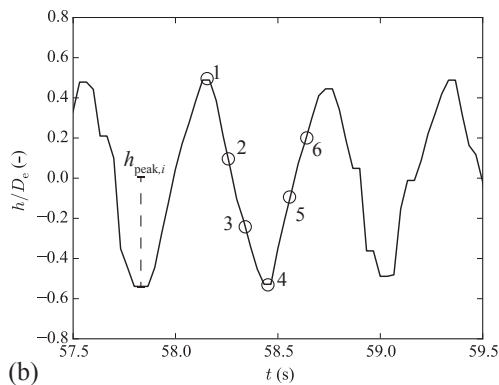
To evaluate the pressure fluctuations, the pressure data are made dimensionless by defining the pressure coefficient:

$$C_p = \frac{(p - \bar{p}) / \rho_{\text{water}}}{gl} \quad (1.9)$$

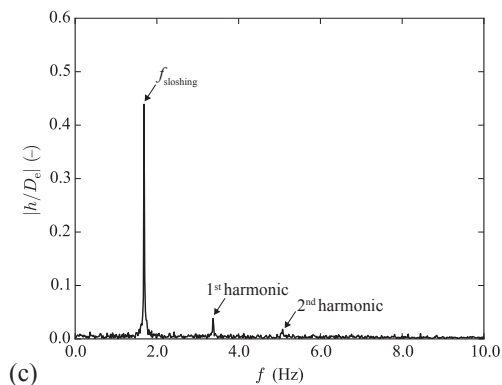
where  $l$  is the water level with respect to the horizontal axis of the elbow of the draft tube cone,



(a)



(b)



(c)

Figure 1.5 – (a) Sequence of images of the water free-surface oscillating during the condenser mode operation of the Francis runner at  $p = 2$  bar and  $Fr_d = 0.75$  with high water level condition. (b) Time resolved signal of the difference in elevation of the two sides of the sloshing water free-surface measured with the image processing method. (c) Corresponding spectrum magnitude of the signal in (b).

$p$  is the instantaneous pressure measured by the sensor C1 or C2 and  $\bar{p}$  the average value.

To evaluate the torque fluctuations, the torque data are made dimensionless by defining the torque factor:

$$T_{ED} = \frac{(T_m - \overline{T_m})/\rho_{\text{air}}}{D_e^3 \times U_{\text{tip}}^2/2} \quad (1.10)$$

where  $U_{\text{tip}}$  is the peripheral velocity of the blade tip,  $T_m$  is the instantaneous torque transmitted through the coupling of the runner and the shaft measured by the torquemeter and  $\overline{T_m}$  the

### 1.1. Experimental investigation of the sloshing motion of the water free-surface in the draft tube of a Francis turbine operating in synchronous condenser mode

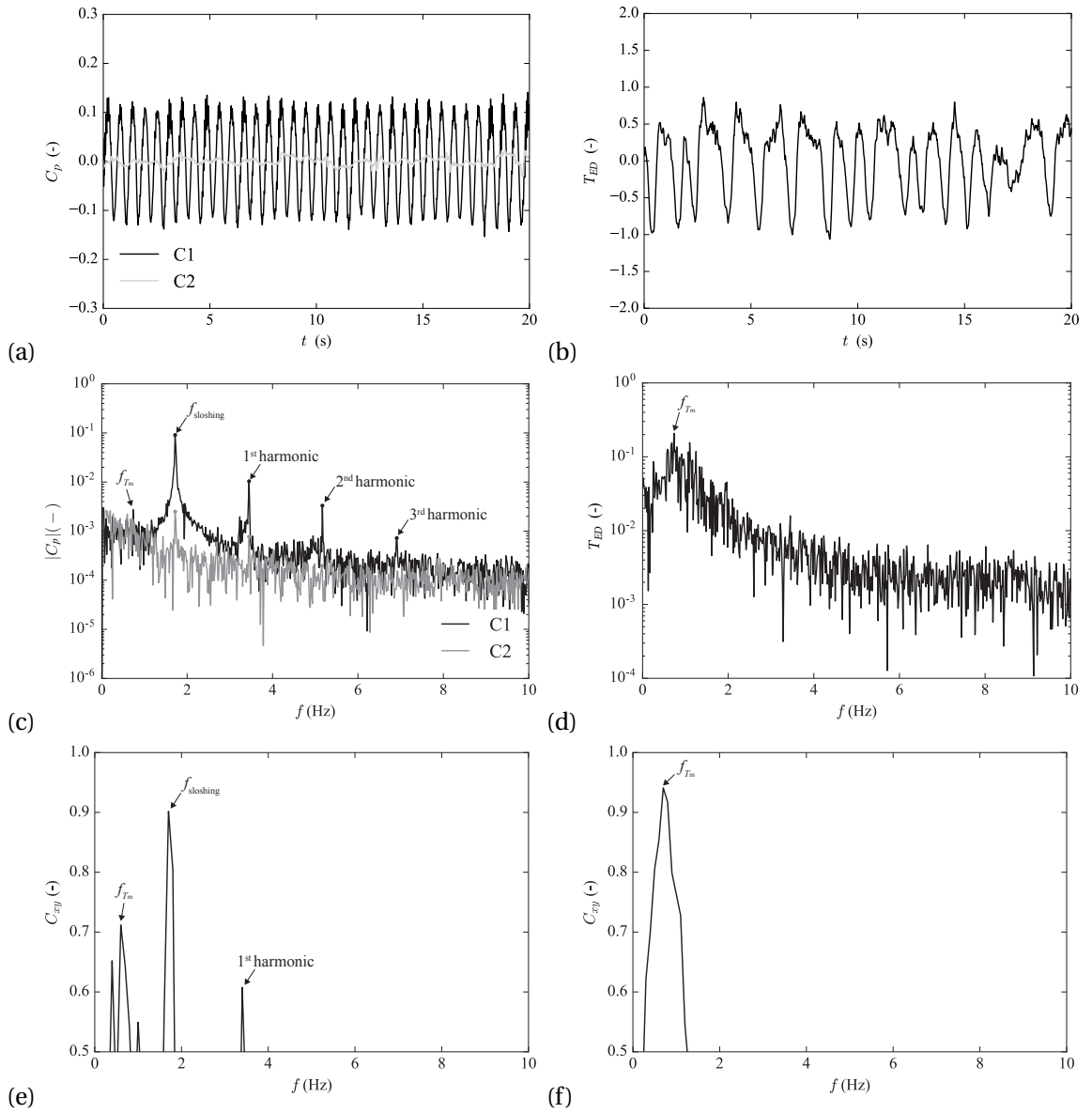


Figure 1.6 – Time history of the pressure coefficients C1 and C2 (a) and torque factor (b). Spectra in logarithmic scale of C1 and C2 (c) and of the torque signal (d). Coherence between the two pressure fluctuations measurements C1 and C2 (e) and coherence between the torque signal and C1 (f). All results are shown for  $Fr_d = 1$  at  $p = 1.5$  bar with high water level condition.

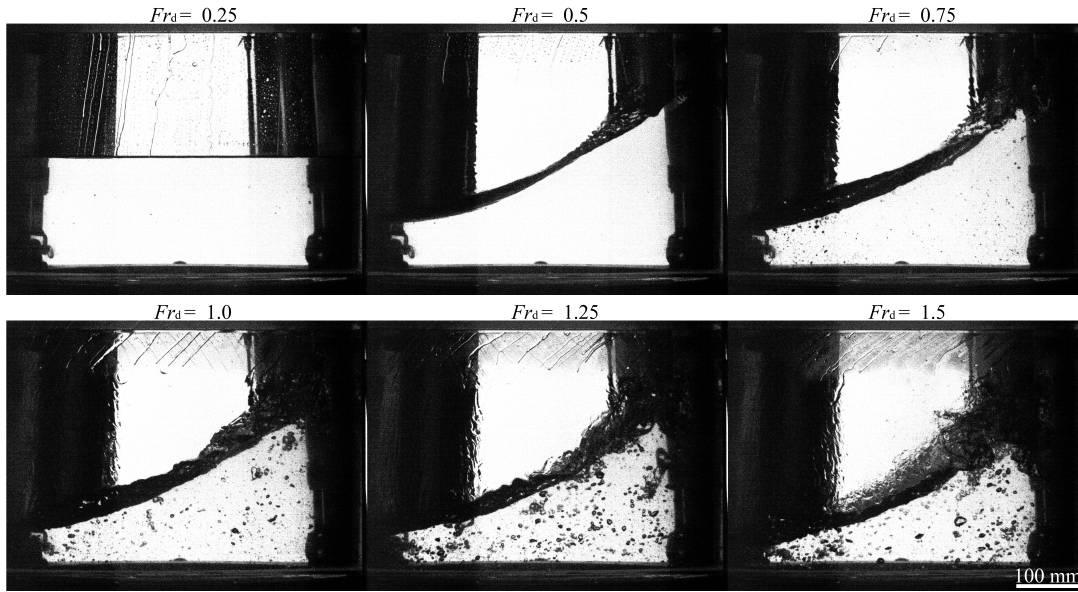


Figure 1.7 – Typical images of the sloshing motion of the free-surface in the draft tube cone of a Francis turbine operating in condenser mode at  $p = 2$  bar for the six investigated densimetric Froude number values.

average value.

The time history of both pressure measurements at the locations C1 and C2 and torque measurement is illustrated in Fig. 1.6(a) and (b), respectively, at  $Fr_d = 1$ ,  $p = 1.5$  bar with high water level condition. The pressure sensor at the upper section is above the water free-surface for all the water level conditions. A low-pass filter with a cut-off frequency of 30 Hz is applied to filter the noise. A study on the pressure and torque fluctuations measurements is performed by spectral analysis. As illustrated in Fig. 1.6(c), the spectra of the pressure signals at the location C1 and C2 make apparent the frequency of the sloshing motion and its harmonics. The fluctuations at the sloshing frequency are dominant at C1 while they are  $10^2$  times lower at the location C2. Moreover, in both spectra it is observed an oscillation at a frequency  $f_{T_m}$  lower than the sloshing motion frequency. The amplitude of this oscillation has the same order of magnitude as the amplitude of the oscillation at the sloshing motion frequency at C2.

A cross-spectral analysis between the pressure measurements at the location C1 and C2 is performed. It includes the computation of the coherence  $C_{xy}$  of the two signals in the frequency domain, presented in Fig. 1.6(e). It is noticed that the peak coherence with  $C_{xy} > 0.9$  corresponds to the frequency of the sloshing motion and that a lower peak appears at  $f_{T_m}$ .

The spectrum of the torque signal is illustrated in Fig. 1.6(d). A peak frequency, which corresponds to  $f_{T_m}$ , observed in both spectra of the pressure fluctuations, is made apparent, while the fluctuation at  $f_{sloshing}$  is limited. This is confirmed by computing the coherence of the pressure at C1 and the torque signals, presented in Fig. 1.6(f): it is noticed that there is a lack

### 1.1. Experimental investigation of the sloshing motion of the water free-surface in the draft tube of a Francis turbine operating in synchronous condenser mode

of coherence at the sloshing frequency. The absence of torque oscillation at  $f_{\text{sloshing}}$  means that the pressure wave caused by the sloshing motion does not affect the torque while there are possibly other phenomena which cause torque fluctuations and influence the pressure oscillations in the cone as well. This result will be further discussed in Sec. 1.1.3.

Moreover, the RMS of the pressure coefficient is estimated as defined in eq. (1.11):

$$\text{RMS} = \sqrt{\frac{1}{n} \sum_{k=1}^n (C_{p,k})^2} \quad (1.11)$$

where  $n$  is the number of samples.

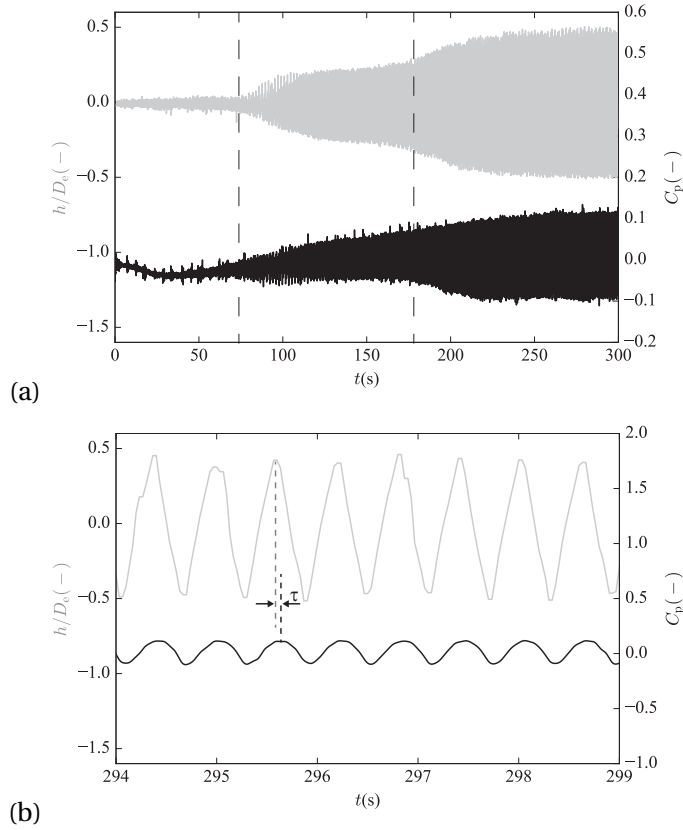


Figure 1.8 – Simultaneous time history of the difference in elevation of the two sides of the sloshing water free-surface extracted by the image processing and pressure coefficients derived from pressure measurements at the lower section of the draft tube cone at  $p = 2$  bar,  $Fr_d = 0.5$ .

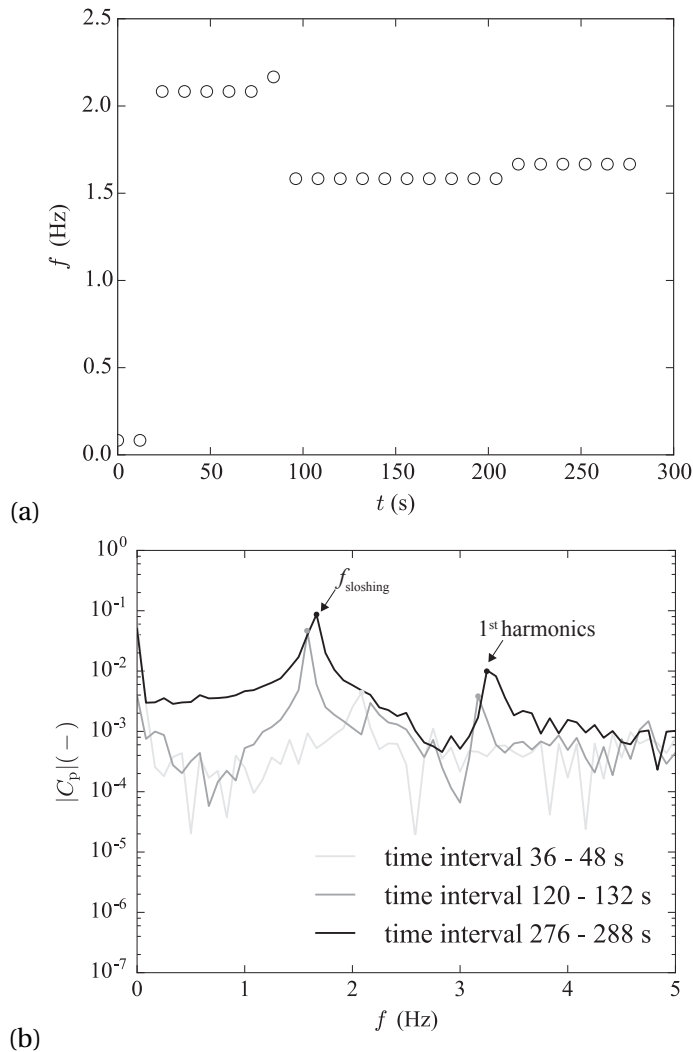


Figure 1.9 – (a) Time history of the frequency of the pressure fluctuations derived from pressure measurements at the lower section of the draft tube cone at  $p = 2$  bar,  $Fr_d = 0.5$ . (b) Spectrum magnitude in logarithmic scale of the pressure signal at different time interval.

### 1.1.3 Results

#### Transient condition at low densimetric Froude number

The observation of the sloshing motion of the water free-surface presented in Fig. 1.5(a) allows the qualitative description of the motion as a rotating gravity wave. The rotating propagation direction is the same as the runner rotating direction, as it was previously observed [24, 100].

The image processing is applied to the visualizations of the sloshing motion of the water free-surface, enabling a quantitative description of the oscillation for the investigated values of the densimetric Froude number. The water free-surface behavior in the draft tube cone

### 1.1. Experimental investigation of the sloshing motion of the water free-surface in the draft tube of a Francis turbine operating in synchronous condenser mode

for the six investigated values of  $Fr_d$  at  $p = 2$  bar at high water level condition is shown in Fig. 1.7. For  $Fr_d < 0.5$  the sloshing motion of the free-surface does not trigger. The oscillation of the free-surface is observed for  $Fr_d > 0.5$ . At  $Fr_d = 0.5$  a transient condition of the water free-surface is observed. The difference in elevation of the two sides of the sloshing water free-surface and the pressure fluctuation measurements at  $p = 2$  bar,  $Fr_d = 0.5$  are shown in Fig. 1.8(a).

The oscillation of the water free-surface increases in amplitude until stable conditions are reached. It is observed that the oscillation, which starts from the flat steady condition, develops until the sloshing amplitude reaches its maximum. The pressure fluctuation measured at the lower section of the draft tube cone also confirms the transient condition of the sloshing motion of the water free-surface at this operating point.

The increase in elevation of the water free-surface is followed by an increase of the pressure coefficient as shown in Fig. 1.8(b). The phase shift between the peak of the computed difference in elevation of the two sides of the sloshing water free-surface and the one of the pressure fluctuation is due to the geometrical shift between the angular position of the pressure sensor and the focus plane of the camera. This geometrical shift produces an off-set  $\tau = \frac{T}{10}$ , where  $T$  is the period of the free-surface oscillation.

The frequency of the oscillation also changes during the transition as shown in Fig. 1.9(a). The transition is characterized by an initial oscillation at low amplitude and frequency  $f = 2.1$  Hz as shown in the spectrum in Fig. 1.9(b). Then, the oscillation evolves in a sloshing motion by increasing its amplitude and the frequency decreases to  $f = 1.6$  Hz. Finally, the sloshing motion reaches the maximum amplitude with a constant oscillation at  $f = 1.7$  Hz.

#### Influence of the densimetric Froude number on the sloshing motion of the water free-surface and pressure oscillation

The influence of the densimetric Froude number on the Froude number of the sloshing free-surface is shown in Fig. 1.10(a) for the operating points at  $p = 1.5$  bar and  $p = 2$  bar. An increase of 13% of the frequency is observed when the densimetric Froude number increases from  $Fr_d = 0.5$  to  $Fr_d = 1.5$ .

The amplitude of the sloshing motion  $\bar{h}_{peak}$  is computed by evaluating the average peak value of  $h$  as illustrated in Fig. 1.5(b) and in the following equation:

$$\bar{h}_{peak} = \frac{1}{n_{peak}} \sum_{i=1}^{n_{peak}} |h_{peak,i}| \quad (1.12)$$

where  $n_{peak}$  is the number of peaks of the measured  $|h|$ . The standard deviation of the peak value of  $h$  is computed as well.

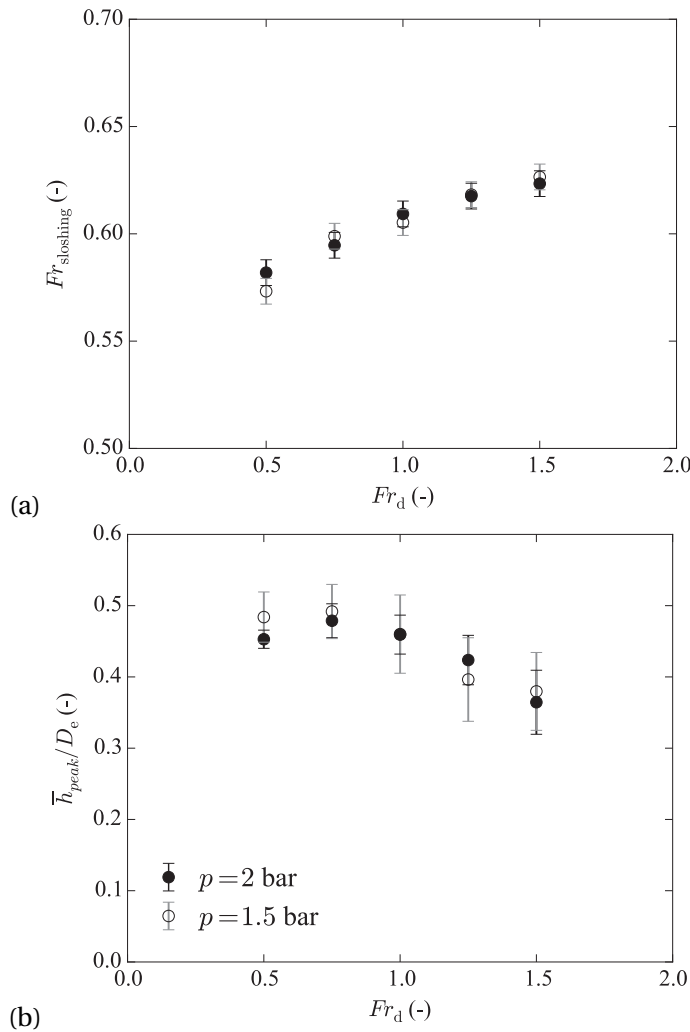


Figure 1.10 – (a) Froude number of the sloshing free-surface. (b) Measured amplitude of the sloshing motion divided by the high pressure diameter of the Francis runner.

The decrease of the sloshing amplitude by increasing the densimetric Froude number is shown in Fig. 1.10(b) for the operating points at  $p = 1.5$  bar and  $p = 2$  bar at high water level condition. The amplitude of the sloshing motion is represented in dimensionless term by dividing the measured amplitude by the high pressure diameter of the Francis runner. The images of the sloshing motion, presented in Fig. 1.7 enable the observation of the behavior of the wave crest: by increasing the  $Fr_d$  value the wave crest breaks by causing the detachment of droplets from the crest and the entrainment of air in the water volume. Both phenomena explain the decrease of the sloshing amplitude.

The influence of the densimetric Froude number on the RMS of pressure coefficient for the investigated points with high water level condition is illustrated in Fig. 1.11. Due to the wave breaking on the free-surface for  $Fr_d > 0.5$ , the RMS of the pressure coefficient is not



### 1.1. Experimental investigation of the sloshing motion of the water free-surface in the draft tube of a Francis turbine operating in synchronous condenser mode

significant for evaluating the amplitude of the sloshing motion since the wave breaking causes a stochastic perturbation of the local pressure.

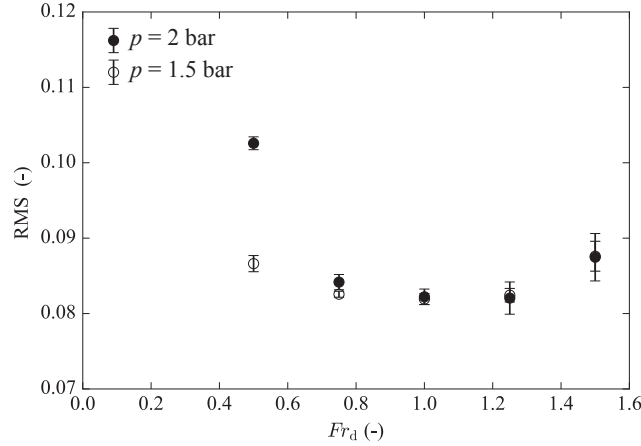


Figure 1.11 – Influence of the densimetric Froude number on the RMS of the pressure coefficient at C2 at high water level condition.

#### Influence of the gauge pressure

As illustrated in Fig. 1.10, the amplitude and Froude number of the sloshing motion of the water free-surface is not influenced by the gauge pressure for the investigated range of parameters. The RMS of the pressure coefficient also is independent of the gauge pressure, as illustrated in Fig. 1.11. The independence of the sloshing motion from the gauge pressure is a consequence of using the densimetric Froude number as scaling parameter for the operating points. It confirms the interest of using this parameter to study the sloshing motion of the free-surface since it allows reducing the number of variables influencing the motion.

#### Influence of the water level in the draft tube cone

To evaluate the influence on the sloshing motion of the water level in the cone of the draft tube, the tests are repeated with three different water volumes as explained in Sec. 1.1.2. The visualization is partially disturbed by the non-transparent part of the draft tube cone for the mean and low water level conditions. Therefore, the evaluation of the frequency of the sloshing motion is performed by computing the frequency of the pressure fluctuations. The influence of the densimetric Froude number on the Froude number of the sloshing free-surface for the investigated points at  $p = 1.5$  bar for the three water levels in the draft tube cone are presented in Fig. 1.12(a). A small influence of the water level on the  $Fr_{\text{sloshing}}$  value is observed.

The RMS of the pressure coefficient for the three water levels as a function of the densimetric Froude number is shown in Fig. 1.12(b). It is noticed a variation of the RMS value for  $Fr_d = 0.5$  which will be further discussed in Sec. 1.1.4. For  $0.5 < Fr_d < 1.25$  the RMS slightly fluctuates

and it increases at  $Fr_d > 1.25$ . As already discussed in Sec. 1.1.3 the amplitude of the pressure fluctuations is perturbed by the wave breaking which might explain the difference in trends of the RMS value for each water level. The small influence on both frequency and RMS of the pressure fluctuations further backs up the interest on the densimetric Froude number as it proves to be the only variable on which the amplitude of the sloshing motion depends.

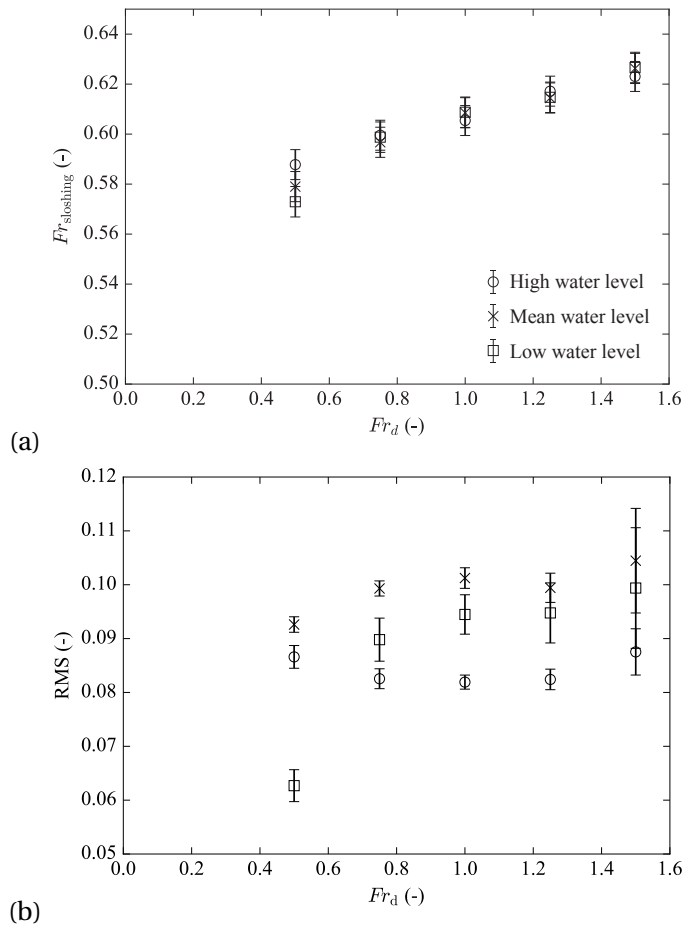


Figure 1.12 – Influence of the densimetric Froude number on the Froude number of the sloshing free-surface (a) and on the RMS of the pressure coefficient (b) for the three investigated water levels at  $p = 1.5$  bar.

### Correlation torque and pressure oscillations

As shown in Fig. 1.13, the dominant frequency of the pressure oscillation at C1 coincides to the frequency of the sloshing motion at the investigated  $Fr_d$  values. On the other side, the torque oscillation at the sloshing frequency is limited. Torque fluctuations are characterized by a dominant frequency  $f_{T_m}$  which increases by increasing the  $Fr_d$  value but this frequency and the sloshing motion frequency mismatch. This is confirmed by computing the coherence of the torque and the pressure signals at  $f_{sloshing}$  as presented in Sec. 1.1.2 and illustrated in

### 1.1. Experimental investigation of the sloshing motion of the water free-surface in the draft tube of a Francis turbine operating in synchronous condenser mode

Fig. 1.14(a) at the investigated  $Fr_d$  values. The sloshing motion and the consequent local variation of the pressure in the draft tube cone do not influence the resistant torque at the runner shaft, as previously observed by Ceravola et al.[24]. The increase of the amplitude and frequency of the torque oscillation is likely caused by other air-water phenomena in the runner due to the cooling water injection in the runner through the labyrinth seals and water entrainment in the runner. For instance, the formation of a water film around the runner due to the centrifugal force could elucidate the causes of the torque fluctuations [100]. These phenomena are influenced by the rotational speed of the runner which could explain the increasing frequency of the torque oscillations by increasing the  $Fr_d$ .

In Fig. 1.14(b) the coherence value of C1, C2 and the torque signals at the frequency  $f_{T_m}$  is presented. As also noticed in Sec. 1.1.2, the oscillation at this frequency appears in the spectra of both pressure coefficients since a high coherence value is computed for all the investigated operating points. The phenomena causing the determinant torque fluctuations produce vibrations which propagate in the draft tube cone and generate a pressure oscillation which has the same order of magnitude as the oscillation caused by the sloshing motion in the air volume, as previously observed in Fig. 1.6(c). In the water volume these vibrations are less significant than the oscillations generated by the sloshing motion of the free-surface.

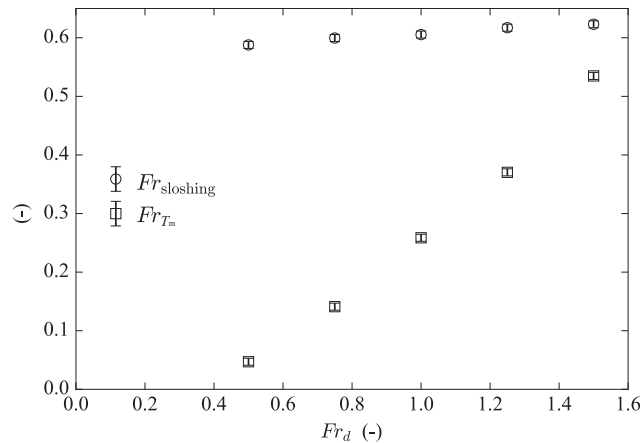


Figure 1.13 – Influence of the densimetric Froude number on the frequency of the sloshing motion and torque oscillation at  $p = 1.5$  bar and high water level condition.

#### 1.1.4 Discussion

##### Onset of the sloshing motion

Previous studies showed that the sloshing motion of a partially filled tank is a resonance phenomenon generated by the vibration of the walls [62]. Indeed, the excitation force causing the development of the rotating gravity wave could come from the vibrations of the draft tube walls produced by the runner rotation, whose rotational speed increases by increasing the

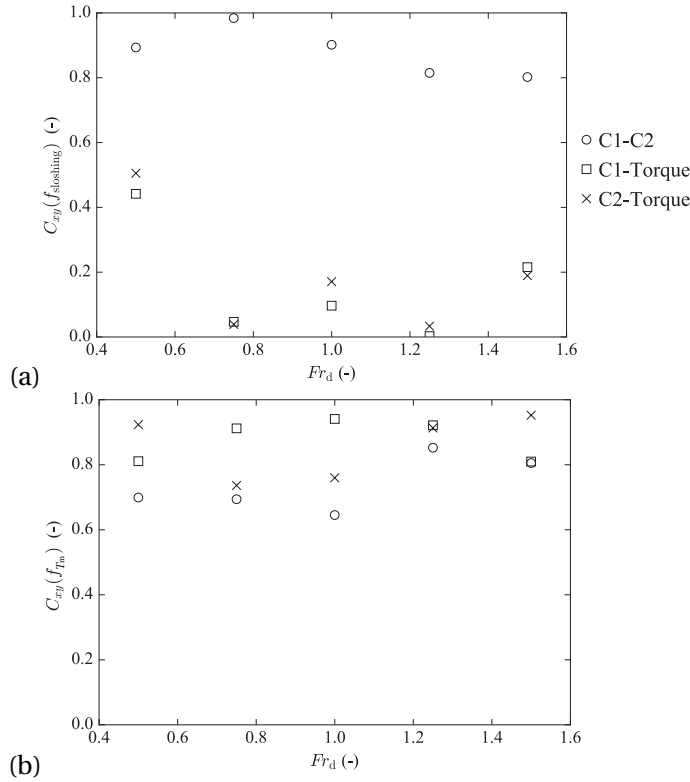


Figure 1.14 – (a) Coherence at the sloshing frequency. (b) Coherence at the dominant frequency of the torque oscillation. All results are shown for all the investigated  $Fr_d$  values at  $p = 1.5$  bar and high water level condition.

$Fr_d$ .

On the other hand, Mujica et al. [76] experimentally investigated the development of a resonant structure dominated by an azimuthal wavenumber  $m = 1$  in a highly turbulent free-surface Taylor-Couette flow. The development of the non-linear rotating wave is justified by the bifurcation of the base-state flow to the gravity wave state due to turbulent fluctuations on the free-surface.

The rotating runner causes the formation of a strong whirlwind above the free-surface which forces the water surface to a rotating axisymmetric base-state flow due to shear stresses. The development of an instability and the high turbulence level characterizing the draft tube cone of a turbine, Reynolds number  $Re = (\omega \cdot (D/2)^2) / \nu_{\text{water}}$  in the range  $1.6 \times 10^6 - 6.5 \times 10^6$ , might explain the bifurcation to the gravity wave state starting from the base-state flow generated by the shear stresses of the air turbulent flow above.

## 1.1. Experimental investigation of the sloshing motion of the water free-surface in the draft tube of a Francis turbine operating in synchronous condenser mode

### Amplitude of the sloshing motion

The image processing showed a decrease in amplitude of the sloshing motion by increasing the densimetric Froude number. From the image processing it is observed that by increasing the densimetric Froude number, wave breaking occurs and a large amount of droplets are detaching from the crest of the gravity wave and sucked by the runner [92, 100]. As a consequence, the amplitude of the water free-surface oscillation decreases. This explains also the perturbation of the RMS of the pressure coefficient by varying the  $Fr_d$  value.

In Fig. 1.12(b) it is observed that the water level does not significantly influence the RMS of the pressure coefficient, except for the operating condition at  $Fr_d = 0.5$ . At this operating point the transition of the water free-surface from a flat steady condition to maximum oscillation condition is observed. The time of the transient state of the water free-surface is difficult to determine and often random as previous works in literature demonstrated [89]. Indeed, it is possible that the measurements at  $Fr_d = 0.5$  did not record the full developed sloshing motion for the low water level condition.

### Frequency of the sloshing motion

As shown in Fig. 1.10(b), the densimetric Froude number influences the frequency of the oscillation of the water free-surface, while the gauge pressure has a limited influence. The frequency of the sloshing motion increases by increasing the densimetric Froude number, being proportional to the rotational speed of the runner.

The water volume of a partially filled cylindrical tank is characterized by a natural frequency given by the following equation [70]:

$$f_{\text{wave}} = \frac{1}{2\pi} \sqrt{\frac{\xi g}{D/2} \tanh\left(\frac{\xi l}{D/2}\right)} \quad (1.13)$$

where  $\xi = 1.84$  for a cylindrical container. The solution of eq. (1.13) for the water volume in the cone of the draft tube of a Francis turbine is illustrated in Fig. 1.15 for the three water level conditions. The ratio between  $D$  and  $l$  is taken into account since the walls of the cone of the draft tube are divergent and the deep water condition  $l > D$  is not satisfied [70, 117]. The above expression approaches a constant value for  $l \simeq D$  [57], indeed the natural frequency could be approximated to  $f_{\text{wave}} = \frac{1}{2\pi} \sqrt{\frac{\xi g}{D/2}}$  by increasing the water level.

The spectral analysis on both the elevation of the free-surface and the pressure in the draft tube cone confirm that the dominant frequency of the sloshing motion is the free-surface gravity wave natural frequency plus a small correction which depends on the densimetric Froude number  $f_{\text{sloshing}} = f_{\text{wave}} + \delta f(Fr_d)$ , as previously observed by Mujica et al. [76] who correlated the small correction to the Reynolds number. The frequency of the sloshing motion is close to the natural frequency of the free-surface gravity wave, it differs by 3 % from the minimum measured frequency of the sloshing motion. Moreover, because of the nonlinear

feature of the sloshing problem, it has been observed that resonance does not occur exactly at the natural frequency of the fluid as computed using eq. (1.13), but at a frequency very close to that value [8, 62].

This difference in frequency can be also partially due to the divergent shape of the wall of the draft tube cone since eq. (1.13) with  $\xi = 1.84$  is validated for cylindrical vessels.

The frequency of the sloshing motion depends also on the quiescent water level. The natural frequency depends on the diameter of the water free-surface as shown by the solution of the wave equation in cylindrical tank in eq. (1.13) [36]. Indeed, the natural frequency increases since the diameter of the water free-surface decreases by increasing the water level due to the divergent shape of the cone of the draft tube where the experiments are performed. Moreover, due to the complexity of the machine, it is expected that vibrations excite the wall of the draft tube cone within a range of frequencies which depend on the rotational speed of the runner. This might explain the influence of the densimetric Froude number on the frequency of the sloshing motion owing to the increase of the rotational speed of the runner which slightly accelerates the sloshing motion.

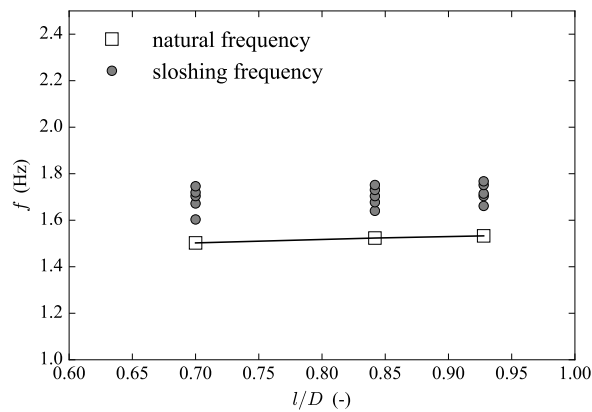


Figure 1.15 – Natural frequency of the water volume and frequency of the sloshing motion as a function of the water level  $l$  divided by the inner diameter of the cone  $D$  at  $p = 1.5$  bar for the investigated  $Fr_d$  values.

### 1.1.5 Summary and Conclusion

The amplitude and frequency of the sloshing motion of the water free-surface of a reduced scale physical model of a Francis turbine operating in condenser mode are studied and the influence of the densimetric Froude number, gauge pressure and water level in the cone of the draft tube are investigated.

Image acquisition is performed in the cone of the draft tube. A method based on image processing to identify the amplitude and frequency of the sloshing motion is developed and

### **1.1. Experimental investigation of the sloshing motion of the water free-surface in the draft tube of a Francis turbine operating in synchronous condenser mode**

---

described in the present paper. In addition, pressure and torque measurements are performed. The results of the pressure measurements are compared in both time and frequency domains with the results obtained by the image processing.

The influence of the densimetric Froude number on the amplitude and frequency of sloshing motion of the water free-surface is investigated for six operating conditions in condenser mode and by measuring the corresponding pressure fluctuations and sloshing amplitude. Measurements are conducted at  $p = 1.5$  bar and  $p = 2$  bar to understand the influence of the pressure on the sloshing motion. Higher pressures values could not be reached because of the pressure design limitation of the reduced scale physical model. Moreover, measurements are performed at three water level conditions in the draft tube cone.

The results of image processing highlight that the motion of water free-surface is a rotating gravity wave whose frequency and amplitude depend on the densimetric Froude number. By increasing the  $Fr_d$  value, a decrease of the amplitude and an increase of the frequency of the sloshing motion are observed.

Pressure measurements in the lower and upper section of the draft tube confirm the results obtained by performing the post-processing of the images acquisition: pressure fluctuations correspond to the surface oscillation. The study and control of the sloshing motion on a machine without optical access can be performed by measuring the pressure fluctuations in the section corresponding to the water volume in the cone of the draft tube.

A study on the natural frequency of the water volume shows that its value is close to the frequency of the sloshing motion which corresponds to the azimuthal wavenumber  $m = 1$  of a gravity wave.

The measurements of the torque fluctuation show a mismatch between the dominant frequency of the torque oscillation and the sloshing motion frequency. The frequency of the torque oscillation increases by increasing the densimetric Froude number and appears in both spectra of the pressure fluctuations as well, while there is a lack of torque fluctuation at the sloshing frequency.

In light of the presented results, the parameters influencing the sloshing motion of the water free-surface in the draft tube cone are identified. In particular, the densimetric Froude number plays a key role in the behavior of the air-water interaction in Francis turbine operating in condenser mode. The results are of interest for the design and refurbishment of new machines which will be required to operate in condenser mode. The results back up the interest in performing similar experiments at higher gauge pressure condition to confirm the densimetric Froude similarity on a wider range of operating condition. Moreover, it would be interesting to perform a study on the estimation of the void fraction and of the air diffusion into the water volume due to the sloshing motion to minimize the air consumption.

## 1.2 Non-linear liquid sloshing in a cylindrical tank forced by a rotating fan

### 1.2.1 Introduction

In the previous section it has been observed the sloshing motion of the free-surface in the draft tube cone of a turbine and the consequences on the pressure fluctuations in the machine. However, the origin of this motion is still not fully understood due to the possible influence of the fluid-structure interaction in the draft tube cone of the machine. The liquid sloshing is a physical phenomenon of increasing interest in many other industrial applications, such as bio-reactors and spacecraft, which require or must deal with liquid sloshing [13, 105]. In literature, several studies have been conducted on the non-linear sloshing in rectangular and cylindrical tank excited by an external forcing acting on the tank walls [47, 68] or by a rotating inner cylinder [76], however, there is a lack in the investigation of the non-linear sloshing excited by a rotating fan on top of the free surface. Indeed, a fundamental study on the dynamics and on the causes provoking the onset of the sloshing motion due to a rotating fan must be carried out to highlight the physics governing the excitation of the sloshing free surface, in particular, to fully understand the behavior of the liquid volume in the draft tube of a Francis turbine.

In this section, the study of the liquid sloshing in a partially filled cylindrical tank produced by the air flow exiting a rotating fan located on top of the tank is performed. Images acquisition and post-processing are performed to estimate the amplitude and frequency of the sloshing motion. The water depth, the gap between the fan and the water free-surface and the rotational speed of the fan are the main parameters which are evaluated to understand the causes of the liquid sloshing and the influence of these parameters on the sloshing dynamics.

### 1.2.2 Experimental set-up

#### Facility and instrumentation

The experiments are performed in a partially filled cylindrical tank of internal diameter  $D = 0.189$  m, as illustrated in Fig. 1.16. The fan located on top of the tank is a commercial axial fan 6424 EBM-Papst of  $172 \times 150 \times 51$  mm size which produces a maximum air discharge  $Q_{\text{air}} = 410 \text{ m}^3 \cdot \text{h}^{-1}$ .

The visualization of the sloshing motion is performed through the transparent tank. The videos are recorded by using a camera (DFK23G445, IMAGINGSOURCE), at image acquisition rates of 30 frames per second for 60 s, and resolution of  $960 \text{ pixels} \times 1'280 \text{ pixels}$ . A 90 % uniform LED screen (PHLOX LEDW-BL-550X400-MSLLUB-Q-1R-24V) of  $500 \text{ mm} \times 400 \text{ mm}$  size and  $7'000 \text{ cd/m}^2$  luminescence is installed as a back light to enhance the contrast between gaseous and liquid phase.



## 1.2. Non-linear liquid sloshing in a cylindrical tank forced by a rotating fan

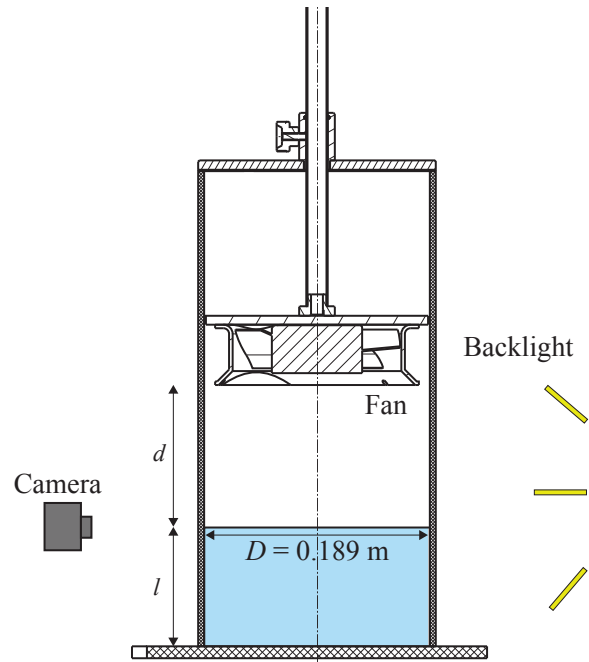


Figure 1.16 – Scheme of the test facility with the instrumentation.

Table 1.1 – Range of the parameters during the experimental investigation.

Parameter	Min	Max
$N$	$1000 \text{ min}^{-1}$	$2000 \text{ min}^{-1}$
$l$	0.05 m	0.2 m
$d$	0.1 m	0.25 m

### Parameters

Experiments are performed by varying the rotational speed of the fan, the water level  $l$  in the tank, and the gap  $d$  between the air-water free-surface and the exit section of the fan. For each test, a constant gap between the free surface and the fan is imposed to allow the full development of a sloshing wave. The lower and upper bounds of these parameters are summarized in Tab. 1.1

### 1.2.3 Characterization of the non-linear liquid sloshing

#### Sloshing amplitude peak to peak

Images of one cycle of the sloshing motion of the air-water free-surface are presented in Fig.1.17 where  $T$  is the period of the sloshing motion, as illustrated in Fig. 1.18(a). In Fig. 1.19, the images representing the free-surface at the maximum amplitude are presented for the investigated rotational speeds of the fan. Wave breaking is observed for  $N \geq 1500 \text{ min}^{-1}$ .

## Chapter 1. Sloshing free-surface

The image post-processing method presented in Sec. 1.1.2 is applied to the recorded images to measure the amplitude of the oscillation of the free-surface. The amplitude of the sloshing motion, measured as peak to peak of the elevation of the free-surfaces, is presented in Fig. 1.20(a) as a function of the rotational speed of the fan. It is noticed that the amplitude increases with the rotational speed of the fan until wave breaking occurs, and then it decreases.

An influence of the water depth is noticed, in particular for  $l \ll D$  which corresponds to a lack in fulfilling the deep water condition. For  $l \ll D$  the bottom wall influence is important and plays a crucial role in limiting the development of the sloshing motion of the free-surface. It is observed that the higher the water depth, the higher is the amplitude of the sloshing motion.

Moreover, it is observed that there is a weak influence of the gap between the water free-surface and the fan on the amplitude of the sloshing motion.

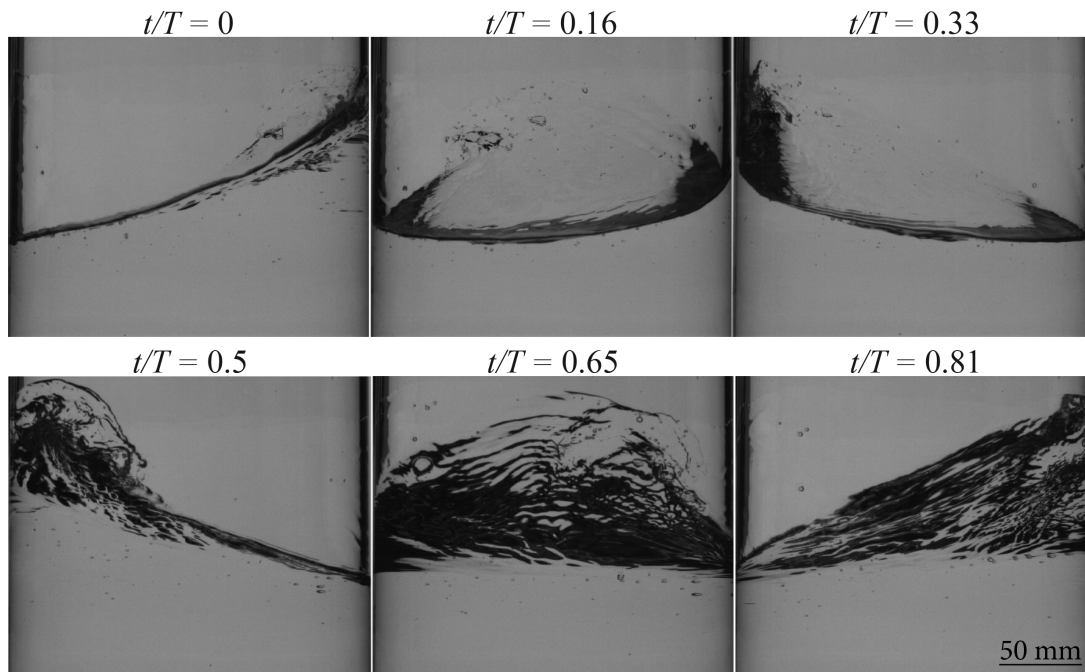


Figure 1.17 – Images of one rotation of the sloshing motion of the free-surface at  $N = 1300 \text{ min}^{-1}$ ,  $l = 0.1 \text{ m}$  and  $h = 0.25 \text{ m}$ .

### Sloshing frequency

The application of the Fourier transform on the signal of the amplitude of the sloshing motion allows computing the spectrum of the signal and to highlight the frequency of the sloshing motion as illustrated in Fig. 1.18(b). The frequency of the sloshing motion as a function of the rotational speed of the fan is illustrated in Fig. 1.20(b). It is noticed that the frequency of the sloshing motion increases by increasing the rotational speed of the fan.

## 1.2. Non-linear liquid sloshing in a cylindrical tank forced by a rotating fan

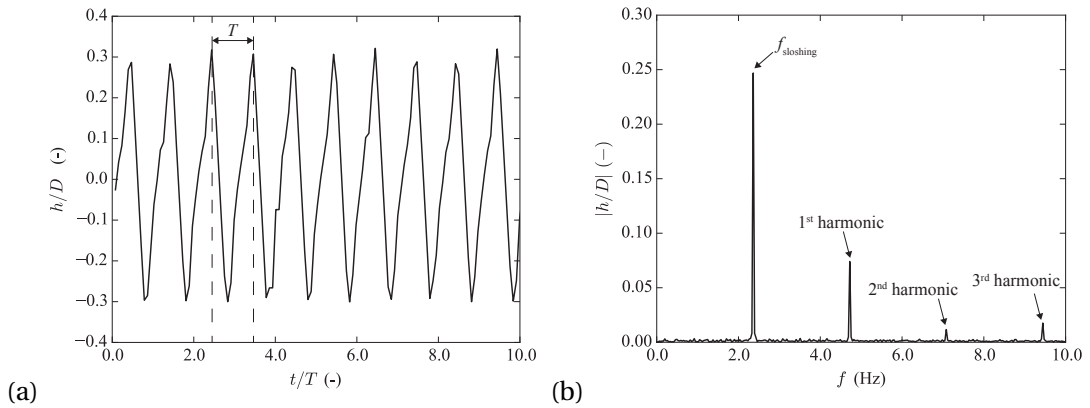


Figure 1.18 – a) Time history of the elevation of the free-surface during the sloshing motion. b) Power spectrum in frequency domain of the sloshing amplitude at  $N = 1100 \text{ min}^{-1}$ ,  $l = 0.1 \text{ m}$  and  $h = 0.15 \text{ m}$

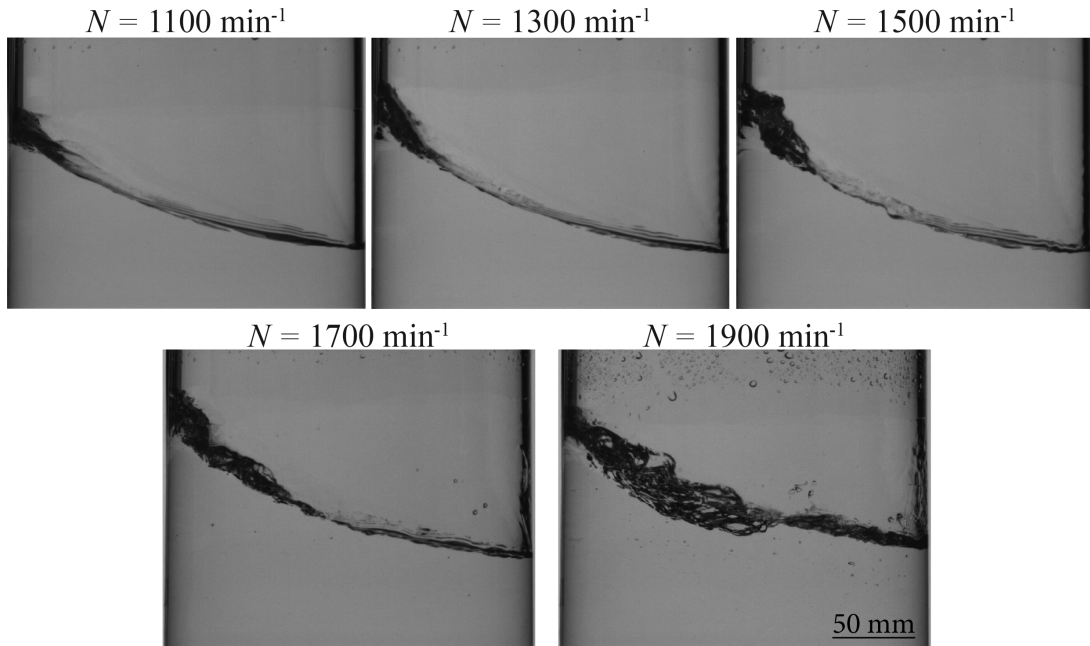


Figure 1.19 – Images of the maximum amplitude of the sloshing motion at the different rotational speed of the fan at  $l = 0.1 \text{ m}$  and  $h = 0.15 \text{ m}$

The natural frequency of the water volume is computed according to eq. (1.13). It varies between  $f_{\text{sloshing}} = 2.1$  for  $l = 0.05 \text{ m}$  and  $f_{\text{sloshing}} = 2.2$  for  $l \geq 0.15 \approx D \text{ m}$  which corresponds to the fulfillment of water depth condition. As observed for the amplitude of the sloshing motion, the bottom wall of the tank noticeably influences the sloshing motion for  $l = 0.05 \text{ m}$  while it is not important for the other water depth. The distance of the water free-surface from the fan does not appear to be influential on the frequency of the sloshing motion.

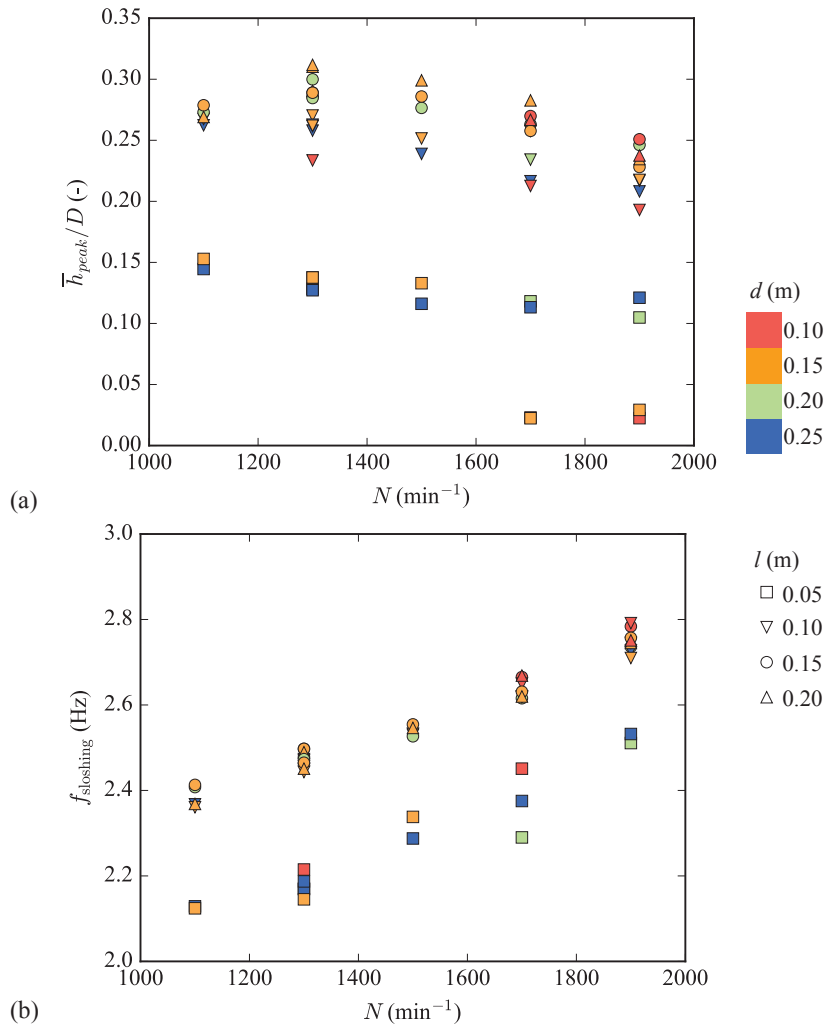


Figure 1.20 – Amplitude (a) and frequency (b) of the sloshing motion as a function of the rotational speed of the fan for all the investigated operating conditions.

#### 1.2.4 Comparison with the sloshing motion of the air-water free-surface in a Francis turbine operating in condenser mode: cause and onset

The behavior of the non-linear sloshing of a water volume excited by a rotating fan placed on top of the free-surface is noticeably similar to the dynamics characteristics of the sloshing motion of the air-water free-surface in the draft tube cone of a Francis turbine operating in condenser mode. The similarity is observed in both frequency and amplitude of the sloshing as a function of the rotational speed and in the mechanism causing wave breaking.

Due to this similarity, the cause of the sloshing motion might be addressed to the shear stresses of air flow on the free-surface generated by the rotating fan/runner causing a rotating base-state flow of the water volume and the further bifurcation to the gravity wave state due to a

## 1.2. Non-linear liquid sloshing in a cylindrical tank forced by a rotating fan

---

potential instability. The experimental investigation conducted in the present work allowed observing that the initially steady free-surface is drag by the tangential shear stresses of the air flow exiting the fan causing a rotation of the free-surface. Then, the development of an instability of the free-surface triggers the free-surface gravity wave at the natural frequency, corresponding to the azimuthal wavenumber  $m = 1$ , plus a small correction depending on the rotational speed of the air-water interface, as observed in Sec.1.1.4.

To further detail and back up this explanation, a study on the water base-state flow and on the velocity profiles of the air flow would be required to fully understand the mechanism of forcing of the air flow on the water surface and to define the condition at the air-water interface causing the onset of the rotating gravity wave.

### 1.2.5 Conclusion

The investigation of the non-linear sloshing of the air-water free-surface in a partially filled tank excited by a rotating fan is performed. Image acquisition and post-processing are applied to measure the amplitude and frequency of the sloshing motion. The influence of the rotational speed of the fan, of the water depth and of the gap between the fan and the free-surface on the amplitude and frequency of the non-linear sloshing are evaluated and a noticeable impact of the rotational speed of the fan is observed on both amplitude and frequency.

The results achieved highlight a similitude of the non-linear sloshing generated by the rotating fan and the sloshing motion observed in the draft tube cone of a Francis turbine operating in condenser mode. This allows identifying the shear stresses of the air flow on the water free-surface as the main phenomenon for understanding the onset of the bifurcation to the gravity wave state, and excluding the possible influence of the fluid-structure interaction due to the vibrations of the draft tube cone.

The present study suggests the need of a further experimental investigation and/or numerical simulation on the velocity profiles of both the air flow and the base-state water flow and on the possible development of an instability to fulfill the theoretical framework describing the onset of the rotating gravity wave.



## 2 Air-water ring

### **Rotating air-water ring in the vaneless gap of a pump-turbine operating in condenser mode**

Reproduced version of:

E. Vagnoni, L. Andolfatto, R. Guillaume, P. Leroy and F. Avellan, (2018), *Rotating air-water ring in the vaneless gap of a pump-turbine operating in condenser mode*, Int. Journal of Multiphase Flow, 105:112-21. DOI:<https://doi.org/10.1016/j.ijmultiphaseflow.2018.03.022>.

with the permission of Elsevier.

#### **The author's contribution:**

The author performed the experiments, the data analysis, and the development of the image processing method. She made the major contribution to analytically develop the diametrical modes of the rotor-stator interaction influenced by the air-water ring. She is the first author of this publication.

#### **Abstract**

The rotating air-water ring, featuring a bubbly flow, in the vaneless gap of a reduced scale physical model of a pump-turbine operating in dewatered condition is investigated. High-speed visualizations are performed together with pressure fluctuation measurements to estimate the bubbles size, the velocity and pressure fields of the two-phase flow as a function of the cooling water discharge and of the gauge pressure in the draft tube cone of the pump-turbine. An image processing method is developed to compute the bubbles size and to estimate both tangential and radial velocity components of the bubbles. The results show that the size of the bubbles in the rotating air-water ring increases by increasing the gauge pressure while the cooling discharge through the labyrinth seals has no influence. The pressure and the velocity fields in both radial and tangential components are estimated as a function of the gauge pressure. Pressure fluctuations and the corresponding frequency are explored and correlated

to the interaction of the rotating air-water ring with the rotating parts and the stationary parts of the pump-turbine. The modal decomposition of the harmonic components of the pressure fluctuation is analytically derived to evidence the rotor-stator interaction in the vaneless gap causing pressure fluctuation.

**Keywords:** Bubbly flow, image processing, velocity profiles, pressure fluctuations, rotor-stator interaction, dewatered hydraulic turbine.

### 2.1 Introduction

Multiphase flows draw increasing attention in the design and the optimization of an engineering system. In particular, gas-liquid two-phase flows play an important role in hydraulic engineering systems. Problems such as cavitation in hydraulic turbomachines, bubbly turbulent flows and air-water interaction phenomena are examples of common two-phase flows which represent a risk for the machine operation, efficiency and safety [20, 64, 108].

Hydraulic turbines and pump-turbines are often required to operate in dewatered condition to minimize the impeller resistant torque and thus the corresponding power losses. One application that requires the dewatered condition is the operation in condenser mode for the grid stabilization [50]. Pressurized air is injected in the draft tube of the machine to maintain the water free-surface level below the impeller. The estimation of the compressed air required by this system is challenging: the operation in dewatered condition by injecting air shows significant air losses yielding power losses.

Several two-phase flow phenomena can be observed in a turbine or pump-turbine operating in dewatered condition. In literature, the sloshing motion of a free-surface, turbulent waves causing the formation and entrainment of bubbles diffusing in the water volume and the formation of droplets interfering with the impeller are described [100]. Another expected phenomenon in dewatered turbine and pump-turbines is the onset of a water ring in the vaneless gap between the impeller and the closed guide vanes due to the interaction of the water discharge coming from the labyrinth cooling system and water droplets which are generated by the oscillation of the air-water interface entrained by the impeller. The water drawn into the impeller is expelled from the outer periphery of the impeller by centrifugal force and it forms a rotating air-water ring in the vaneless gap. The rotating flow interacts with the impeller causing power losses. In addition, it is a suitable place for bubble formations and the mass transfer of air into water.

The two-phase flow and correlated phenomena in the vaneless gap between the impeller and the guide vanes are still not understood and they require further investigations to identify and quantify the flow characteristics causing air losses. To accomplish this goal, the present paper seeks the geometric and dynamic characterization of the rotating air-water ring in the vaneless gap by performing experimental investigations to estimate the bubbles size, the velocity and the pressure fields of the flow as a function of the gauge pressure and the cooling



water discharge.

To successfully investigate two-phase flow phenomena, multiple experimental techniques have been developed and performed. Point intrusive methods can be performed to explore two-phase flow in time domain [46, 90]. Since the intrusive techniques do not provide the spatial information, non-intrusive measurement methods are applied. Thanks to the development of high-speed cameras and optical tools, visualization techniques represent a powerful method to achieve whole-field information in two-phase flows. Example of such non-intrusive experimental techniques are Particle Image Velocimetry (PIV), Laser Doppler Velocimetry (LDV), Particle Tracking Velocimetry (PTV), Magnetic Resonance Velocimetry (MRV) and shadowgraphy [21, 52, 53, 65, 74, 99, 101, 106].

High-speed visualization is widely used for studying two-phase flows. Successful experimental set-up and facility arrangements are essential to achieve undistorted and reliable images. There exist examples of complete optical access through the blades of a turbomachine [109] or the employment of water boxes to mitigate the image distortion [78]. In addition, high-speed visualization is drawing increasing attention due to the advanced image processing which improved in recent years thanks to the development of digital imaging techniques.

Bubbly turbulent flow represents a challenge for a successful image processing, especially in case of a void fraction higher than 15 % and bubbles clusters [41, 45]. For bubbles detection, an image processing method mainly consists in the segmentation of the bubbles in the illuminated liquid film and in the reconstruction of the detected bubbles. When the void fraction increases in bubbly turbulent flows, the image processing method must be able to distinguish deformed bubbles, overlapping bubbles and clusters. Robust image processing methods are described in literature with successful applications on bubble columns [22, 31, 120], micro-channels [55, 82], vapor bubbles [28, 66] and for seabed investigations [103].

In the present paper, the measurement of the size and velocity field of the bubbles of the air-water ring in the vaneless gap between the impeller and the guide vanes of a reduced scale physical model of a pump-turbine are performed by high-speed visualization. Image processing is applied for the bubble detection and tracking position in the rotating air-water ring in the vaneless gap to measure the velocity field. Pressure fluctuation measurements, spectral analysis and modal decomposition of the harmonic components are performed to investigate the pressure field and to evidence the rotor-stator interaction.

The experimental set-up is described in Sec. 2.2 and the image processing method developed and performed to estimate the velocity field of the bubbly flow is illustrated in Sec. 2.3. The results are presented and discussed in Sec. 2.4.

## 2.2 Experimental set-up

### 2.2.1 Facility

The experiments are performed on a 1:14 reduced scale physical model of a high head reversible pump-turbine with a specific speed coefficient  $n_{QE} = 0.078$  defined as follows:

$$n_{QE} = n \times \frac{Q^{1/2}}{E^{3/4}} \quad (2.1)$$

where  $n$  is the rotating frequency of the impeller ( $\text{s}^{-1}$ ),  $Q$  the discharge and  $E$  the machine specific energy.

A sketch of the main components of the model is illustrated in Fig. 2.1. The model includes the spiral case, 20 guide vanes, 9 blades impeller and the draft tube. As illustrated in Fig. 2.2, the vaneless gap between the impeller and the guide vanes has a ring shape and it measures  $0.06 \times D_e$  in height  $h_{\text{gap}}$  and  $0.09 \times D_e$  in maximum width  $w$  - to be used to make non dimensional the diameter of the bubbles - where  $D_e = 0.304$  m is the high pressure diameter of the impeller. A generator connected to the impeller regulates the rotational speed. The test rig is operated in closed loop configuration and is equipped with an axial pump which generates the specific hydraulic energy. To operate in condenser mode, the guide vanes are closed and a system of air injection is installed in the draft tube cone. Water is injected through the labyrinth seals for cooling purpose.

The Froude similarity is fulfilled by defining the densimetric Froude number as follows in eq. (2.2).

$$Fr_d = \sqrt{\frac{\rho_{\text{air}}}{\rho_{\text{water}}} \frac{\omega \sqrt{D_e}}{\sqrt{g}}} \quad (2.2)$$

$\omega$  is the angular velocity of the impeller ( $\text{rad}\cdot\text{s}^{-1}$ ),  $\rho_{\text{air}}$  and  $\rho_{\text{water}}$  are the air and water density, respectively. The air density is computed from the ideal gas law by measuring the static air pressure in the cone of the draft tube and the temperature. This similarity law has been introduced by Tanaka et al. [100] in the investigation of the sloshing motion of the free-surface in the draft tube cone of a pump-turbine operating in synchronous condenser mode.

### 2.2.2 Instrumentation

The visualization of the water ring in the vaneless gap between the guide vanes and the impeller is performed through two flat optical windows to allow the illumination and the optical access of the vaneless gap and guide vanes as illustrated in Fig. 2.1. The air-water

## 2.2. Experimental set-up

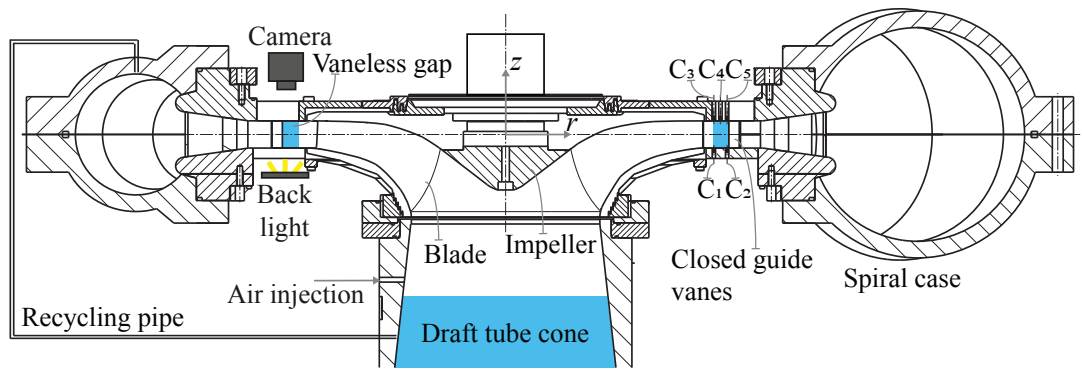


Figure 2.1 – Test-rig layout with the instrumentation.

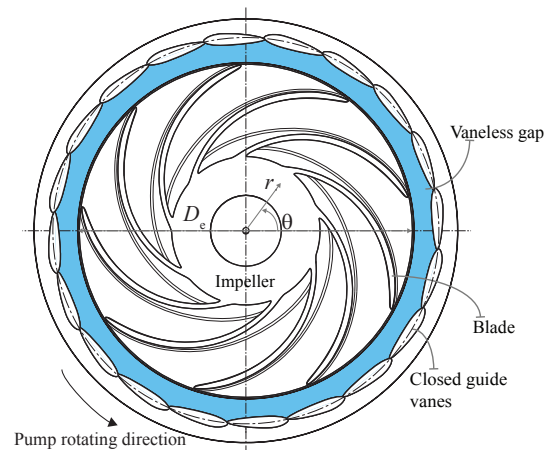


Figure 2.2 – Top view of the 9 bladed impeller and the 20 guide vanes of the pump-turbine model.

ring visualization is performed with high-speed camera (Photron FASTCAM MC2.1), at image acquisition rates of 4'000 frames per second for 8 s, and resolution of 512 pixels  $\times$  256 pixels. A 95 % uniform LED screen (PHLOX LEDW-BL-150/40-LLUB-Q-1R24) of 150 mm  $\times$  40 mm size and 35'000  $\text{cd}\cdot\text{m}^{-2}$  luminance is installed as a back light to enhance the contrast between gaseous and liquid phases.

Dynamic wall pressure measurements are performed in five locations in the vaneless gap between the impeller blades and the closed guide vanes by using flush-mounted piezo-resistive pressure sensors (UNISENSOR HF900-03291.500). They allow for pressure measurements in the range of 0-20 bar with a maximum measurement uncertainty of 0.7 %. The position of the sensors is illustrated in Fig. 2.1 and summarized in Tab. 2.1. The sample frequency is set at 1'200 Hz and 5 s of measurements are recorded.

The camera triggers the pressure acquisition system to start simultaneously both photography and pressure measurements.

Table 2.1 – Pressure sensors position in the vaneless gap.

Sensor	$r/R_e$ (-)	$z/D_e$ (-)	$\theta$ (°)
C1	1.06	-0.03	0
C2	1.12	-0.03	36
C3	1.06	0.03	0
C4	1.09	0.03	18
C5	1.12	0.03	36

### 2.2.3 Investigated operating points

The operating points at which the reduced scale physical model of a pump-turbine operates during the performed tests are given in Fig. 2.3. Five gauge pressure  $p$  conditions measured in the cone of the draft tube in air are investigated at  $Fr_d = 0.5$ . For each  $p$  value, four cooling discharge conditions are studied:  $Q = 20 \text{ l}\cdot\text{h}^{-1}$ ,  $Q = 40 \text{ l}\cdot\text{h}^{-1}$ ,  $Q = 60 \text{ l}\cdot\text{h}^{-1}$  and  $Q = 80 \text{ l}\cdot\text{h}^{-1}$ . The machine operates in pump rotating direction for all the investigated operating points. An electronic controller sets the rotational speed  $N$  ( $\text{min}^{-1}$ ) of the impeller, a manometer regulates the gauge pressure in the cone of the draft tube and a valve coupled with an electromagnetic flowmeter controls the cooling discharge.

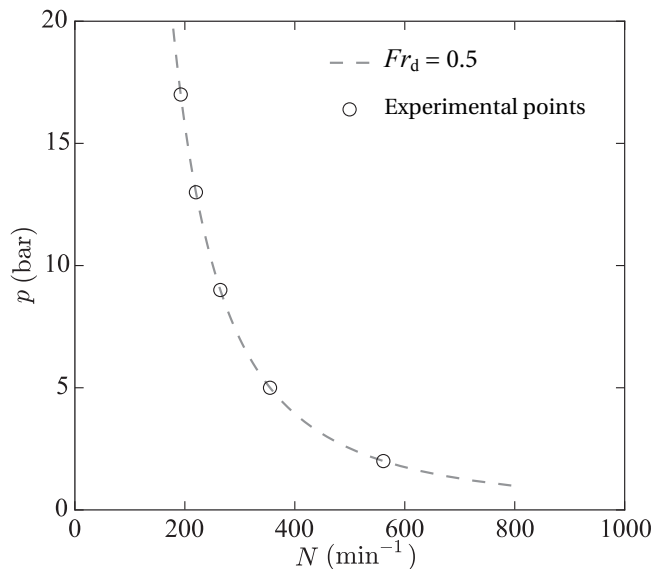


Figure 2.3 – Investigated operating points on the iso-Froude curve at  $Fr_d = 0.5$  as a function of the rotational speed  $N$  and the gauge pressure  $p$ .

## 2.3 Method

### 2.3.1 Image processing

An image processing method is developed to determine the bubble size and velocity profiles by detecting and tracking the bubbles in the recorded images, as summarized in the flow chart given in Fig. 2.4. This method is a particle tracking based technique implemented in Python by using the open source library *scikit-image* for bubbles labeling [114] and *trackpy* for tracking the detected bubbles [9]. One application of these algorithms can be found in the work of Sauret et al. [94].

As a first step, the images are trimmed to select the region of interest and each pixel of the image is identified by polar coordinates which corresponds to the polar coordinates system presented in Fig. 2.2 and illustrated in Fig. 2.5 as well.

In a second step, the Otsu filter [48] is applied to identify the edge of the bubbles in contrast with the bright background, as shown in Fig. 2.6 (a). The patterns of interest are the single bubbles represented by the small black areas surrounded by white liquid film. The black areas at the bottom and top of the window correspond to the casing of the machine and they should not be considered as a pattern. Bubbles clusters which cannot be individually distinguished also are discarded since their behavior is stochastic and not representative of the dynamic characteristics of the air-water ring. While it is troublesome to estimate the number of discarded bubbles in clusters in the recorded images, it is possible to estimate that the discarded clusters represent about 5 % of the total number of black areas for  $p < 13$  bar and about 15 % for higher pressure conditions. Since the size of one bubble is clearly different on the top and on the bottom black areas and on the clustering of many bubbles, only the features with a perimeter smaller than a fixed value are selected, as illustrated in Fig. 2.6 (b). In a first stage, the perimeter size is chosen based on the distribution of the perimeters of the black areas. This means by computing the range of perimeters which corresponds to the size of single bubbles. Then, by running the algorithm and looking at the selected bubbles and/or clusters in few images, the values are precisely tuned. The lower bound is fixed to avoid that the algorithm erroneously considers as a bubble any black area of one or two pixels which correspond to noise in the image. The upper bound allows discarding clusters without discarding single bubbles. It is important to select the good range of values because single bubbles better follow the flow than clusters, indeed different ranges of values would decrease the accuracy of the velocity measurements. On the other side, clusters of few tiny bubbles can be considered as a single feature by the image processing method.

In the previous step, each feature is determined by the perimeter, major and minor axis, and the position on the image by using the open source library *skimage.measure.regionprops* [114]. The bubbles are assumed to be oblate spheroid with minor semi-axis  $a$  and major semi-axis  $b$ . This hypothesis has been validated in literature as for instance the work of Colombet et al.

[31]. For each bubble the equivalent diameter is estimated as follows:

$$d_{\text{eq}} = (8b^2 a)^{1/3} \quad (2.3)$$

In the next step, the method links the successive positions of each feature in the following images. The trajectories of the bubbles are identified and the velocity vectors are computed for each bubble as shown in Fig. 2.6 (c).

To compute the radial and angular velocity profiles of both velocity components, the velocities of the bubbles are averaged depending on the bubble position. For computing the radial profile, five radial sections are identified in the image and the velocities of the bubbles - whose position belongs to the same section - are averaged. The same procedure is applied to compute the angular distribution of the velocity components by dividing the investigated window in 160 sections, 40 radial and 40 angular, respectively.

### 2.3.2 Pressure fluctuations and spectral analysis

The time history of the pressure measurement at the location C1 is illustrated in Fig. 2.7(a). A study on the pressure fluctuations measurements is performed by spectral analysis to investigate the amplitude and frequency of the pressure oscillation. As illustrate in Fig. 2.7(b), the auto-spectrum  $G_{xx}$  of the pressure signal at the location C1 makes apparent the resonance frequency  $f_0$  of the pressure oscillation at  $p = 5 \text{ bar}$  and  $Q = 60 \text{ l}\cdot\text{h}^{-1}$ . Moreover, a cross-spectral analysis between the pressure measurements is performed to evaluate the correlation of the pressure measurements at different locations and to assure the homogeneity of the response in frequency domain of the pressure at the different locations in the vaneless gap. Examples of the performed cross-spectral analysis are illustrated in Fig. 2.8 for the pressure measurements at location C1 and C3. It includes the computation of the amplitude of the cross-spectral density function  $G_{xy}$  and the coherence in the frequency domain of the two signals.

## 2.4 Results and discussion

### 2.4.1 Size of the bubbles

The high-speed visualization enables the observation of the air-water ring in the vaneless gap between the impeller and the guide vanes of a pump-turbine. Images of the air-water ring at the four cooling discharge conditions are presented in Fig. 2.9. The flow in the air-water ring is characterized by a rotating bubbly flow whose bubbles increase in size by increasing the gauge pressure in the cone of the draft tube. It is observed that the cooling discharge through the labyrinth seals has no influence on the bubbles size. Images of the air-water ring at the five gauge pressure conditions are presented in Fig. 2.10.

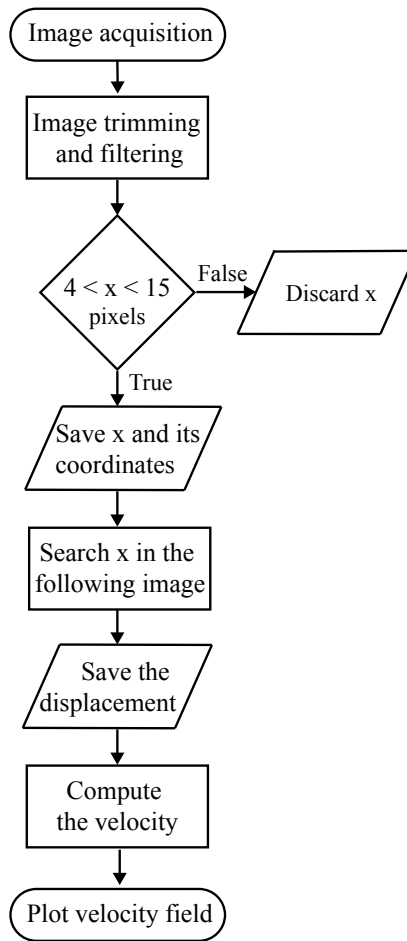


Figure 2.4 – Flow chart of the image processing method for tracking bubbles at  $p = 2$  bar.  $x$  represents the perimeter of the black area of interest in the image to feature bubbles.

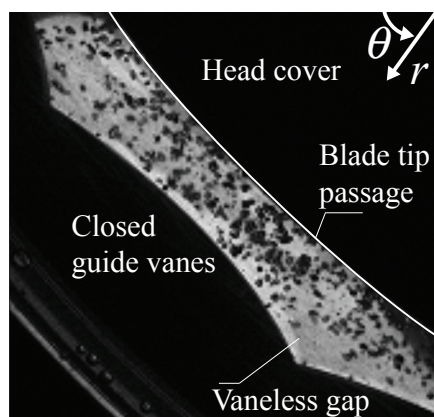


Figure 2.5 – Sample image.

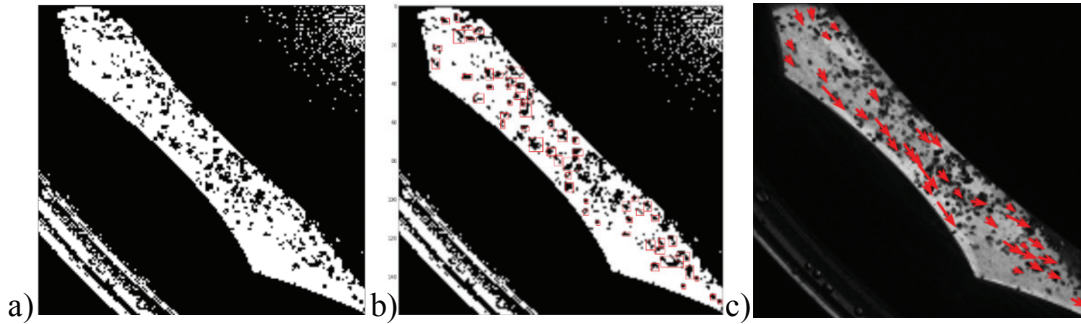


Figure 2.6 – Steps of the image processing method to measure the velocity of the bubbles in the air-water ring.

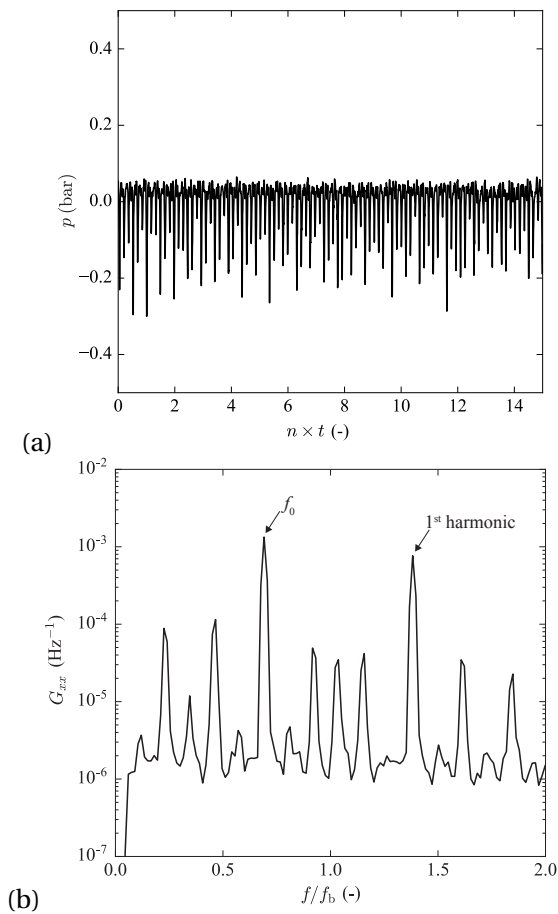


Figure 2.7 – Time history (a) and auto-spectrum (b) of the pressure measurements at the location C1 at  $p = 5 \text{ bar}$  and  $Q = 60 \text{ l}\cdot\text{h}^{-1}$ .

The mean equivalent diameter of the bubbles, non-dimensionalized as defined in eq. (2.4), is presented in Fig. 2.11 as a function of the gauge pressure. The boxes extend from the lower to upper quartile values of the data, with a line at the median and a point at the mean value.



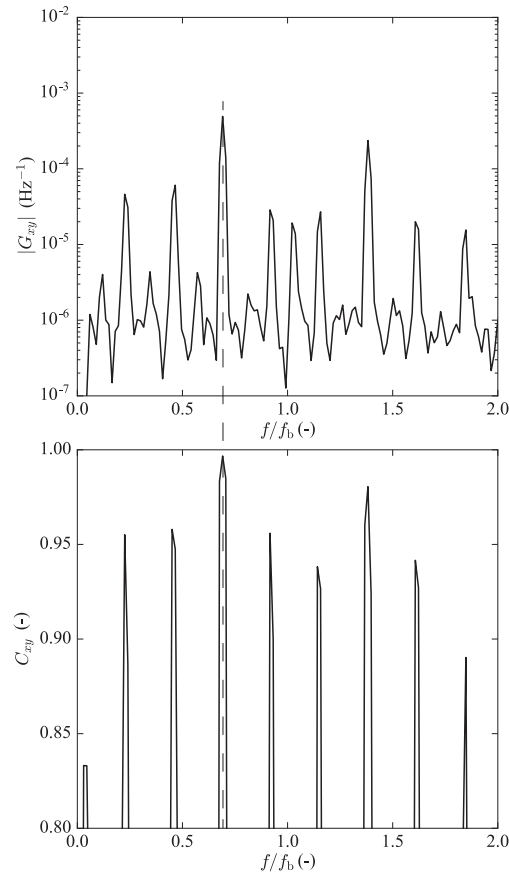


Figure 2.8 – Cross-spectral analysis between the pressure measurements at the locations C1 and C3 at  $p = 5$  bar and  $Q = 60 \text{ l}\cdot\text{h}^{-1}$ . Cross-spectrum amplitude in logarithmic scale (top) and coherence (bottom).

The whiskers extend from the box to the maximum and minimum value to show the range of the data. It is observed that the boxes and the whiskers extension increases by increasing the gauge pressure. The mean size of the bubbles increases by increasing the gauge pressure and as a consequence, there are more bubbles of different sizes which explains the distribution of the data on a wider range of values.

$$d_{\text{eq}}^* = \frac{d_{\text{eq}}}{w} \quad (2.4)$$

### 2.4.2 Influence of the cooling discharge on the velocity profiles

The velocity profiles of both tangential and radial components divided by the peripheral velocity of the blade tip  $U_{\text{tip}}$  at  $p = 5$  bar for the four cooling discharge conditions are illustrated

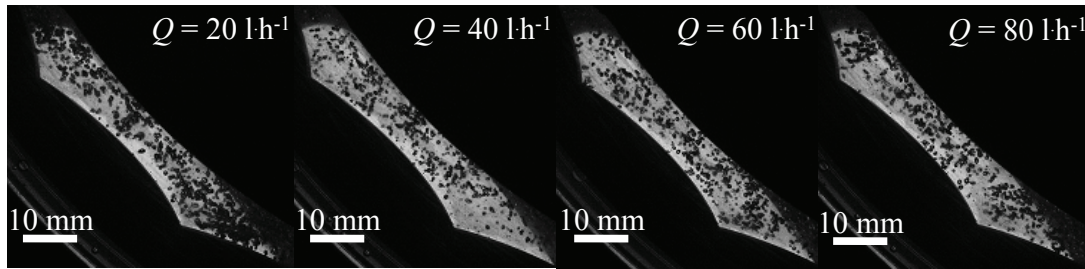


Figure 2.9 – Images of the air-water ring in the vaneless gap at  $p = 5$  bar for the four cooling discharge conditions.

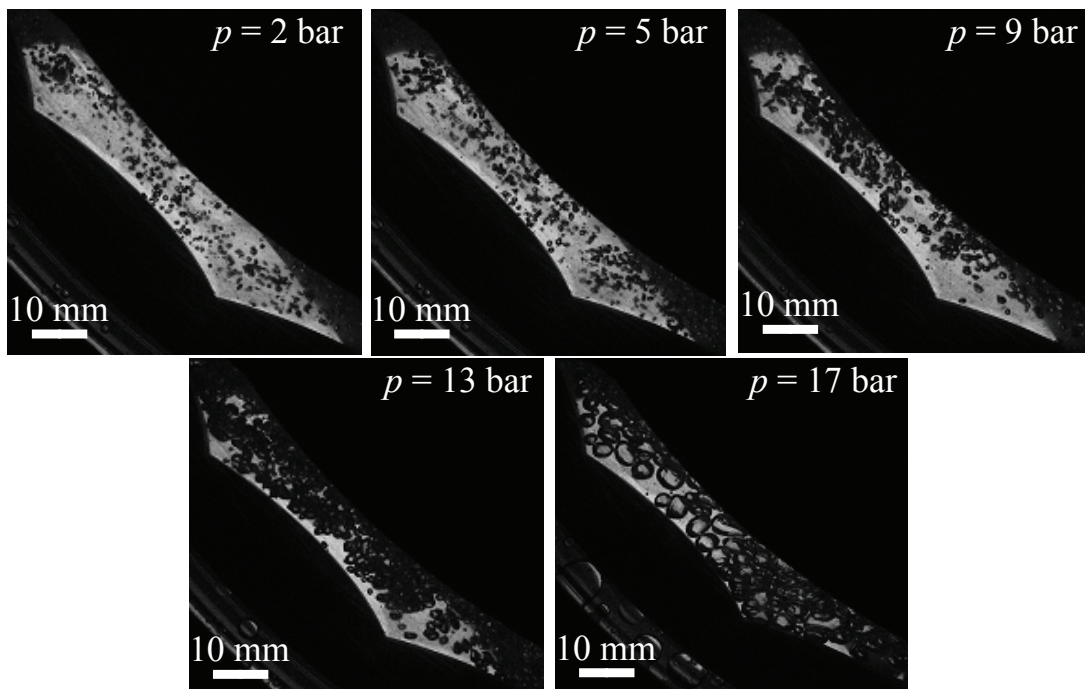


Figure 2.10 – Images of the air-water ring in the vaneless gap at  $Q = 60 \text{ l}\cdot\text{h}^{-1}$  for the five investigated gauge pressure conditions.

in Fig. 2.12. The velocity of the bubbles in the air-water ring is mainly tangential: the radial velocity component is small in comparison to the tangential component. No difference is recorded by changing the cooling discharge with a maximum standard deviation equal to 0.21 on the non-dimensional tangential velocity.

### 2.4.3 Influence of the gauge pressures on the velocity profiles

The velocity profiles of both tangential and radial components are illustrated in Fig. 2.13. As previously observed, the bubbles velocity is mainly tangential and is slower than the tip of the blades. An influence of the gauge pressure on the tangential velocity divided by the peripheral

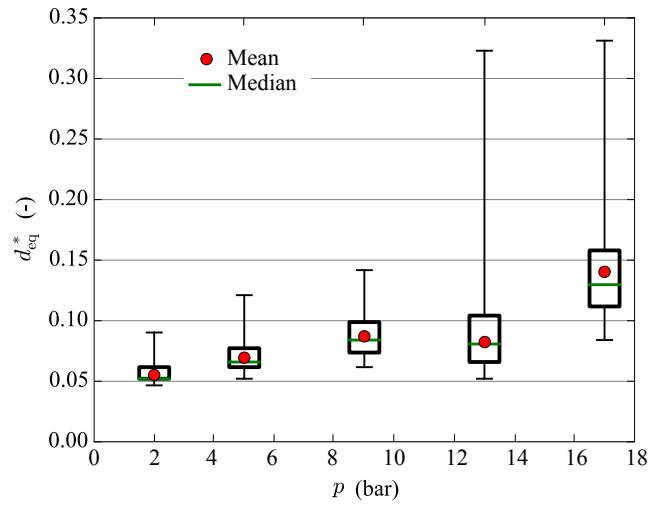


Figure 2.11 – Equivalent diameter distribution statistics as a function of the gauge pressure at  $Q = 60 \text{ l}\cdot\text{h}^{-1}$ .

velocity of the blade tip is noticed. The tangential velocity of the flow at  $p = 17$  bar is lower than the one recorded at the other pressure conditions. This can be explained by the larger size of the bubbles: the formation of clusters of bubbles is observed and they slow down the flow velocity. At  $p = 13$  bar a lower number of bubbles could be tracked due to the higher void fraction. The bubbles at the radius closer to the tip could not be distinguished by the image processing method. Moreover, this introduces a higher standard deviation on both tangential and radial velocity components.

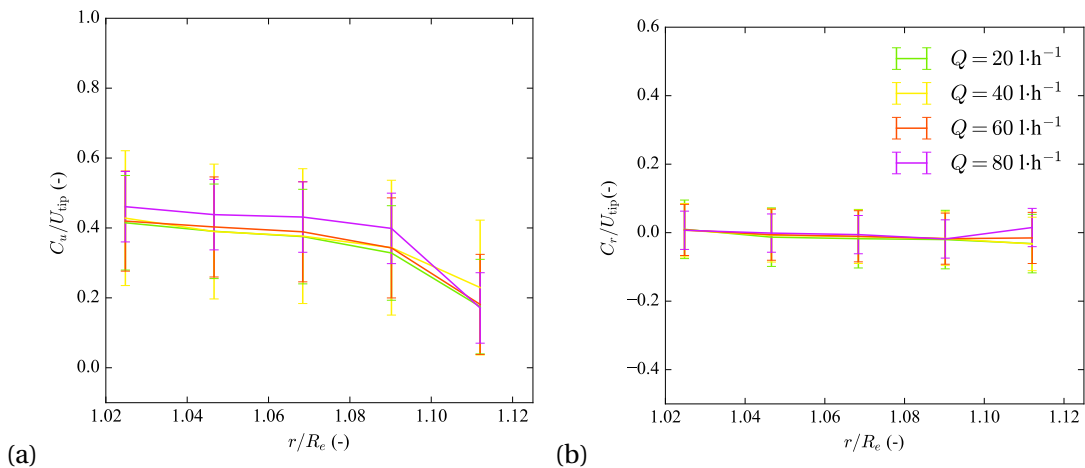


Figure 2.12 – Velocity profile of tangential (a) and radial (b) velocity at  $p = 5$  bar.

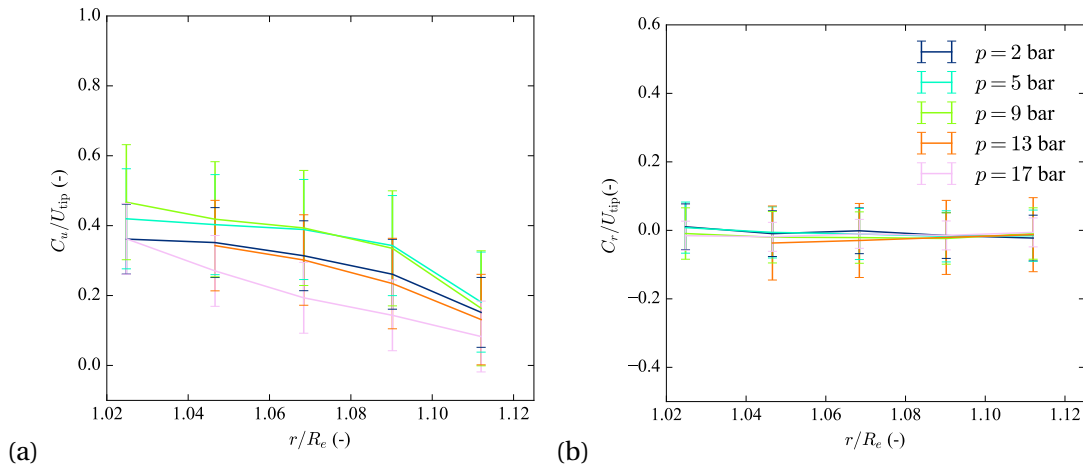


Figure 2.13 – Velocity profile of tangential (a) and radial (b) velocity at  $Q = 60 \text{ l}\cdot\text{h}^{-1}$ .

#### 2.4.4 Angular distribution of the radial and tangential velocity components of bubbles in the air-water ring

The angular distributions of the tangential and radial velocity components of the bubbles of the air-water ring are presented in Fig. 2.14 and Fig. 2.15, respectively at  $Q = 60 \text{ l}\cdot\text{h}^{-1}$  and  $p = 5 \text{ bar}$ .

It is observed that the bubbles follow the geometrical shape of the guide vanes by causing a fluctuation of the flow velocity in the vaneless gap which can justify the value of the standard deviation of both velocity components profiles observed in Sec. 2.4.3. In particular, it is observed that the tangential velocity decreases in correspondence of the enlargements of the vaneless gap due to the guide vanes shape. The radial velocity component increases in amplitude in negative direction following the cross-section narrowing of the vaneless gap due to the guide vanes shape and it increases in positive direction in the corresponding enlargement.

#### 2.4.5 Pressure field in the vaneless gap

The frequency corresponding to the spectrum peak of the pressure measurements and divided by the blade passing frequency  $f_b$  is illustrated in Fig. 2.16 (a) and (b) as a function of the cooling discharge at  $p = 9 \text{ bar}$  and of the gauge pressure at  $Q = 60 \text{ l}\cdot\text{h}^{-1}$ , respectively. The frequency ratio keeps constant by varying the cooling discharge and the gauge pressure. The pressure fluctuations measured by all the sensors exhibit significant amplitudes at a frequency  $f/f_b = 0.7$ , except for the one at the location C5 which experiences significant amplitudes at a frequency  $f/f_b = 1.4$ . The frequency values of the pressure fluctuations are proportional to the blades frequency, but they do not occur at the blade passing frequency or at a multiple. These oscillations are possibly produced by the interaction of the rotating parts (air-water ring and blades) and the stationary parts of the machine (guide vanes), as it will be discussed in

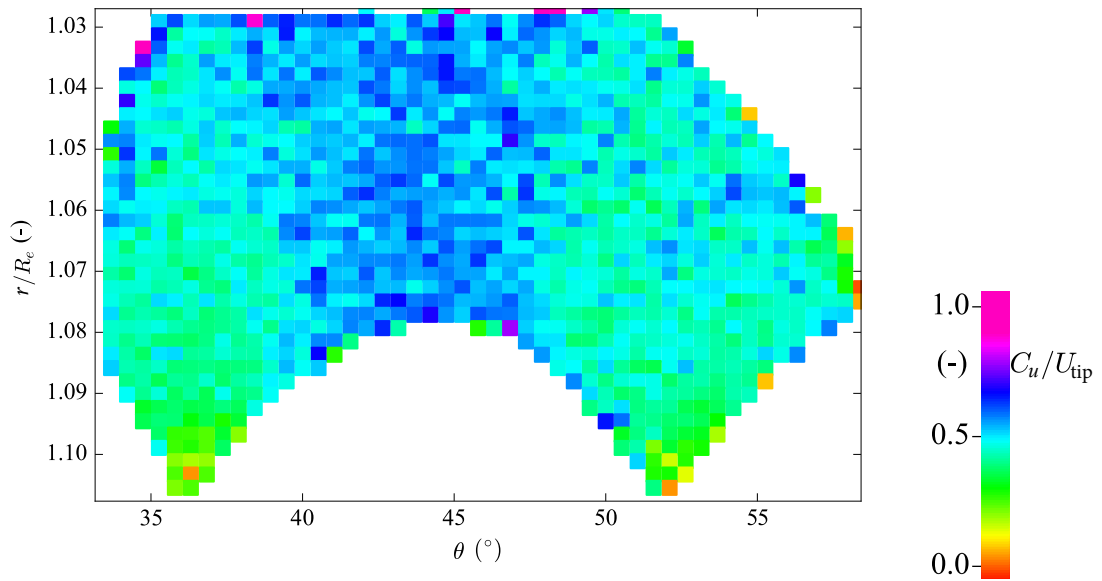


Figure 2.14 – Angular distribution of the tangential velocity component of the bubbles in the air-water ring at  $Q = 60 \text{ l}\cdot\text{h}^{-1}$  and  $p = 5 \text{ bar}$ .

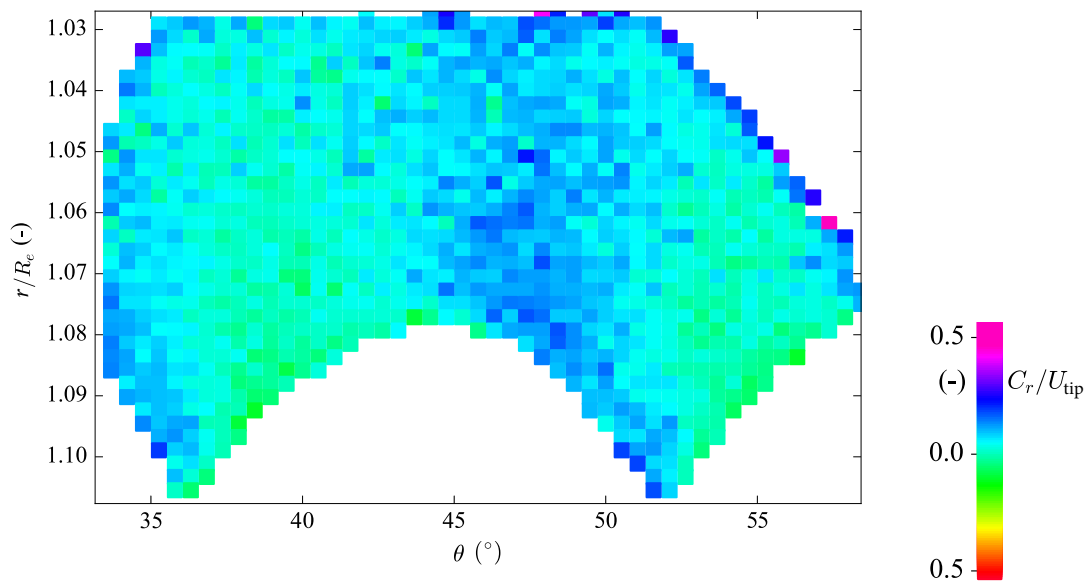


Figure 2.15 – Angular distribution of the radial velocity component of the bubbles in the air-water ring at  $Q = 60 \text{ l}\cdot\text{h}^{-1}$  and  $p = 5 \text{ bar}$ .

Sec. 2.4.6.

The influence of the cooling discharge on the amplitude  $G_{xx}(f_0)$  evaluated in the five locations C1, C2, C3, C4 and C5 is presented in Fig. 2.16 (c) at  $p = 9 \text{ bar}$ . The cooling discharge does not significantly influence the amplitude of the hydro-acoustic response of the system. The

## Chapter 2. Air-water ring

evolution of the amplitude  $G_{xx}(f_0)$  with the gauge pressure is presented in Fig. 2.16 (d) at  $Q = 60 \text{ l}\cdot\text{h}^{-1}$ . A lower amplitude is observed at  $p = 2 \text{ bar}$  with respect to the other pressure conditions. Moreover, it is observed that the amplitude evaluated at the bottom wall and close to the blade tip, location C1, is higher than at the guide vanes wall, location C2, while at the top wall there are no significant differences in amplitude between the three measurement locations C3, C4 and C5. This variation of amplitude related to the measurement location is likely due the shape of the rotating air-water ring which could not fill the entire vaneless gap and indeed the locations C1 and C2 are in water while the others in air.

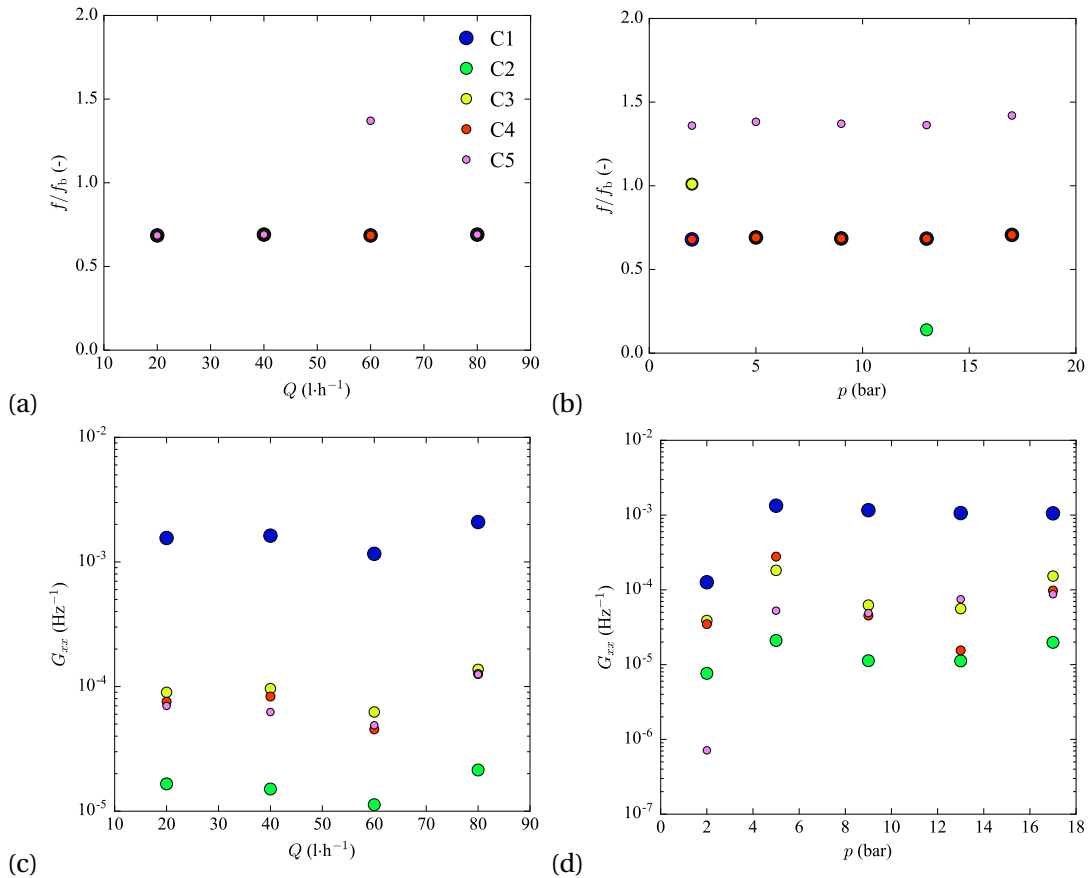


Figure 2.16 – Frequency corresponding to the spectrum peak of the pressure fluctuation normalized to the frequency of the blades passage  $f_b$  as a function of the cooling discharge at  $p = 9 \text{ bar}$  (a) and as a function of the gauge pressure at  $Q = 60 \text{ l}\cdot\text{h}^{-1}$  (b). Auto-spectrum of the pressure measurements as a function of the cooling discharge at  $p = 9 \text{ bar}$  (c) and as a function of the gauge pressure at  $Q = 60 \text{ l}\cdot\text{h}^{-1}$  (d).

### 2.4.6 Evidence of the rotor-stator interaction

Flow perturbations in the vaneless gap are caused by the interaction of the impeller blades and the guide vanes. This rotor-stator interaction (RSI) induces pressure waves propagating

in the hydraulic machine as diametrical pressure mode rotating in the vaneless gap between the guide vane and the impeller blades. Previous studies investigated the development of these pressure waves in a reversible pump-turbine during the operation in pump or turbine mode [17, 93]. Zobeiri [124] developed a RSI model in a reversible pump-turbine operating in generating mode and explained the propagation of pressure fluctuations due to the RSI as the result of the interaction between two non-uniform velocity-pressure fields, one coming from the guide vanes and the other from non-uniform pressure field at the impeller inlet. These stationary and rotating periodic flows are expressed as a Fourier series and the resulting pressure field can be analytically described as a product of the guide vanes and the impeller blades pressure fields.

In the case of a reversible pump-turbine operating in synchronous condenser mode, it is necessary to consider also the harmonic components related to the rotating air-water ring. Indeed, the combination of the guide vanes, impeller blades and air-water ring pressure fields is evaluated to investigate the resulting modes of the RSI which could justify the measured pressure fluctuations at  $f/f_b = 0.7$  and its harmonics in the vaneless gap. These periodic pressure fields can be expressed as a Fourier series:

$$p_s(\theta_s, t) = \sum_{n=0}^{\infty} A_n \cdot \cos(nz_o\theta_s + \varphi_n) \quad (2.5)$$

$$p_r(\theta_r, t) = \sum_{m=0}^{\infty} A_m \cdot \cos(mz_b\theta_r + \varphi_m) \quad (2.6)$$

$$p_{wr}(\theta_r^*, t) = \sum_{l=0}^{\infty} A_l \cdot \cos(l\theta_r^* + \varphi_l) \quad (2.7)$$

Where  $m$ ,  $n$  and  $l$  are the harmonic orders,  $A_m$ ,  $\varphi_m$  being respectively the amplitude and the phase for the  $m^{\text{th}}$  harmonic,  $\theta_s$ ,  $\theta_r$ ,  $\theta_r^*$  being the angle coordinates in the stationary, rotating systems and in the air-water ring, respectively,  $z_b$  is the impeller blade number and  $z_o$  is the guide vanes number. The resulting pressure fields can be expressed as follows:

$$p = \left[ \sum_{n=0}^{\infty} A_n \cdot \cos(nz_o\theta_s + \varphi_n) \right] \cdot \left[ \sum_{m=0}^{\infty} A_m \cdot \cos(mz_b\theta_r + \varphi_m) \right] \cdot \left[ \sum_{l=0}^{\infty} A_l \cdot \cos(l\theta_r^* + \varphi_l) \right] \quad (2.8)$$

According to the impeller angle coordinate expression for the stationary reference frame,  $\theta_r$ ,  $\theta_r^*$  are defined as  $\theta_r = \theta_s - \omega t$  and  $\theta_r^* = \theta_s - c \cdot \omega t$ .  $c$  is a reduction coefficient  $0 < c < 1$  due to the rotational speed of the bubbly flow of the air-water ring which is lower than the one of the blade tip as shown in Fig. 2.13. This modulation for one harmonic yields the following

resulting pressure field:

$$\begin{aligned}
 p_{mnl}(t, \theta_s) = & \frac{A_{k_1}}{4} \cos((mz_b + cl)\omega t - k_1\theta_s + \varphi_n + \varphi_m + \varphi_l) + \\
 & + \frac{A_{k_2}}{4} \cos((mz_b - cl)\omega t - k_2\theta_s + \varphi_n + \varphi_m + \varphi_l) + \\
 & + \frac{A_{k_3}}{4} \cos((mz_b + cl)\omega t - k_3\theta_s + \varphi_n + \varphi_m + \varphi_l) + \\
 & + \frac{A_{k_4}}{4} \cos((mz_b - cl)\omega t - k_4\theta_s + \varphi_n + \varphi_m + \varphi_l)
 \end{aligned} \tag{2.9}$$

where  $k_1 = mz_b + nz_o + l$ ,  $k_2 = mz_b + nz_o - l$ ,  $k_3 = mz_b - nz_o + l$  and  $k_4 = mz_b - nz_o - l$  are the contributions of the diametrical pressure modes and they indicate the rotating direction of diametrical mode: positive  $k$  values correspond to a rotational mode in the same direction than the impeller.

Fig. 2.17 represents all the main frequencies correlated with RSI influenced by the rotating air-water ring. The frequencies of pressure fluctuations related to the blade passing frequency,  $f/f_b = 1$  and the frequency corresponding to the diametrical mode with the highest energy,  $f/f_b = 0.7$  are detected. This diametrical mode corresponds to the harmonics orders  $m = n = 1$  and  $l = 10$ , which diverges from the diametrical modes highlighted in literature for the generating mode of a pump-turbine [124]. The variance with the generating mode over the diametrical modes is due to the presence of the air-water ring, when operating in condenser mode, which adds a further pressure fields interacting with the one coming from the impeller blades and the one of the closed guide vanes. Therefore, this analysis evidences that the pressure fluctuations observed in the experimental results presented in Sec. 2.4.5 are the outcome to the modulations of rotor-stator interactions which occur at  $f/f_b = 0.7$ .

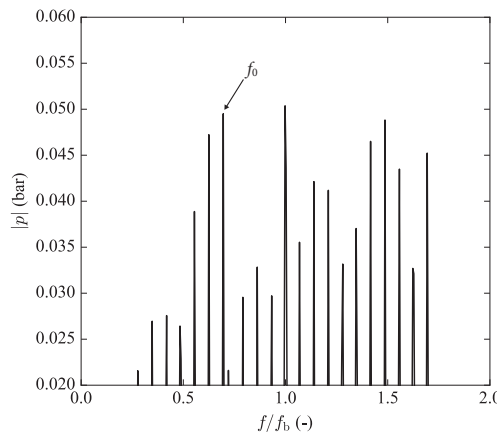


Figure 2.17 – Spectral analysis of the instantaneous pressure in the vaneless gap at a radius  $r/R_e = 1.06$  and  $p = 5$  bar.



### 2.5 Conclusion

In the present work, the bubbles size, velocity and pressure field in the air-water ring in the vaneless gap between the guide vanes and the impeller of a pump-turbine operating in dewatered condition are investigated.

High-speed visualization and pressure fluctuation measurements are performed. The size and the radial and tangential velocity profiles of the bubbles in the air-water ring are estimated by developing an image processing method. The size of the bubbles depends on the gauge pressure: the higher the pressure, the larger is the equivalent diameter of the bubbles. The gauge pressure has also an influence on the bubbles velocity in the air-water ring. At  $p = 17$  bar the size of the bubbles causes the formation of clusters which slow down the motion of the flow. The measured velocity profiles showed that the flow is mainly tangential in the radial section of the vaneless gap. The variation of the tangential and radial component is observed by computing the angular distribution of the velocity components in the radial section. The bubbles in the air-water ring follow the geometrical shape of the guide vanes wall and it causes the fluctuation of both velocity component.

Pressure measurements showed a pressure fluctuation in the vaneless gap between the guide vanes and the impeller characterized by a frequency which is lower than the blade passing frequency. The ratio  $f/f_b = 0.7$  is constant for all the investigated operating points. It is analytically demonstrated that this pressure fluctuations are caused by the interaction of the rotating air-water ring with the rotating and stationary component of the machine.

In light of the presented results, the dynamic characteristics of the rotating air-water ring in the vaneless gap are illustrated and they can be useful for understanding the air losses in a pump-turbine operated in dewatered condition. In a further study, we envisage to estimate the parameters of the mass transfer of air in water to compute the air losses through the vaneless gap. A numerical simulation of the flow in the vaneless gap can be useful to further investigate the RSI influenced by the rotating air-water ring.



## 3 Torque stability

### **Interaction of a rotating two-phase flow with the torque stability of a reversible pump-turbine operating in condenser mode**

Reproduced version of:

E. Vagnoni, L. Andolfatto, R. Guillaume, P. Leroy and F. Avellan, *Interaction of a rotating two-phase flows with the torque stability of a reversible pump-turbine operating in condenser mode*, submitted to International Journal of Multiphase Flow (2018).

with the permission of Elsevier.

#### **The author's contribution:**

The author performed the experiments and the data analysis. She implemented the surrogate model to predict the differential pressure coefficient. She is the first author of this publication.

#### **Abstract**

The operation of a reversible pump-turbine in condenser mode requires to dewater the impeller by closing the guide vanes and injecting compressed air in the draft tube cone to reduce the friction torque on the impeller blades. A water discharge is injected through the labyrinth seals for cooling purpose. The interaction of the water cooling discharge and the blades of the impeller causes the formation of an air-water ring in the vaneless gap between the impeller blades and the closed guide vanes. Depending on the operating conditions, the hydrodynamic characteristics of the air-water ring in the vaneless gap change and affect the stability of the pressure in the machine and of the resisting mechanical torque transmitted through the coupling of the impeller and the shaft. This research aims to experimentally elucidate the hydrodynamic properties of the air-water ring as a function of the operating condition and to investigate the influence of this flow on the stability of both pressure and torque. High-speed visualizations are performed together with pressure fluctuations and torque measurements to establish a correlation between the flow characteristics and the

pressure and torque swings. A cross-spectral analysis between the signals is performed as well as phase averaging to investigate the periodicity of the recorded instability. Based on the results achieved in this analysis, a multivariate adaptive regression spline surrogate model of the pressure coefficient at stable condition is built as a function of the relevant operating parameters.

**Keywords:** Two-phase flow instability, torque fluctuation, densimetric Froude number, high-speed visualization, MARS surrogate model, dewatered hydraulic turbine.

### 3.1 Introduction

Hydraulic turbines and pump-turbines can operate in condenser mode to provide or absorb reactive power for grid regulation [50]. The impeller is dewatered to minimize the resisting mechanical torque and so the corresponding power losses. Compressed air is injected in the draft tube of the machine to maintain the water free-surface level below the impeller and a cooling discharge is injected through the labyrinth seals. The mixing of the water cooling discharge with the pressurized air causes the formation of two-phase flow phenomena which can interact with the impeller and increase the resisting torque. Moreover, two-phase flow phenomena increase the air consumption due to the mixing of air into the water volume and make challenging the design of the air supply system.

Previous studies evidence the formation of many two-phase flow phenomena in a turbine or pump-turbine operating in condenser mode. These include the observation of a sloshing motion of a free-surface [100, 110], turbulent waves causing the formation and entrainment of bubbles diffusing in the water volume and the formation of droplets interfering with the impeller [100]. Another observed phenomenon in dewatered turbine and pump-turbines is the formation of an air-water ring in the vaneless gap between the impeller blades and the closed guide vanes. Tanaka et al. [100] mentioned this phenomenon by observing tiny water droplets, coming from the oscillation of the air-water free-surface in the draft tube cone and sucked into the impeller. Vagnoni et al. [111] observed the formation of the air-water ring characterized by a rotating bubbly flow and investigated both velocity and pressure fields. Due to the centrifugal force given to the cooling discharge by the rotating impeller and to the mixing of the flow with the compressed air, an air-water ring forms in the vaneless gap between the closed guide vanes and the impeller blades. This phenomenon can cause pressure instabilities and interact with impeller by causing power losses due to the increase of the resisting mechanical torque. An illustration of the geometry of the vaneless gap and air-water ring in a reversible pump-turbine is presented in Fig. 3.1.

Two-phase flows interacting with the components of a real size power plant can produce several material damages and electrical power swings by introducing oscillation of the resisting mechanical torque. Müller [79] elucidated the fluid-structure interactions mechanisms related to the cavitation vortex rope at full load in a Francis turbine by showing the correlation of the pressure and torque fluctuations with the cavitating flow. Other examples of structure

behavior depending on the surrounding flow are the variation of structural properties due to hydrodynamics flow instabilities [81] and the induced vibrations [61, 86, 87].

This paper aims to study the characteristics of the flow of the air-water ring and its interaction with the impeller blades in a reduced scale physical model of a reversible pump turbine and the influence on the pressure and torque stability. In particular, the phenomenon is investigated by performing high-speed visualizations together with measurements of the differential pressure between the vaneless gap and the draft tube cone and torque measurements. Tests are performed at several operating points by varying the gauge pressure in the draft tube cone, the water cooling discharge and the rotational speed. A cross-spectral analysis of the signals allows evidencing the correlation within the performed measurements. This also leads to associate the observed two-phase flow in the vaneless gap with the differential pressure fluctuations and elucidate the causes of the recorded instability. The influence of the operating parameters of the machine on the observed two-phase flow phenomena and on the pressure and torque stability is observed. In a specific range of operating conditions, instability of the differential pressure and of the resisting torque are recorded.

In stable condition, the differential pressure can be defined by a set of operating parameters instantiating a parametric model. A cubic multivariate adaptive regression spline (MARS) surrogate model is built as a function of the relevant variables to simulate the differential pressure. A similar approach was used in the design optimization of turbine to predict the performance of the machine [116].

The experimental set-up and the data processing methodology to study the stability of the machine are described in Sec. 3.2 and Sec. 3.3, respectively. The results of the experiments showing the correlation of the flow in the vaneless gap with the pressure and resisting torque fluctuations are presented and discussed in Sec. 3.4. The empirical modeling of the differential pressure at stable condition is detailed in Sec. 3.5.

## 3.2 Experimental set-up

### 3.2.1 Facility

The experiments are performed on a 1:14 reduced scale physical model of a reversible pump-turbine with a specific speed  $n_{QE} = 0.078$  defined as follows:

$$n_{QE} = n \times \frac{Q^{1/2}}{E^{3/4}} \quad (3.1)$$

where  $n$  is the rotating frequency of the impeller ( $s^{-1}$ ),  $Q$  the discharge and  $E$  the machine specific energy.

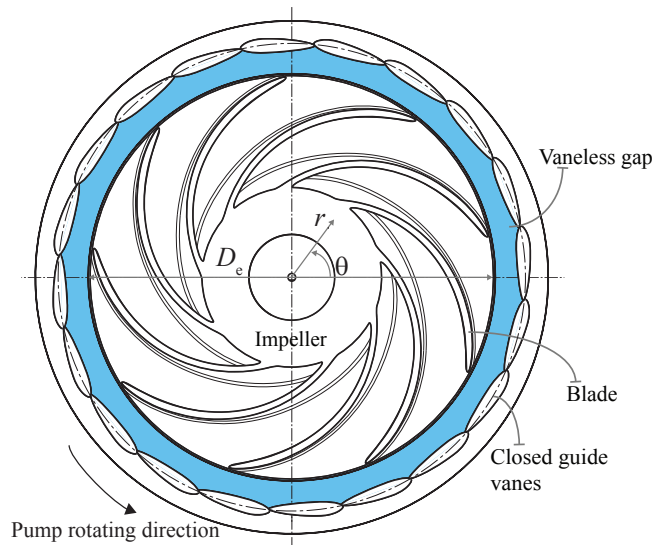


Figure 3.1 – Illustration of the air-water ring in vaneless gap between the closed guide vanes and the impeller blades of a reversible pump-turbine.

A sketch of the main components of the reduced scale model is illustrated in Fig. 3.2. It is composed by the spiral case, 20 guide vanes, 9 blades impeller and the draft tube. The vaneless gap between the impeller and the closed guide vanes measures  $0.06 \times D_e$  in height  $h_{\text{gap}}$  and  $0.09 \times D_e$  in maximum width  $w$  - where  $D_e = 0.304$  m is the high pressure diameter of the impeller. A generator connected to the impeller regulates the rotational speed. The test rig is operated in closed loop configuration and is equipped with an axial pump to generates the specific energy. To operate in condenser mode, the guide vanes are closed and a system of air injection is installed in the draft tube cone. The guide vane closure has 3 mm backlash in geometrical homology with the full scale prototype. A cooling discharge is injected through the labyrinth seals of the pump-turbine and a recycling pipe links the spiral case to the draft tube cone to evacuate the water coming from the guide vanes closure backlash.

The dynamic similarity with the full scale prototype is fulfilled by employing the densimetric Froude similarity as defined in eq. (3.2).

$$Fr_d = \sqrt{\frac{\rho_{\text{air}}}{\rho_{\text{water}}} \frac{\omega \sqrt{D_e}}{\sqrt{g}}} \quad (3.2)$$

$\rho_{\text{air}}$  and  $\rho_{\text{water}}$  are respectively the air and water density,  $\omega$  is the angular speed of the impeller ( $\text{rad}\cdot\text{s}^{-1}$ ). This similarity law has been introduced by Tanaka et al. [100] in the investigation of the sloshing motion of the free-surface in the draft tube cone of a pump-turbine operating in synchronous condenser mode.

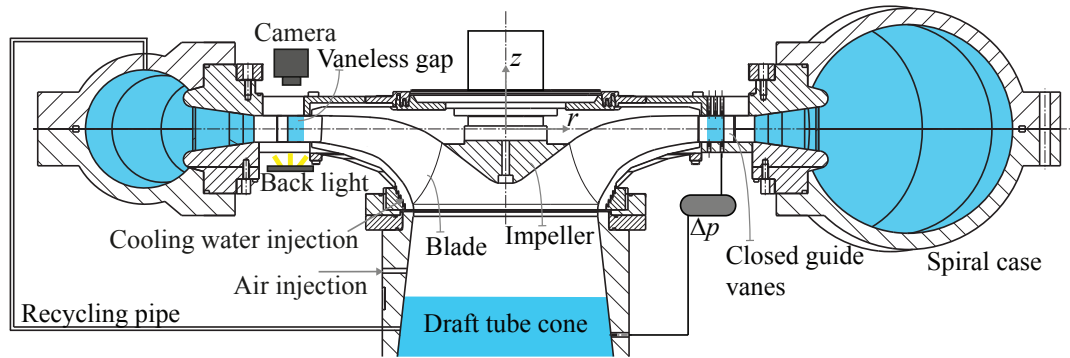


Figure 3.2 – Scheme of the test facility with the instrumentation.

Table 3.1 – Pressure sensors position to measure the gap-cone differential pressure.

Sensor	$r/R_e$ (-)	$z/D_e$ (-)
$p_{\text{gap}}$	1.09	-0.03
$p_{\text{cone}}$	0.88	-0.4

### 3.2.2 Instrumentation

The visualization of the water ring in the vaneless gap between the guide vanes and the impeller blades is performed through two transparent flat windows to guarantee the illumination and the optical access of the vaneless gap and guide vanes as illustrated in Fig. 3.2. The videos of the water ring are recorded using a high-speed camera (Photron FASTCAM MC2.1), at image acquisition rates of 4000 frames per second for 8 s, and resolution of  $512 \times 256$  pixels. A 95 % uniform LED screen (PHLOX LEDW-BL-150/40-LLUB-Q-1R24) of  $150 \text{ mm} \times 40 \text{ mm}$  size and  $35'000 \text{ cd} \cdot \text{m}^{-2}$  luminescence is installed as a back light which ensures the contrast between the gaseous and the liquid phase.

Differential wall pressure measurements  $\Delta p = p_{\text{gap}} - p_{\text{cone}}$  are performed between the vaneless gap and the draft tube cone. The position of the sensors is illustrated in Fig. 3.2 and summarized in Tab. 3.1. The sampling frequency is set at 2400 Hz and 10 s of measurements are recorded. Longer measurements are recorded at 600 Hz and 300 s for specific operating points presenting instability. Torque measurements are also performed by a torque-meter measuring the torque transmitted through the coupling of the impeller and the shaft and corresponding to the mechanical power of the impeller.

All measurements are synchronized with the camera input: the camera gives an input to the acquisition system as external trigger to start simultaneously both high-speed visualization and pressure measurements.

### 3.2.3 Investigated operating points

The operating points are set by fixing the rotational speed of the impeller by an electronic controller, the gauge pressure in the cone of the draft tube is adjusted by using a manometer and the discharge by a valve coupled with an electromagnetic flowmeter.

The operating domain at which the experiments on the reduced scale physical model of a reversible pump-turbine are performed is presented in Fig. 3.3. Each point is also tested by changing the cooling discharge between  $Q = 20 \text{ l}\cdot\text{h}^{-1}$  and  $Q = 80 \text{ l}\cdot\text{h}^{-1}$ . All the operating points are investigated in pump rotating direction. The operating conditions at which the measurements have been performed for an acquisition time  $t_{\text{acq}} = 300 \text{ s}$  are also indicated in Fig. 3.3.

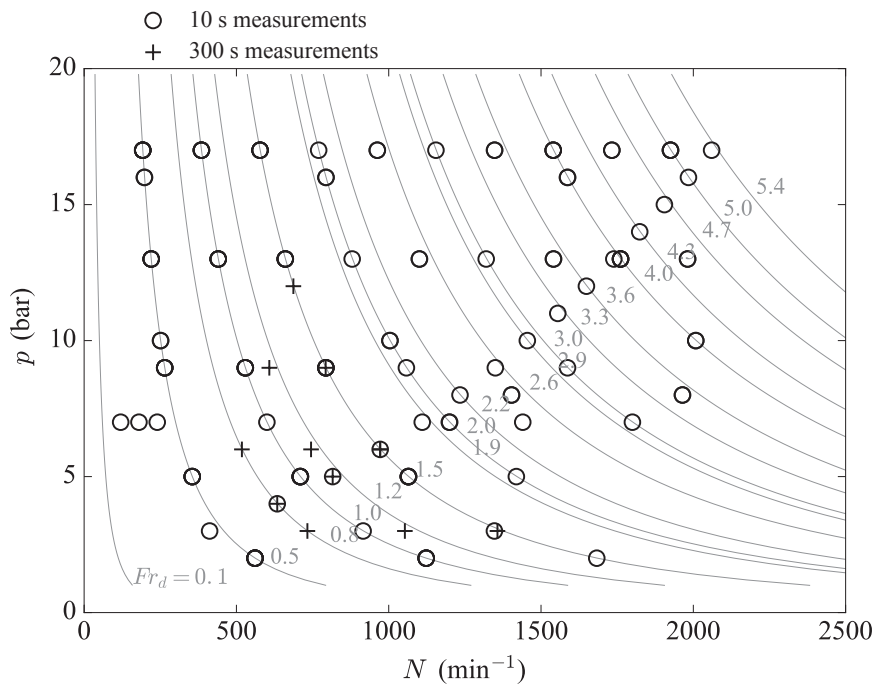


Figure 3.3 – Investigated operating points and iso-Froude curves as a function of the rotational speed  $N$  and the gauge pressure  $p$ .

## 3.3 Study of the machine stability

### 3.3.1 Spectral analysis

Differential pressure and torque measurement are performed for a wide range of operating conditions to identify the conditions at which the machine has a stable operation and the conditions at which instabilities appear. To study the eventual fluctuations, a preliminary analysis in the frequency domain is performed. The auto-spectrum of the signals is computed



to determine the frequency corresponding to the frequency of the periodic instabilities. As an example, as observed in the auto-spectrum of the differential pressure  $G_{xx}$  shown in Fig. 3.4(a), a low frequency fluctuation of the differential pressure is observed. This oscillation is recorded at the operating points with a densimetric Froude number between 0.8 and 2. This fluctuation causes also a torque oscillation as observed in the auto-spectrum of the torque signal  $G_{yy}$  presented in Fig. 3.4(b). To investigate this instability and the correlation between the differential pressure and the torque response in frequency domain, a cross-spectral analysis between the pressure and the torque signals is performed. It includes the computation of the coherence in the frequency domain between the differential pressure and the torque signals, presented in Fig. 3.4(c). The frequency value of the differential pressure and torque swings is made apparent and a coherence value  $C_{xy} > 0.95$  is recorded at the operating conditions presenting instability.

The differential pressure and the torque coefficients are respectively defined as follows:

$$C_{\Delta p} = \frac{\Delta p}{\rho_{\text{water}} g D_e} \quad (3.3)$$

$$C_T = \frac{T_m}{\rho_{\text{water}} g D_e^4} \quad (3.4)$$

In eq. (3.4),  $T_m$  is the resisting mechanical torque transmitted through the coupling of the impeller and the shaft.

The root mean square value of the differential pressure coefficient  $C_{\Delta p, RMS}$  is computed according to eq. (3.5) to evaluate the amplitude of the fluctuation:

$$C_{\Delta p, RMS} = \sqrt{\frac{1}{k} \sum_{i=1}^k (C_{\Delta p, i})^2} \quad (3.5)$$

where  $k$  is the number of samples.

#### 3.3.2 Phase averaging procedure

The torque signals are phase-averaged with respect to the differential pressure signal [40, 80]. Firstly, a noise reduction filter and a high-pass filter with a cut-off frequency of 10 Hz are applied to both the pressure and torque signals. Secondly, the analytic signal of the differential pressure measurement is computed by performing the Hilbert transform [16]. This leads to identify the cycles of the periodic phenomenon of interest with period  $T_{\text{inst}}$  in the differential pressure signal and these are used to identify the synchronized cycles in the torque signal.

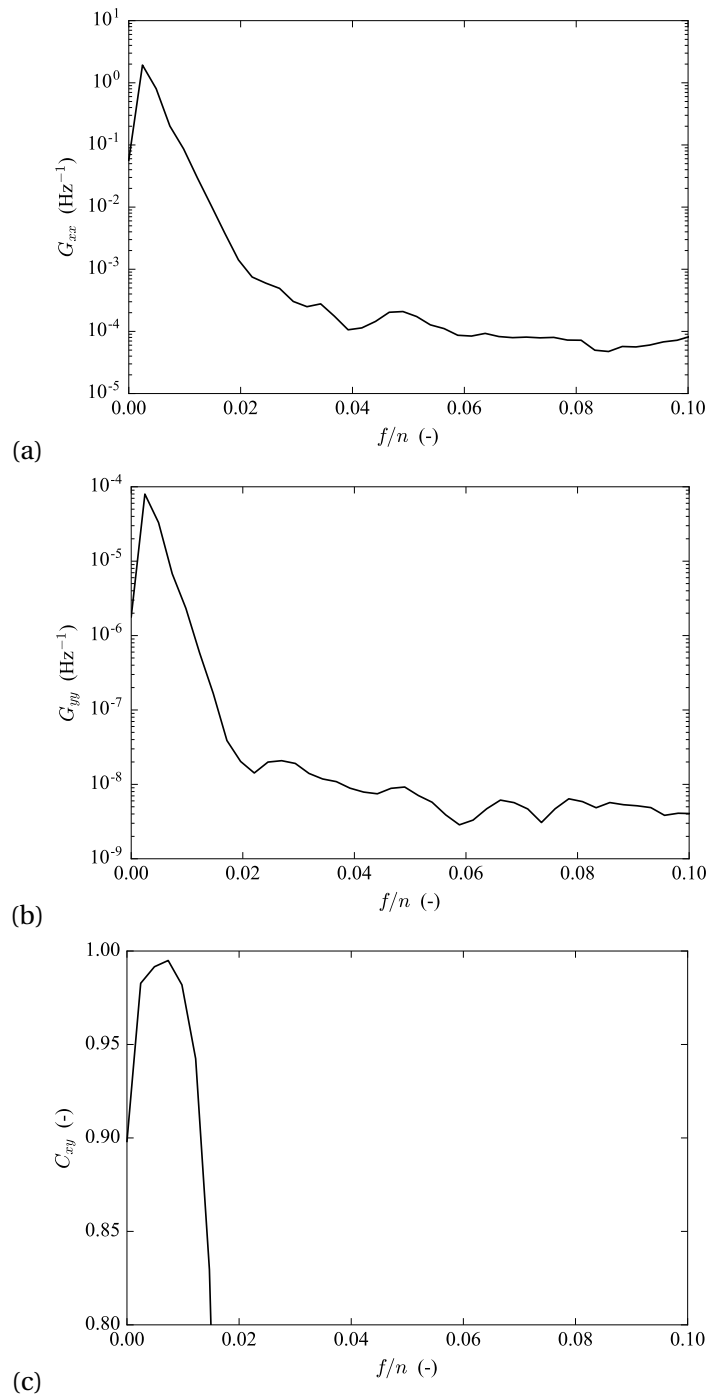


Figure 3.4 – Auto-spectrum in logarithmic scale of the pressure coefficient (a), of the torque coefficient (b) and coherence between the torque and the differential pressure signals (c) at  $Fr_d = 1.2$ ,  $p = 5$  bar and  $Q = 60 \text{ l}\cdot\text{h}^{-1}$ .

Each cycle, corresponding to a period of  $2\pi$  is then divided into 180 phase windows of  $\frac{\pi}{90}$  width.

### 3.3. Study of the machine stability

This allows computing 180 mean torque values, representing the time history of the resisting torque in one typical cycle of the periodic phenomenon. The identification of the cycles is illustrated in Fig. 3.5 and the corresponding phase averaged resisting torque is presented in Fig. 3.6.

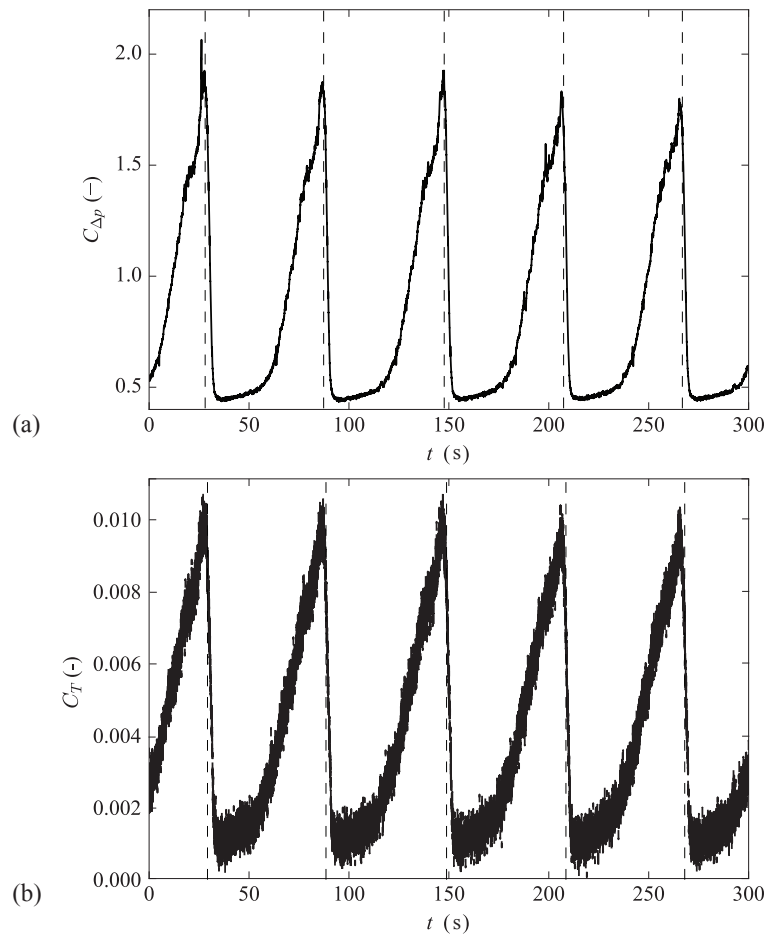


Figure 3.5 – Identification of the instability cycles in the differential pressure signal and the resisting torque signals synchronously measured at  $Fr_d = 1.2$ ,  $p = 5$  bar and  $Q = 60 \text{ l}\cdot\text{h}^{-1}$ . (a) Differential pressure coefficient. (b) Torque coefficient.

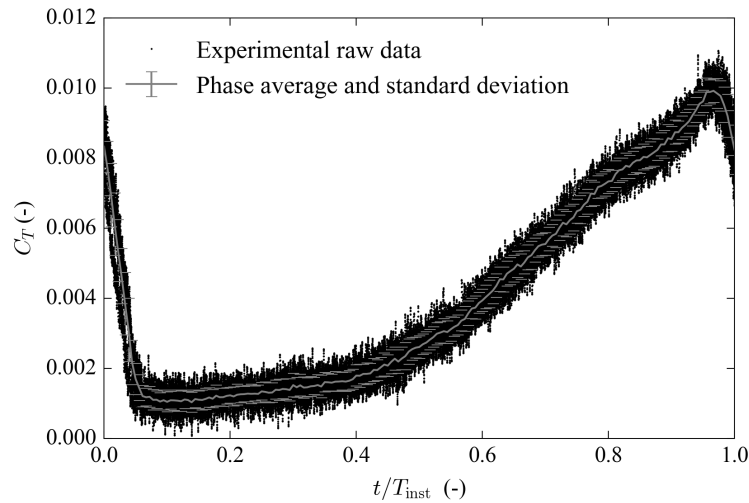


Figure 3.6 – Phase-averaged signal of the resisting torque and its corresponding standard deviation together with the raw data corresponding to the successive cycles of the periodic instability.

## 3.4 Results

### 3.4.1 Flow visualization and correlation with the resisting mechanical torque and differential pressure cone - gap

Four images of the air-water ring in the vaneless gap between the closed guide vanes and the impeller blades at different densimetric Froude number values are illustrated in Fig. 3.7. It is observed that the behavior of the flow in the vaneless gap depends on the densimetric Froude number. Four regimes of the flow are identified depending on the  $Fr_d$  values.

In Regime 1, for  $Fr_d \leq 0.5$  a bubbly flow is observed and the bubble size depends on the pressure: the higher the pressure, the bigger the bubble dimension. The flow in this Regime was previously studied by Vagnoni et al. [111] who investigated both the velocity and the pressure field of the air-water ring.

In Regime 2, for  $0.5 < Fr_d \leq 2$ , a dense bubbly flow is observed and a shrinking of the air-water ring periodically appears at low frequency. When the air-water ring shrinks, the velocity of bubbles decreases and the air-water free-surface of the flow is observed.

Regime 3, for  $2 < Fr_d \leq 3.6$ , is characterized by a thin water ring with capillary waves on the free surfaces. Moreover, a bubbly flow with tiny bubbles appears at the bottom of the flow, under the capillary waves.

In Regime 4, for  $Fr_d > 3.6$ , the air-water ring is characterized by a blurry mixing of air and water pushed against the guide vanes.

Depending on the regime of the flow in the vaneless gap, the mean value of the differential pressure and of the torque coefficient changes. As illustrated in Fig. 3.8, the mean value of the differential pressure coefficient is influenced by the densimetric Froude number and by the regime of the flow. In particular for  $Fr_d > 2$ , the differential pressure coefficient increases by increasing the  $Fr_d$  value. Moreover, a linear relation can be determined between the mean value of the torque coefficient and the differential pressure coefficient, as illustrated in Fig. 3.9. A lower number of torque measurements is available due to inaccuracy of measurements caused by the low value of the recorded torque and the sensitivity of the torque-meter employed for measurements.

In Regime 1 the mean differential pressure coefficient depends on the gauge pressure as illustrated in Fig. 3.10. Since the densimetric Froude number is fixed at 0.5, the increase of the pressure requires a decrease of the rotational speed of the impeller to keep the  $Fr_d$  constant. Indeed, more likely, the decrease of the differential pressure coefficient by increasing the pressure, i.e. decreasing the rotational speed, is due to the interaction between the blades of the impeller and the air-water ring in the vaneless gap whose bubbles dimension depends on the gauge pressure and whose velocity depends on the rotational speed of the impeller [111].

In Fig. 3.8, it is observed that an increase of the mean value of the differential pressure occurs in correspondence of the operating points in Regime 2 which is unrelated to the gauge pressure, to the rotational speed of the impeller and to the water cooling discharge. At this condition, a periodic phenomenon is observed and it causes a periodic oscillation of both the torque and the differential pressure. A detailed study of this phenomenon is further described in Sec. 3.4.2.

In Regime 3 and 4 the differential pressure coefficient increases with the  $Fr_d$  value and a weak variation is noticed by changing the operating condition of the machine at fixed  $Fr_d$  value.

In light of these observations, the air-water ring in the vaneless gap plays a crucial role in the operating condition in condenser mode. Pressure fluctuations are often observed during the operation of hydraulic pump-turbines and they normally have a limited influence on the hydrodynamic properties of the impeller, thus on the torque [10, 80]. Thanks to the high-speed visualizations, evidence is exhibited that the hydrodynamic properties of the impeller are affected by the surrounding flow whose size increases and consequently it interacts with the impeller blades and causes the resulting torque excess.

### 3.4.2 Characterization of the instability caused by the air-water ring

In the images sequence shown in Fig. 3.11, the variation of the flow in the vaneless gap during the operating condition in Regime 2 is presented. In Fig. 3.11, for  $t/T_{inst} > 0.4$ , the flow in the vaneless gap is characterized by a dense bubbly flow which causes the increase of the resisting torque and differential pressure. For  $t/T_{inst} \leq 0.4$ , the air-water ring shrinks causing a sharp decrease of the two measured quantities. Both torque and differential pressure increase when

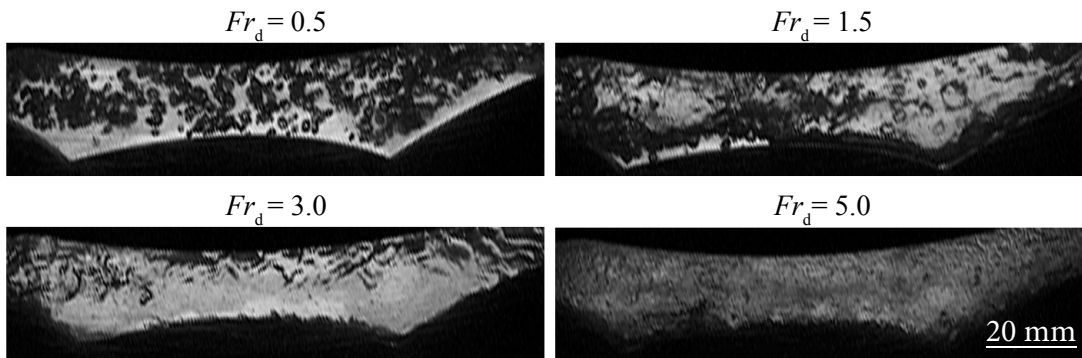


Figure 3.7 – Images of the air-water ring for each flow Regime.

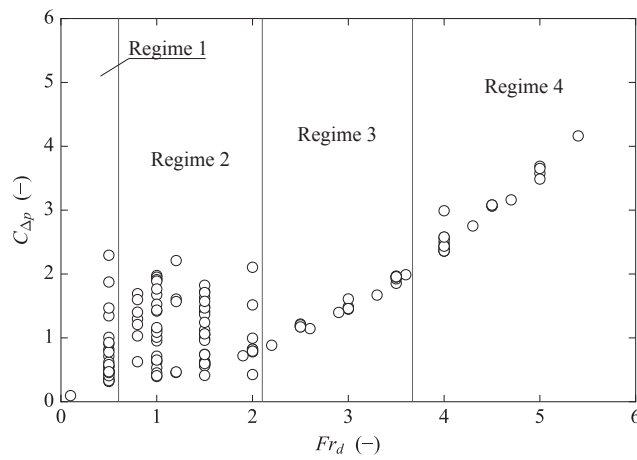


Figure 3.8 – Differential pressure coefficient as a function of the densimetric Froude number.

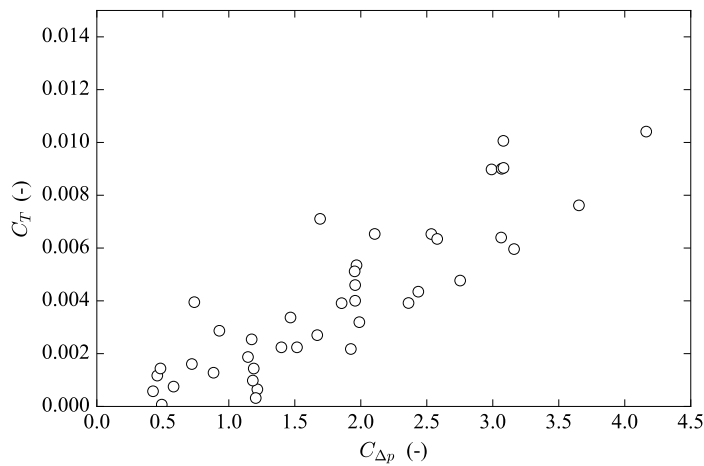


Figure 3.9 – Torque coefficient as a function of the differential pressure coefficient.

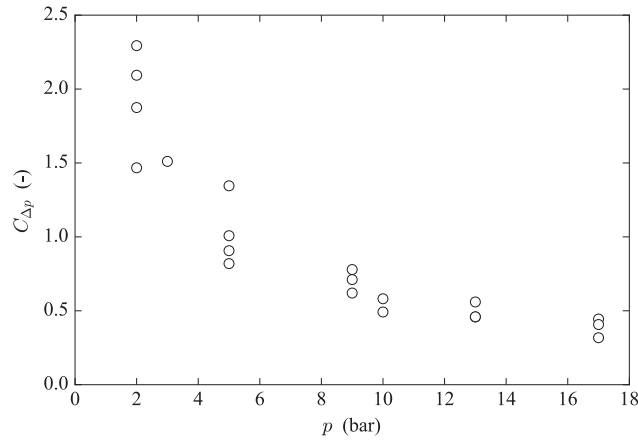


Figure 3.10 – Differential pressure coefficient as a function of the gauge pressure at  $Fr_d = 0.5$ .

the two-phase flow in the vaneless gap features a dense bubbly flow. In this condition the thick water layer interacts with the blade of the impeller causing the increase of the resisting torque. Contrarily, both decrease as soon as the water ring begins to shrink since its interaction with the blades of the impeller becomes limited.

The mean phase averaged of both torque and differential pressure coefficients, showing the periodic instability introduced by the flow in the vaneless gap, is illustrated in Fig. 3.12. The correspondence between the shrinking of the water ring and the decrease of the torque is also shown. The evaluation of the two-phase flow in the vaneless gap is performed by measuring the mean gray level GL as follows:

$$GL = \frac{\sum_{j=1}^{n_{px}} (gl_j)}{\sum_{j=1}^{n_{px}} (gl_{j,cal})} \times 100 \quad (3.6)$$

In eq. (3.6)  $n_{px}$  is the number of pixel in each image,  $gl_j$  is the gray level of each pixel of the image and  $gl_{j,cal}$  is the gray level of each pixel of the calibration image which is a picture of the vaneless gap filled with steady water with no gas.

The dense bubbly flow presents a constant gray level of the image and it is lower than the one of the images with the free-surface which presents an oscillating movement of the flow and where the back light can illuminate part of the image through the free-surface or the liquid phase without bubbles.

As a result of the spectral analysis conducted on the differential pressure signals, the frequency of the periodic instability  $f_{inst}$  is computed and illustrated in Fig. 3.13(a). The frequency increases by increasing the densimetric Froude number, the cooling discharge and by decreasing the gauge pressure. The RMS value of the differential pressure coefficient is presented

### Chapter 3. Torque stability

in Fig. 3.13(b). It is observed that it decreases by increasing the densimetric Froude number. Since the differential pressure signal has limited fluctuations at frequencies different from the frequency of the periodic instability phenomenon, a lower RMS value corresponds to a lower amplitude of the fluctuation caused by the unstable flow.

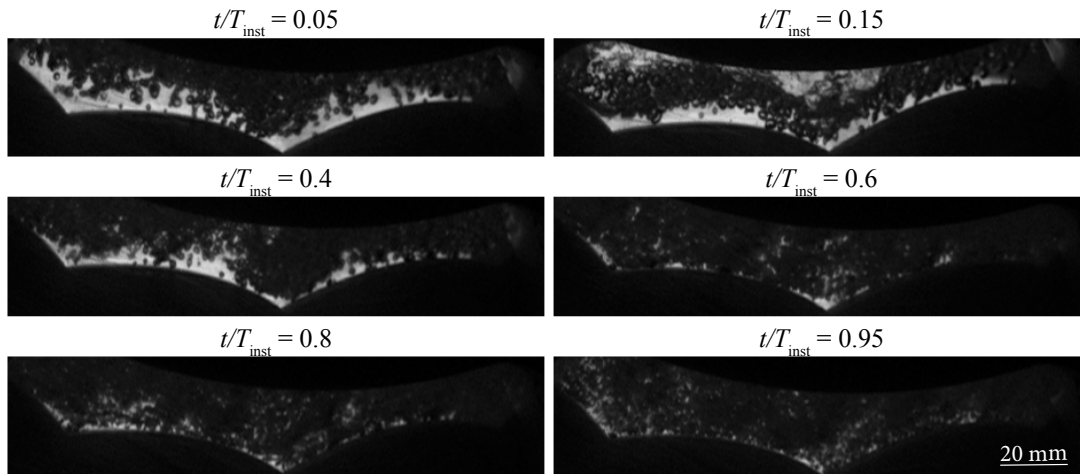


Figure 3.11 – Time history of the air-water ring in the vaneless gap between the closed guide vanes and the impeller blades in one period of the instability in Regime 2 causing torque instability.

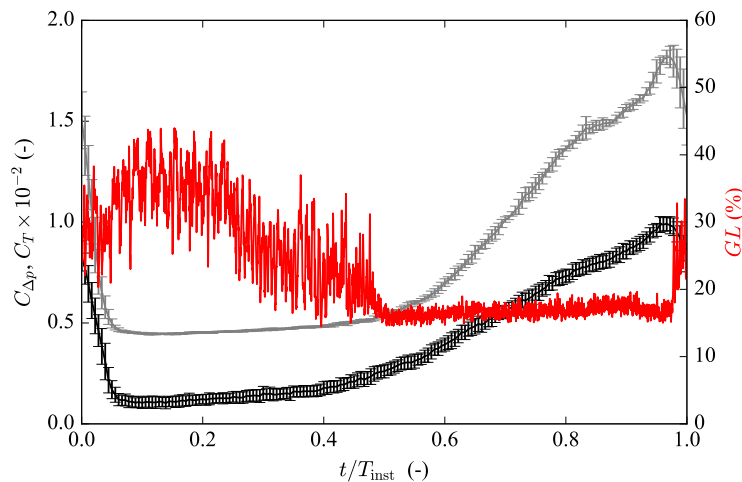


Figure 3.12 – Mean phase averaging of the torque and differential pressure signal together with the  $GL$  values extracted from the high-speed visualization of the air-water ring in one period of the instability at  $Fr_d = 1.2$ .



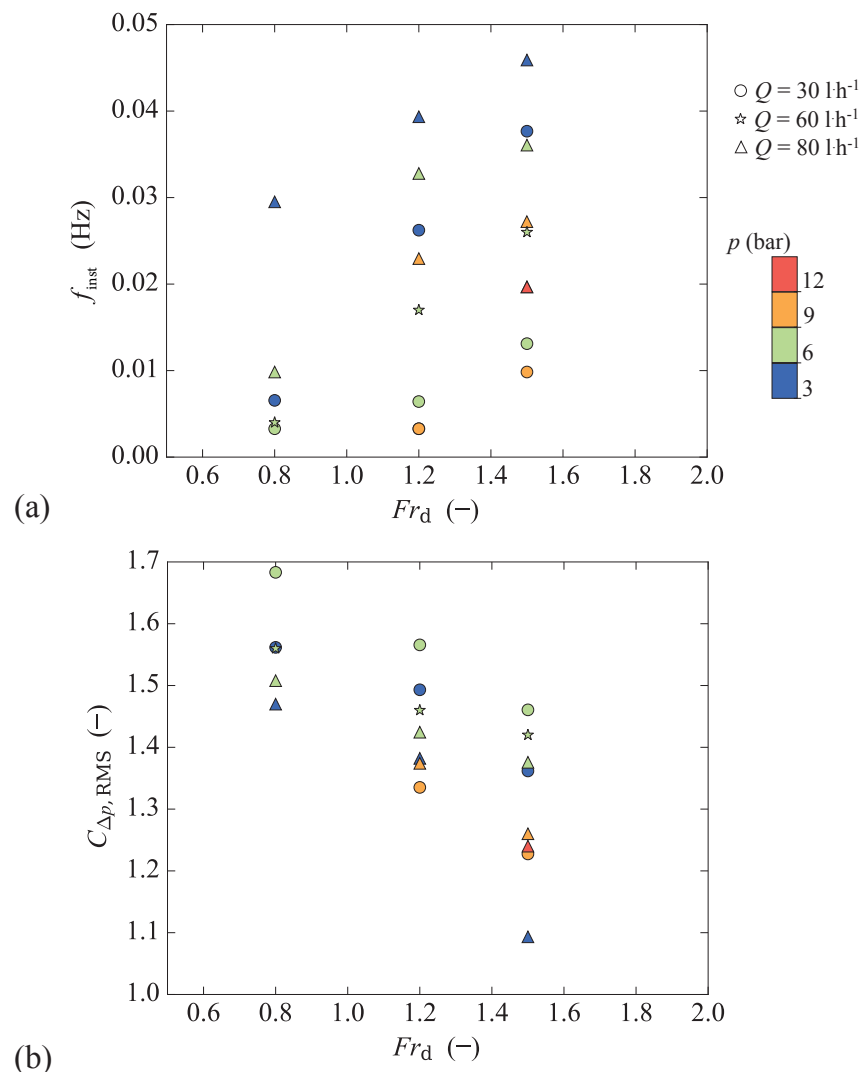


Figure 3.13 – (a) Mean frequency of the periodic instability. (b) RMS of both torque coefficient and differential pressure coefficient as a function of the densimetric Froude number.

### 3.4.3 Instability cause and onset

The recognition of the causes producing the instability recorded is not straightforward in such a complex system. The periodic increase of the differential pressure, corresponding to the increase of the torque, can find its onset in the formation and thickening of the water ring in the vaneless gap due to the water cooling discharge. The periodic instability of the machine operation is likely to be due to the flow in the vaneless gap and its evacuation through the recycling pipe which allows for the water ring shrinking by emptying the vaneless gap of the water ring and filling the draft tube. This explanation is supported by the measurement of the water level in the cone of the draft tube which coherently increases in correspondence of a decrease of the differential pressure and torque and it causes the increase of the pressure in

Table 3.2 – Range of the input parameters to build the model.

Parameter	Min	Max
$Fr_d$	2.2	5.4
$p$	6 bar	17 bar
$N$	$190 \text{ min}^{-1}$	$2050 \text{ min}^{-1}$
$Q$	$20 \text{ l}\cdot\text{h}^{-1}$	$80 \text{ l}\cdot\text{h}^{-1}$

the cone while the pressure in the vaneless gap decrease as illustrated in Fig. 3.14. This can explain the variation of the size of the water ring and the resulting fluctuating interference with the impeller blades causing the swings of the mechanical resisting torque.

This explanation is further strengthened by the dependency of the amplitude and frequency of the instability on the densimetric Froude number, being proportional to the rotational speed of the impeller which provides the centrifugal force to the cooling discharge to arrange the water ring in the vaneless gap. Furthermore, in the unstable regime the water cooling discharge and the gauge pressure play an important role on the characteristics of the recorded instability. The higher cooling discharge the higher is the frequency since the time to fill-up the vaneless gap decreases. It is also observed that lower pressure conditions accelerate the periodic instability by decreasing its period.

## 3.5 Empirical modeling of the differential pressure at stable operating condition

### 3.5.1 Variables definition

As observed in Sec. 3.4.1, unstable operating conditions are highlighted at  $0.5 < Fr_d \leq 2$ . For the other operating conditions at  $Fr_d > 2$ , which are not characterized by flow instability, the dependency between the differential pressure coefficient and the operating parameters is modeled. The choice of modeling the differential pressure coefficient instead of the torque coefficient is due to the higher availability of data of the differential pressure coefficient.

The definition of the parameters to choose as variables of the differential pressure coefficient function has a key role for achieving an unbiased and extended prediction of the differential pressure coefficient. Four possibly influencing parameters are initially identified: the densimetric Froude number, the gauge pressure, the rotational speed of the impeller and the water cooling discharge. The problem can be reduced to three independent variables since the densimetric Froude number depends on the gauge pressure and the rotational speed of the impeller. Tab. 3.2 lists the lower and upper bounds of the explored range for the associated parameters. Those bounds are arbitrarily defined and correspond to the full operating range of the reduced scale model. The condition  $C_{\Delta p} = 0$  at  $Fr_d = 0$  is imposed since the pressure should be uniform in the machine when the impeller is not rotating.

### 3.5. Empirical modeling of the differential pressure at stable operating condition

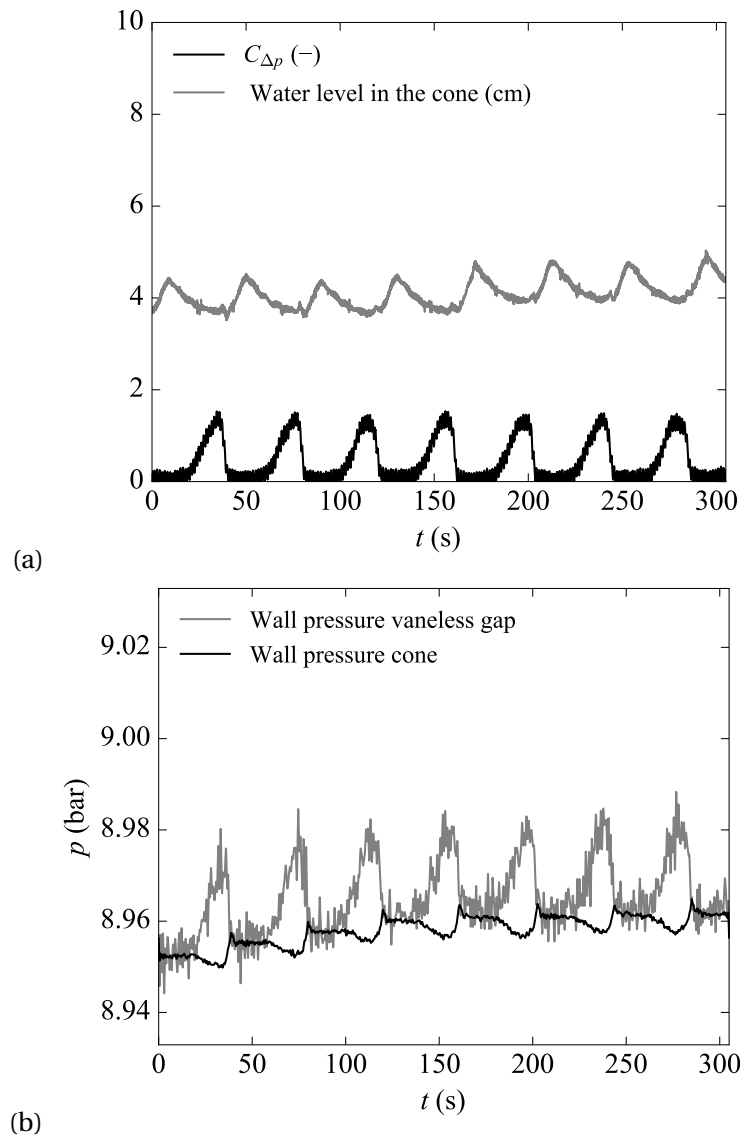


Figure 3.14 – Time history of the water level and  $C_{\Delta p}$  (a) and of the tap wall pressure sensors in the cone of the draft tube and in the vaneless gap at  $Fr_d = 1.2$  and  $Q = 70 \text{ l}\cdot\text{h}^{-1}$ .

#### 3.5.2 Dimension reduction

A Multivariate Adaptive Regression Spline model (MARS) [44] with 18 non-constant basis functions is built with  $N_{sp} = 45$  explored points. The MARS model is selected for its ability to outperform other surrogate modeling techniques, such as neural networks, polynomial chaos expansion, support vector regression or Kriging [11, 116]. The MARS surrogate modeling framework is also well suited to evaluate the importance of each parameter on the  $C_{\Delta p}$  function using only the initial exploration sample. The model consists in a sum of piece-wise spline basis functions whose degree must be set. The best function degree is selected by performing

a preliminary model considering all the parameters and evaluating the Mean Squared Error (MSE) by changing the maximum function degree between 1 and 4. As shown in Fig. 3.15, the best performance is achieved with a sum of piece-wise cubic spline. It is possible to estimate the loss of quality of a model containing all the basis functions but excluding the ones related to one or more variables. Friedman proposed to measure the importance of a parameter through the difference of the Generalized Cross Validation error (GCV) between the full identified model and a model without basis functions involving one or more parameters [44]. The GCV error between the mean differential pressure coefficient  $\overline{C_{\Delta p}}$  and its surrogate model  $\overline{C_{\Delta p}^*}$  is computed according to eq. (3.7), where  $z_M$  is the number of MARS model parameters :

$$\text{GCV} = \frac{1}{N_{\text{sp}}} \frac{\sum_{j=1}^{N_{\text{sp}}} \left( \overline{C_{\Delta p}}(jx) - \overline{C_{\Delta p}^*}(jx) \right)^2}{\left( 1 - \frac{z_M}{N_{\text{sp}}} \right)} \quad (3.7)$$

Removing basis functions involving one or more parameters decreases the number of parameters  $z_M$  of the model but increases the difference between the actual values  $C_{\Delta p}$  and the modeled values  $C_{\Delta p}^*$ . Therefore, a high increase of the GCV when a parameter is removed implies a high importance of this parameter.

This method is used for the evaluation of the variables importance only. The quality of the surrogate model must be verified by ensuring that the  $C_{\Delta p}^*$  function well predicts all the trends of the initial sample. This can be evaluated by the MSE and by the coefficient of determination  $R^2$ , defined in eq. (3.8). It must be verified that this coefficient is close to 1.

$$R^2 = 1 - \frac{\sum_{j=1}^{N_{\text{sp}}} \left( \overline{C_{\Delta p}}(jx) - \overline{C_{\Delta p}^*}(jx) \right)^2}{\sum_{j=1}^{N_{\text{sp}}} \left( \overline{C_{\Delta p}}(jx) - \overline{C_{\Delta p}}(jx) \right)^2} \quad (3.8)$$

where:

$$\overline{C_{\Delta p}}(jx) = \frac{1}{N_{\text{sp}}} \sum_{j=1}^{N_{\text{sp}}} \overline{C_{\Delta p}}(jx) \quad (3.9)$$

#### 3.5.3 Prediction of the differential pressure

The impact of each variable on the  $C_{\Delta p}$  modeling is evaluated and reported in Tab. 3.3. For each variable, The difference  $\Delta\text{GCV}$  between the GCV error of the model with three independent variables and of the model without a variable is computed. Moreover, the MSE related to each

### 3.5. Empirical modeling of the differential pressure at stable operating condition

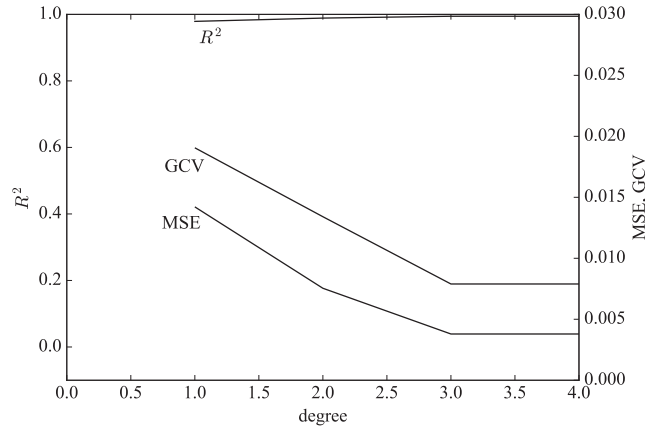


Figure 3.15 – Evaluation of the performance of the surrogate model by changing the maximum interpolation degree.

variable when it is removed as variable of the model is computed. The variables are sorted in decreasing importance and the ranks  $R_{\Delta GCV}$  and  $R_{MSE}$  of each parameter are also presented in Tab.3.3.

For the presented test case the densimetric Froude number appears to be the most important parameter since the surrogate model performance noticeably decreases with the removal of this parameter. The removal of the cooling discharge, the rotational speed and the gauge pressure as input variables does not decrease the performance of the surrogate model, indeed the problem is reduced in dimension with only one input variable:  $Fr_d$ . The solution of the resulting problem is presented in Fig. 3.16, showing a fairly good agreement with the measurements. The function describing the differential pressure coefficient follows in eq. (3.10) and the performance of the surrogate model are listed in Tab. 3.4. As can be seen in Fig. 3.17, the experimental data coincide with the model. Moreover, as illustrated in Fig. 3.18, it is noticed that there is a lack of remaining trend in the representation of the difference between the measured differential pressure coefficient and the model as a function of the four input parameters. This further confirms that it is reasonable to consider the densimetric Froude number as the only variable to model the differential pressure coefficient.

$$C_{\Delta p}^* = a + b \cdot Fr_d + c \cdot Fr_d^2 \quad (3.10)$$

The coefficients estimated by the surrogate model are  $a = 0$ ,  $b = 0.015$  and  $c = 0.12$  for  $Fr_d < 4.5$  and  $a = 3.04$ ,  $b = -1.02$  and  $c = 0.23$  for  $Fr_d \geq 4.5$ .

### Chapter 3. Torque stability

Table 3.3 – Relative importance of the variables of the surrogate model of the differential pressure coefficient, measured thanks to the GCV error and the MSE.

Variable	$\Delta$ GCV	$R_{\Delta\text{GCV}}$	MSE	$R_{\text{MSE}}$
$Fr_d$	0.71	1	0.69	1
$N$	0.00	2	0.01	2
$p$	0.00	2	0.01	2
$Q$	0.00	2	0.01	2

Table 3.4 – Performance of the surrogate model.

Parameter	Value
$R^2$	0.985
GCV	0.016
MSE	0.01

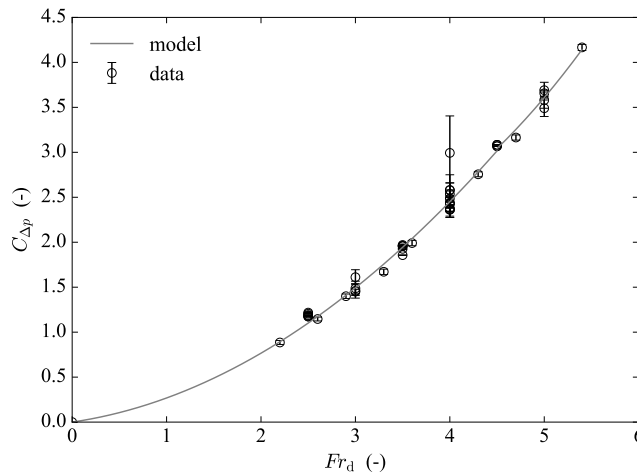


Figure 3.16 – Data set and model of the differential pressure coefficient as a function of the densimetric Froude number validated for  $Fr_d > 2$ .

### 3.6 Conclusion

The two-phase flow in the vaneless gap between the closed guide vanes and the impeller blades is experimentally investigated on the reduced scale physical model of a reversible pump-turbine. High-speed visualizations are performed together with pressure and torque measurements. In particular, the differential pressure between the vaneless gap and the draft tube cone is measured. A preliminary cross-spectral analysis is performed to evaluate the stability of both the torque and the differential pressure. Furthermore, they are compared to the high-speed flow visualization to perform an analysis of the fluid-structure interaction mechanism.

The images of the two-phase flow in the vaneless gap make apparent the onset of an air-

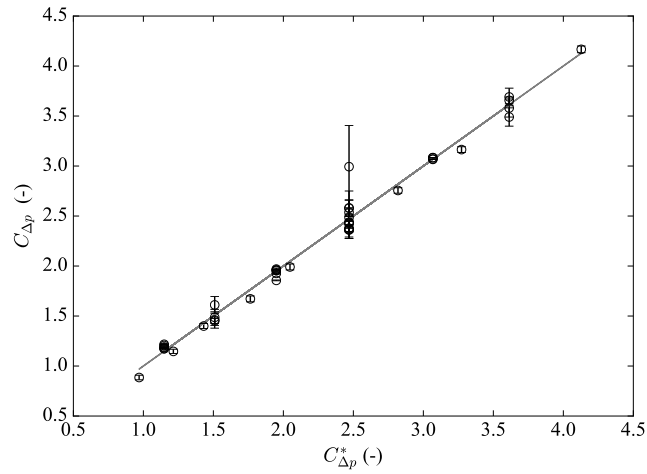


Figure 3.17 – Measured differential pressure coefficient as a function of the model given in eq. (3.10).

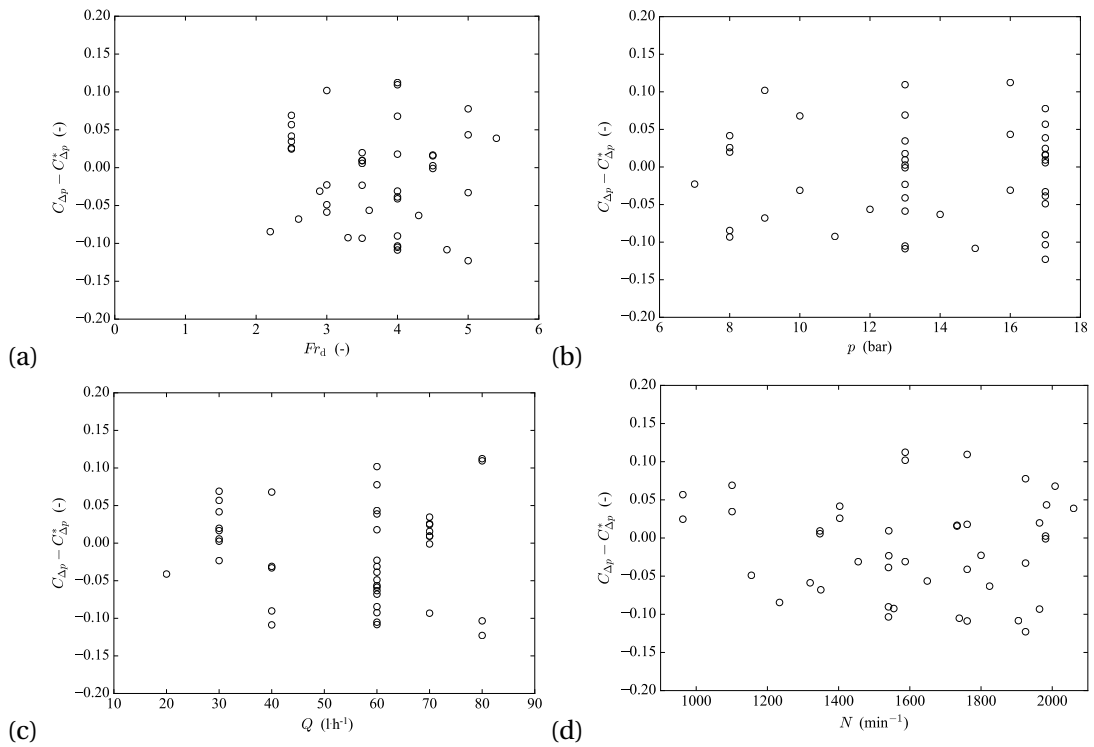


Figure 3.18 – Residual difference between the measured differential coefficient and the model as a function of the densimetric Froude number (a), the gauge pressure (b), the cooling discharge (c) and the rotational speed of the impeller (d).

water ring which hydrodynamics properties depend on the densimetric Froude number. Four regimes are identified as a function of the  $Fr_d$  value.

### Chapter 3. Torque stability

---

The results suggest that the formation of the rotating air-water ring in the vaneless gap can modify the resisting torque by interacting with the impeller blades. The thickening of the air-water ring due to a variation of the differential pressure between the vaneless gap and the draft tube cone is the reason of the increasing resisting torque.

A periodic flow instability causing the fluctuation of the resisting torque is observed in Regime 2. The period of this oscillation is illustrated through the mean phase averaging with respect to the differential pressure signal and the association of several images representing the variation of the hydrodynamic properties of the flow at the corresponding instant of the period.

In the other flow regimes a stable air-water flow is observed. In particular Regime 1 is characterized by a bubbly flow interacting with the impeller blades. The flow characteristics, the torque and differential pressure coefficient are influenced by the rotational speed of the impeller and the gauge pressure. On the other hand, in Regime 3 and 4 this influence is not recorded and the densimetric Froude number appears to be the most relevant parameter.

A cubic MARS modeling of the differential pressure is performed within the stable operating domain for  $Fr_d > 2$ . The surrogate model achieves satisfactory results by considering the densimetric Froude number as the only input parameter. These results back-up the previously observed dependency of the hydrodynamics properties of the flow in the vaneless gap on the densimetric Froude number thanks to the elucidated flow-structure interactions.

Due to the complexity of the problem, several questions on the phenomenon causing instability are still open and require further investigations to be performed. Numerical simulation together with novel experiments could be performed to further investigate the two-phase flow in the vaneless gap and to validate the results achieved. Moreover, a study on the real size prototype could contribute to understand the scale effect of this phenomenon.



## 4 Air diffusion in the liquid volume

### **Oxygen diffusion through air-water free surfaces in a pump-turbine operating in condenser mode**

Reproduced version of:

E. Vagnoni, L. Andolfatto, R. Guillaume, P. Leroy and F. Avellan, *Oxygen diffusion through air-water free surfaces in a pump-turbine operating in condenser mode*, submitted to International Journal of Multiphase Flow (2018).

with the permission of Elsevier.

#### **The author's contribution:**

The author performed the experiments and the data analysis. She developed the theoretical model of the oxygen diffusion in the water volume and made the major contribution to the scaling law of the global diffusion coefficient. She is the first author of this publication.

#### **Abstract**

The present research aims at understanding the mass transfer of air into water in a reversible pump turbine operating in condenser mode. In particular, the diffusion of oxygen through the water free-surface both in the vaneless gap between the impeller blades and the closed guide vanes and in the cone of the draft tube are investigated. A theoretical framework is carried out to compute the diffusion equation describing the oxygen diffusion process in the investigated machine. Oxygen concentration measurements together with temperature and wall pressure measurements are performed to validate the theoretical model of the mass transfer of oxygen in the water volume and to evaluate the influence of the densimetric Froude number, of the gauge pressure and of the cooling discharge on the diffusion process. Moreover, the analytical solution of the diffusion equation applied to both the free surfaces in the vaneless gap and in the cone of the draft tube allows computing the global diffusion coefficient for each air-water free-surface.

The results show that the oxygen concentrations computed by the analytical model of the oxygen diffusion are in agreement with the measurements. The dependency of the oxygen concentration in water on the densimetric Froude number, on the gauge pressure and on the water cooling discharge is also observed. The computed global diffusion coefficients are mainly dependent on the densimetric Froude number in the vaneless gap and in the cone of the draft tube. Finally, the results achieved allow estimating the air losses correlated to the oxygen diffusion causing the increase of the water level in the cone of the draft tube.

**Keywords:** Mass transfer, Oxygen concentration, Free-surface, Densimetric Froude number, Dewatered reversible pump-turbine.

### 4.1 Introduction

In the last decades new renewable energy (NRE) sources have been increasing their production in the electricity mix to meet the goal of reducing green house gases of 20 % by the 2020. NRE sources have a stochastic energy production which, together with the variation of the generation mix and the environmental and regulatory policy changes, increase the need of absorbing or supplying reactive power for voltage regulation to avoid black-outs. Hydro-power units have the capability to regulate the reactive power of the electric grid by operating as synchronous condenser which guarantees the stability of the electrical grid [50]. Since the synchronous condenser mode requires the absorption of active power, the reversible pump-turbines are operated in dewatered condition to minimize the resistant torque of the impeller and so the power consumption. Pressurized air is injected in the machine to maintain the water level in the draft tube below the impeller to minimize the interference with water. The estimation of the compressed air required by this system is important for a proper design of the air injection system. Significant air losses are recorded in a pump-turbine operating in condenser mode and the phenomena governing the air consumption need to be clarified.

Mass transfer of air in water can be one of the causes of the air losses. Diffusion of air in water takes place in each free-surface that arranges an air-water interface. Free surfaces, bubbles and droplets are all affected by diffusion of air in water. As it was previously observed [24, 100, 112], the operation in condenser mode is characterized by a sloshing free-surface in the cone of the draft tube and by a rotating two-phase flow in the vaneless gap between the impeller and the guide vanes [111]. Both arrange a free-surface where air diffusion takes place. The prediction and estimation of the mass transfer of air in water is challenging since the mixing of the two-phase flow introduces a variation of the mass transfer coefficient which depends on the dynamics of the flow. To assess the mass transfer of air and the estimation of the losses due to this phenomenon, an experimental investigation of the time history of oxygen concentration in the water volume is required.

In literature, several fundamental researches have been developed on the diffusion of gases into water [23, 30, 19] or other media such as porous materials [102, 84].

Different experimental methods have been employed to understand and describe the mass transfer of air in water through a free-surface. Soh [97] visualized the void formation on a free-surface when a plunging jet of water impinges on it. This phenomenon has been associated to the water droplets which impinge on the free-surface of a water volume and cause the entrainment of air, so the bubble formation, growth and collapse according to the advection diffusion equation. Chanson [25, 26, 27] studied air-water flow interactions in several conditions and the correlation with the air entrainment, the air bubble formation, the further growth and collapse, and the factors which affect the diffusion phenomenon at the interface between air and water by using conductivity probes.

Several image processing methods have been developed to experimentally study the mass transfer coefficient of the dissolved oxygen concentration in a dense bubbly swarm and to compute the void fraction in liquid volume [31, 41, 95, 103, 120]. Furthermore, several techniques and theoretical models have been developed for investigating mass transfer in rotating bio-reactor with a rotating impeller [60, 71, 107, 118, 121].

The present research presents a novel method for investigating the oxygen diffusion through a water free-surface in a complex two-phase flow system such a reversible pump-turbine. A theoretical framework is carried out starting from the equations describing the mass transfer of oxygen through a free-surface and by developing an analytical solution for the investigated system. The global diffusion coefficients are estimated by solving a numerical problem based on the analytical equations of the oxygen diffusion and on the experimental measurements of oxygen concentration, pressure and temperature. Measurements are performed at several operating condition of the machine. They allow for the validation of the analytical solution of the oxygen mass transfer in the machine and for evaluating the influence of the operating parameters of the machine on the diffusion coefficients.

In Sec. 4.2 the experimental set-up and the investigated operating conditions in the reduced scale physical model of a pump-turbine operating in condenser mode are detailed and in Sec. 4.3 the analytical solution of the mass transfer of air in water in a pump-turbine is described. In Sec. 4.4 the methods used to perform the data post-processing are illustrated and the results achieved are presented in Sec. 4.5. A discussion of the results follows in Sec. 4.6.

## 4.2 Experimental set-up

### 4.2.1 Facility

The experiments are performed on a 1:14 reduced scale physical model of a reversible pump-turbine with a specific speed  $n_{QE} = 0.078$  defined as follows:

$$n_{QE} = n \times \frac{Q^{1/2}}{E^{3/4}} \quad (4.1)$$

## Chapter 4. Air diffusion in the liquid volume

---

where  $n$  is the rotating frequency of the impeller ( $\text{s}^{-1}$ ),  $Q$  the discharge ( $\text{m}^3 \cdot \text{s}^{-1}$ ) and  $E$  the machine specific energy ( $\text{J} \cdot \text{kg}^{-1}$ ).

A sketch of the main components of the reduced scale model is illustrated in Fig. 4.1. It is composed by the spiral case, 20 guide vanes, 9 blades impeller and the draft tube. The vaneless gap between the impeller and the guide vanes measures  $0.06 \times D_e$  in height  $h_{\text{gap}}$  and  $0.09 \times D_e$  in maximum width  $w$ , where  $D_e = 0.304 \text{ m}$  is the high pressure diameter of the impeller. A generator connected to the impeller regulates the rotational speed. The test rig is operated in closed loop configuration and is equipped with an axial pump to generate the specific energy. To operate in condenser mode the guide vanes are closed and a system of air injection is installed in the draft tube cone. The guide vane closure has 3 mm backlash in geometrical homology with the full scale prototype. A cooling discharge is injected through the labyrinth of the pump-turbine. The draft tube end is closed by a blind plate to control the water level and an exiting pipe is placed to evacuate the cooling water discharge.

The dynamic similarity with the prototype is fulfilled by using the densimetric Froude similarity as defined in Eq. 4.2.

$$Fr_d = \sqrt{\frac{\rho_{\text{air}}}{\rho_{\text{water}}} \frac{\omega \sqrt{D_e}}{\sqrt{g}}} \quad (4.2)$$

$\rho_{\text{air}}$  and  $\rho_{\text{water}}$  are respectively the air and water density,  $\omega$  is the angular speed of the impeller ( $\text{rad} \cdot \text{s}^{-1}$ ). This similarity law has been introduced by Tanaka [100] in the investigation of the sloshing motion of the free-surface in the draft tube cone of a pump-turbine operating in synchronous condenser mode.

### 4.2.2 Instrumentation

Oxygen concentration measurements are performed by using T1000 Ocean Optics optical fiber probes in the three sections as indicated in Tab. 4.1. The sensors have 6.35 mm external diameter and 177.8 mm length. The fiber is a 1'000  $\mu\text{m}$  optical fiber (BIFBORO-1000-2) in a stainless steel ferrule. A thermistor probe is included in the sensors for temperature compensation. They allow for both oxygen concentration and temperature measurements in environments up to 21 bar. The acquisition system is Neofox-GT benchtop phase fluorimeter which records  $O_2$  partial pressure by photoluminescence quenching using a ruthenium compound. Measurements are performed at 1 Hz sample rate for 900 s.

Dynamic wall pressure measurements are performed in the vaneless gap between the impeller and guide vanes and in the cone of the draft tube by using flush-mounted piezo-resistive pressure sensors (UNISENSOR HF900-03291.500). They allow for pressure measurements in the range of 0 – 20 bar with a maximum measurement uncertainty of 0.7 %. The position of the sensors is illustrated in Fig. 4.1 and summarized in Tab. 4.1. The sampling frequency is set

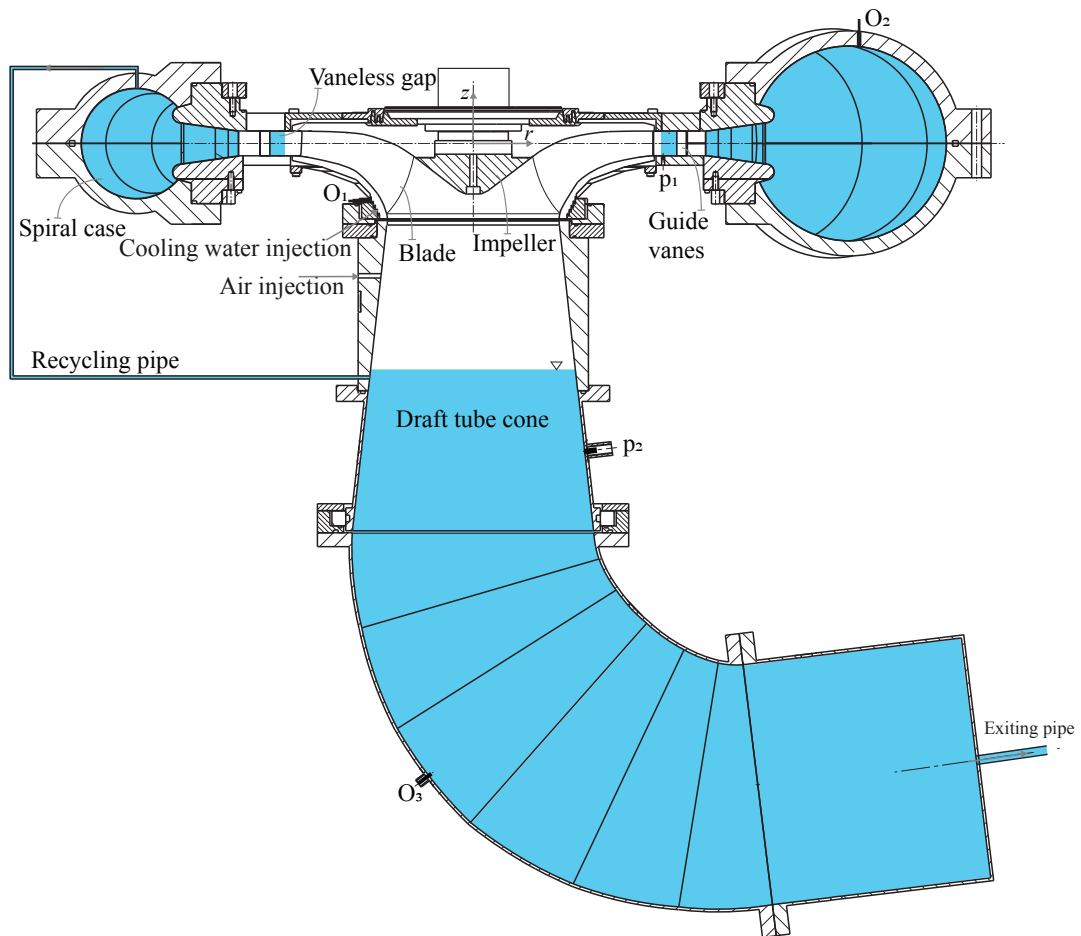


Figure 4.1 – Scheme of the test facility with the instrumentation.

at 300 Hz and measurements are recorded for 900 s.

### 4.2.3 Investigated operating points

The operating points are set by fixing the rotational speed of the impeller by an electronic controller, the gauge pressure in the cone of the draft tube is adjusted by using a manometer and the discharge by a valve coupled with an electromagnetic flowmeter.

The operating domain at which the experiments on the reduced scale physical model of a reversible pump-turbine are performed is presented in Fig. 4.2. Each point is tested at two cooling discharge conditions:  $Q = 40 \text{ l} \cdot \text{h}^{-1}$  and  $Q = 80 \text{ l} \cdot \text{h}^{-1}$ . All the operating points are investigated in pump rotating direction.

## Chapter 4. Air diffusion in the liquid volume

Table 4.1 – Oxygen probes position.

Sensor	$r/R_e$ (-)	$z/D_e$ (-)
O1	0.72	-0.26
O2	1.97	0.16
O3	0.7	-1.14

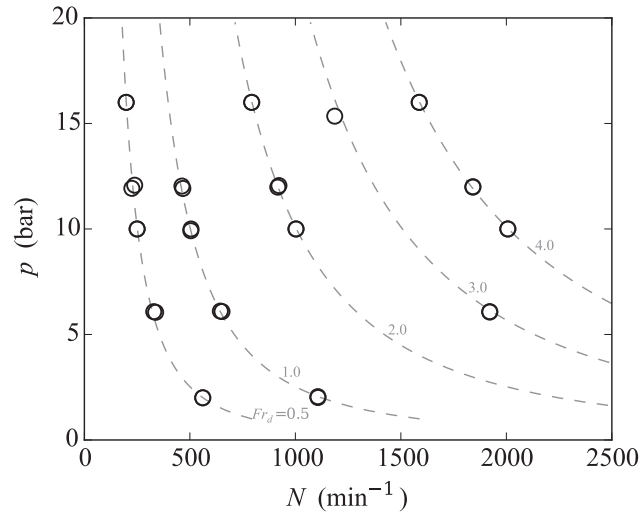


Figure 4.2 – Investigated operating points on the iso-Froude curve as a function of the rotational speed  $N$  and the gauge pressure  $p$ .

### 4.3 Analytical solution

The air concentration in water in saturated condition is computed as the sum of the oxygen and the nitrogen saturated concentration values in water [15].

$$x_{\text{air,sat}} = x_{O_2,\text{sat}} + x_{N_2,\text{sat}} \quad (\text{mol}\cdot\text{m}^{-3}) \quad (4.3)$$

Following Henry equation [54] it is possible to compute both the  $O_2$  and  $N_2$  concentration in water at the saturation point:

$$x_{O_2,\text{sat}} = \frac{p_{p,O_2}}{He} \cdot MM_{O_2} \quad (\text{mol}\cdot\text{m}^{-3}) \quad (4.4)$$

$$x_{N_2,\text{sat}} = \frac{p_{p,N_2}}{He} \cdot MM_{N_2} \quad (\text{mol}\cdot\text{m}^{-3}) \quad (4.5)$$

### 4.3. Analytical solution

Where  $p_{p,O_2}$  and  $p_{p,N_2}$  are the partial pressure of oxygen and nitrogen considering the air composition 21%  $O_2$  and 79%  $N_2$ .

The variation of the oxygen concentration in a closed system -where air and water are contained in a volume  $V$  and separated by a free-surface of area  $A$ - is defined by the mass balance considering a flux of oxygen through the exchanging free-surface.

$$\frac{dx_{O_2}^{liq}}{dt} \cdot V = q_{O_2,in} \cdot A - q_{O_2,out} \cdot A \quad (\text{mol} \cdot \text{s}^{-1}) \quad (4.6)$$

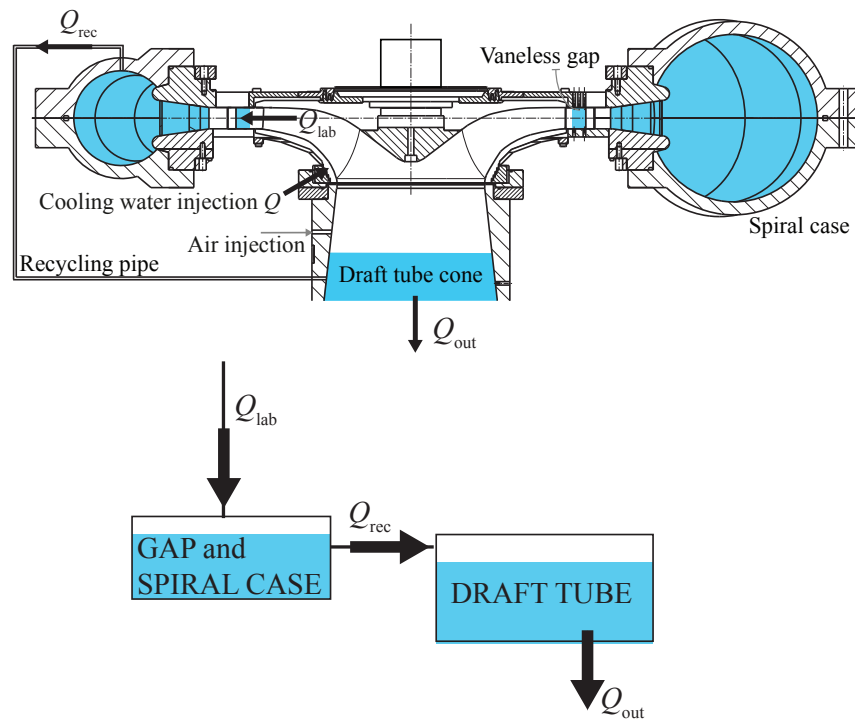


Figure 4.3 – Scheme of the water volumes and flows considered to perform the theoretical framework of the diffusion of air in water in the reduced scale physical model of a reversible pump-turbine.

In a reversible pump-turbine operating in condenser mode, two free surfaces are identified: one in the vaneless gap between the impeller and the guide vanes and the other in the cone of the draft tube. As illustrated in Fig. 4.3, the two water volumes which arrange a free surfaces are linked by the recycling pipe through the spiral case which is fully filled up by water. The water volume of the vaneless gap and the water volume of the spiral case are considered as one single volume  $V_{gap}$  linked to the water volume in the draft tube  $V_{cone}$ . In this modeling, the two water volumes are considered constant since their variation in time is negligible, less than 5 %, if compared to the total volume. This configuration is validated for the operating

## Chapter 4. Air diffusion in the liquid volume

points with  $Fr_d > 0.5$  while for lower  $Fr_d$  values the cooling discharge trickles directly in the draft tube cone from the vaneless gap and so this model can not be applied.

The variations of the concentration of the oxygen in the vaneless gap and spiral case  $x_{O_2, \text{gap}}^{\text{liq}}$  and in the draft tube  $x_{O_2, \text{cone}}^{\text{liq}}$  in water by considering the diffusion of air in water and the discharge of oxygen coming in and out the water volumes are defined as follows:

$$\begin{cases} \frac{dx_{O_2, \text{gap}}^{\text{liq}}}{dt} \cdot V_{\text{gap}} = q_{O_2, \text{in}} \cdot A_{\text{gap}} - q_{O_2, \text{out}} \cdot A_{\text{gap}} + Q_{\text{lab}} - Q_{\text{rec}} & (\text{mol} \cdot \text{s}^{-1}) \\ \frac{dx_{O_2, \text{cone}}^{\text{liq}}}{dt} \cdot V_{\text{cone}} = q_{O_2, \text{in}} \cdot A_{\text{cone}} - q_{O_2, \text{out}} \cdot A_{\text{cone}} + Q_{\text{rec}} - Q_{\text{out}} & (\text{mol} \cdot \text{s}^{-1}) \end{cases} \quad (4.7)$$

$$\begin{cases} Q_{\text{lab}} = Q \cdot x_{O_2, 0}^{\text{liq}} \\ Q_{\text{rec}} = Q \cdot x_{O_2, \text{gap}}^{\text{liq}} \\ Q_{\text{out}} = Q \cdot x_{O_2, \text{cone}}^{\text{liq}} \end{cases} \quad (\text{mol} \cdot \text{s}^{-1}) \quad (4.8)$$

Where  $Q$  is the water cooling discharge and  $x_{O_2, 0}^{\text{liq}}$  is the initial concentration of oxygen in the cooling water discharge before entering the pump-turbine. The area  $A_{\text{gap}} = 2\pi R_e \cdot h_{\text{gap}}$  and  $A_{\text{cone}} = \pi(D/2)^2$  are the geometrical area of the free surfaces in the vaneless gap and in the cone of the draft tube, respectively. The diameter of the cone  $D$  is evaluated at the initial position of the air-water interface in the cone. The flux of oxygen  $q_{O_2, \text{out}}$ , which is exiting the system, is zero since no water is evaporating. The flux of oxygen which is coming in the water volume due to the diffusion phenomenon is defined by Fick's law [43] as follows:

$$q_{O_2, \text{in}} = K_G (p_{O_2}^{\text{gas}} - p_{O_2}^{\text{i}}) \quad (\text{mol} \cdot \text{s}^{-1} \cdot \text{m}^{-2}) \quad (4.9)$$

With  $K_G$  the mass gas coefficient for the gas phase,  $p_{O_2}^{\text{gas}}$  is the oxygen partial pressure in the phase gas and  $p_{O_2}^{\text{i}}$  is the interface partial pressure of oxygen.

The mass transfer of oxygen can be written also as a function of the concentration changing in the liquid phase since at steady-state the oxygen flux in one phase must equal the oxygen flux in the other phase. Therefore, these two fluxes equate:

$$q_{O_2, \text{in}} = K_L (x_{O_2}^{\text{i}} - x_{O_2}^{\text{liq}}) \quad (\text{mol} \cdot \text{s}^{-1} \cdot \text{m}^{-2}) \quad (4.10)$$

$K_L$  is the mass transfer coefficient in liquid phase,  $x_{O_2}^{\text{liq}}$  is the bulk liquid oxygen concentration



and  $x_{O_2}^i$  is the interface concentration of oxygen in the liquid. By assuming a steady state condition at the interface and the equilibrium condition between the two phases, Henry's equation is applied at the interface in the mass transfer in liquid phase:

$$p_{O_2}^i = He \cdot x_{O_2}^i \quad (\text{Pa}) \quad (4.11)$$

With He Henry constant for oxygen depending on the temperature. The flux in the liquid phase becomes:

$$q_{O_2, \text{in}} = K_L \left( \frac{p_{O_2}^p}{He} - x_{O_2}^{\text{liq}} \right) \quad (\text{mol} \cdot \text{s}^{-1} \cdot \text{m}^{-2}) \quad (4.12)$$

It is usually not possible to measure the partial pressure and concentration at the interface. It is therefore convenient to define overall mass transfer coefficients based on an overall driving force between the bulk compositions. For the physical situation of oxygen transporting from air to water, the overall mass transfer coefficient is defined taking in account the entire diffusional resistance in both phases. By substituting eq. (4.12) in eq. (4.9):

$$q_{O_2, \text{in}} = \frac{K_G}{1 - He/K_G} (p_{O_2}^p - He \cdot x_{O_2}^{\text{liq}}) \quad (\text{mol} \cdot \text{s}^{-1} \cdot \text{m}^{-2}) \quad (4.13)$$

The overall mass transfer coefficient is so defined as follows:

$$K = \frac{K_G}{1 - He/K_L} \quad (\text{m} \cdot \text{s}^{-1}) \quad (4.14)$$

To solve the variation of concentration in a liquid volume, the overall mass transfer defined by eq. (4.14) is substituted in eq. (4.13):

$$q_{O_2, \text{in}} = K \left( \frac{p_{O_2}^p}{He} - x_{O_2}^{\text{liq}} \right) = K (x_{O_2, \text{sat}}^{\text{liq}} - x_{O_2}^{\text{liq}}) \quad (\text{mol} \cdot \text{s}^{-1} \cdot \text{m}^{-2}) \quad (4.15)$$

Indeed, eq. (4.7) can be rewritten as follows:

$$\begin{cases} \frac{dx_{O_2, \text{gap}}^{\text{liq}}}{dt} \cdot V_{\text{gap}} = K_{\text{gap}} \cdot A_{\text{gap}} (x_{O_2, \text{sat, gap}}^{\text{liq}} - x_{O_2}^{\text{liq}}) + Q_{\text{lab}} - Q_{\text{rec}} & (\text{mol} \cdot \text{s}^{-1}) \\ \frac{dx_{O_2, \text{cone}}^{\text{liq}}}{dt} \cdot V_{\text{cone}} = K_{\text{cone}} \cdot A_{\text{cone}} (x_{O_2, \text{sat, cone}}^{\text{liq}} - x_{O_2}^{\text{liq}}) + Q_{\text{rec}} - Q_{\text{out}} & (\text{mol} \cdot \text{s}^{-1}) \end{cases} \quad (4.16)$$

## Chapter 4. Air diffusion in the liquid volume

The solution of the differential equation in eq. (4.16) is:

$$\begin{cases} x_{O_2, \text{gap}}^{\text{liq}} = x_{O_2, 0}^{\text{liq}} \cdot \exp\left(-\frac{1}{\tau_{1, \text{gap}}} t\right) + x_{O_2, \text{lim}, \text{gap}}^{\text{liq}} \cdot (1 - \exp\left(-\frac{1}{\tau_{1, \text{gap}}} t\right)) & (\text{mol} \cdot \text{m}^{-3}) \\ x_{O_2, \text{cone}}^{\text{liq}} = x_{O_2, 0}^{\text{liq}} \cdot \exp\left(-\frac{1}{\tau_{1, \text{cone}}} t\right) + x_{O_2, \text{lim}, \text{cone}}^{\text{liq}} \cdot (1 - \exp\left(-\frac{1}{\tau_{1, \text{cone}}} t\right)) & (\text{mol} \cdot \text{m}^{-3}) \end{cases} \quad (4.17)$$

In eq.4.17 the following parameters are defined for the diffusion through the water free-surface in the vaneless gap:

$$\begin{cases} \tau_{0, \text{gap}} = V_{\text{gap}} / (A_{\text{gap}} \cdot K_{\text{gap}}) & (\text{s}) \\ \tau_{1, \text{gap}} = \tau_{0, \text{gap}} \frac{1}{1 + \frac{Q}{V_{\text{gap}}} \cdot \tau_{0, \text{gap}}} & (\text{s}) \\ x_{O_2, \text{lim}, \text{gap}}^{\text{liq}} = \frac{\tau_{1, \text{gap}}}{\tau_{0, \text{gap}}} x_{O_2, \text{sat}, \text{gap}}^{\text{liq}} + \frac{Q_{\text{lab}}}{V_{\text{gap}}} \cdot \tau_{1, \text{gap}} & (\text{mol} \cdot \text{m}^{-3}) \end{cases} \quad (4.18)$$

For the diffusion through the water free-surface in the draft tube cone the following parameters are defined:

$$\begin{cases} \tau_{0, \text{cone}} = V_{\text{cone}} / (A_{\text{cone}} \cdot K_{\text{cone}}) & (\text{s}) \\ \tau_{1, \text{cone}} = \tau_{0, \text{cone}} \frac{1}{1 + \frac{Q}{V_{\text{cone}}} \cdot \tau_{0, \text{cone}}} & (\text{s}) \\ x_{O_2, \text{lim}, \text{cone}}^{\text{liq}} = \frac{\tau_{1, \text{cone}}}{\tau_{0, \text{cone}}} x_{O_2, \text{sat}, \text{cone}}^{\text{liq}} + \frac{Q_{\text{rec}}}{V_{\text{cone}}} \cdot \tau_{1, \text{cone}} & (\text{mol} \cdot \text{m}^{-3}) \end{cases} \quad (4.19)$$

The global diffusion coefficients of the diffusion of oxygen in water through the free surfaces in the vaneless gap and in the cone of the draft tube are unknown. In a quiescent water volume the overall mass transfer coefficient for oxygen at atmospheric pressure and  $\Theta = 288$  K is  $K = 1.74 \cdot 10^{-5} \text{ dm} \cdot \text{s}^{-1}$  [42]. In the system of the present research, the free-surface in the vaneless gap is characterized by a rotating air-water flow and the free-surface in the cone is characterized by a non-linear sloshing [100, 111]. Both free surfaces are not stationary and their dynamics causes the variation of both the geometrical area of the free-surface and the global diffusion coefficient. These variations can be experimentally determined by computing the global diffusion coefficients  $K_{\text{gap}}$  and  $K_{\text{cone}}$  which take into account both the variation of the area of the free-surface and of the diffusion coefficient due to the air-water mixing. This is implemented by measuring the oxygen concentration at the condition  $x_{O_2, \text{lim}}^{\text{liq}}$ , which is lower than the concentration at the saturation point due to the flow discharge, and by solving eq. (4.16) with the experimental data. The method to solve this equation system will be further explained in Sec. 4.4.1.

## 4.4 Data processing method

### 4.4.1 Estimation of the global diffusion coefficients in the vaneless gap and in the cone.

The oxygen concentration measurements are performed on the stabilized oxygen concentration in the machine at each sections where measurements are performed. This takes maximum 40 min for each operating point. The measured values of oxygen concentration allow computing the global diffusion coefficient for the diffusion of oxygen in water through the free-surface in both vaneless gap and draft tube cone. Those coefficients are computed by solving the following problem for each investigated point  $j$ :

$$(K_{\text{gap},j}, K_{\text{cone},j}) = \operatorname{argmin}_j \{ |x_{O_2, \text{lim}, \text{gap}, j}^{\text{liq}} - x_{O_2, O_2, j}^{\text{liq}}|, |x_{O_2, \text{lim}, \text{cone}, j}^{\text{liq}} - x_{O_2, O_3, j}^{\text{liq}}| \} \quad (4.20)$$

where  $x_{O_2, O_2, j}^{\text{liq}}$  and  $x_{O_2, O_3, j}^{\text{liq}}$  are the mean value of the measured oxygen concentrations at the location O2 and O3, respectively.

The problem is solved by using the open source Python library *scipy.optimize* [63] which solves a nonlinear least-squares problem with bounds on the variables. The initial condition is given by the measurement of the oxygen concentration at the inlet section of the water cooling discharge. Moreover, the bounds  $K_{\text{gap},j}, K_{\text{cone},j} > 0$  are imposed.

### 4.4.2 Estimation of the oxygen diffused in water in the cone of the draft tube by measuring the water level elevation

The water level in the draft tube increases due to the air volume  $V_{\text{air}}$  lost due to the diffusion in water through the free-surface. By measuring the variation of the water level it is possible to estimate the quantity of air lost through mass transfer into water and to verify that the correspondent quantity of oxygen is equivalent to the variation in concentration of oxygen measured between the inlet and the draft tube cone of the machine. To verify this equivalence a strong hypothesis is done about the air composition in water. It is supposed that the diffusion in water of the different gases composing air is uniform, while it has been demonstrated that it slightly changes due to the different diffusion coefficients of the gases [15, 14, 67]. The variation in time of the mass of oxygen  $\dot{m}_{O_2}$  in the air volume is computed by solving the mass balance equation as a function of the water level variation  $\frac{dl}{dt}$ , as follows:

$$\dot{m}_{O_2, \text{computed}} = \frac{dm_{O_2}}{dt} = \frac{dm_{O_2}}{dl} \cdot \frac{dl}{dt} \quad (\text{kg} \cdot \text{s}^{-1}) \quad (4.21)$$

## Chapter 4. Air diffusion in the liquid volume

By applying the ideal gas equation  $p_{p,O_2} \cdot V_{\text{air}}(l) = n_{O_2} \cdot R \cdot \Theta$  and by knowing that the number of moles  $n_{O_2}$  can be expressed as  $n_{O_2} = m_{O_2} / MM_{O_2}$ , eq. (4.21) can be rewritten as follows:

$$\dot{m}_{O_2, \text{computed}} = \frac{p \cdot X_{O_2} \cdot MM_{O_2}}{R \cdot \Theta} \cdot \frac{dV_{\text{air}}}{dl} \cdot \frac{dl}{dt} \quad (\text{kg} \cdot \text{s}^{-1}) \quad (4.22)$$

The volume depends on the water level due to the conical shape of the draft tube cone. The measurement of water level  $l$  is linearized by performing a linear interpolation since the water level is oscillating due to the sloshing motion of the free-surface in the cone of the draft tube, as presented in Fig. 4.4.

The measurement of the oxygen concentration the inlet and the draft tube cone of the machine allows computing the mass flow rate of oxygen exiting the machine as follows:

$$\dot{m}_{O_2, \text{measured}} = (x_{O_2, O3}^{\text{liq}} - x_{O_2, O1}^{\text{liq}}) \cdot MM_{O_2} \cdot Q \quad (\text{kg} \cdot \text{s}^{-1}) \quad (4.23)$$

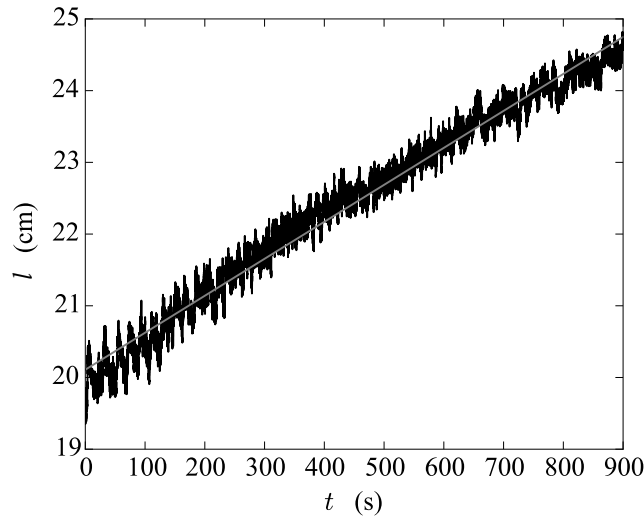


Figure 4.4 – Time history of the water level at  $Fr_d = 4$ ,  $p = 10 \text{ bar}$  and  $Q = 80 \text{ l} \cdot \text{h}^{-1}$ .

## 4.5 Results

### 4.5.1 Evolution of the oxygen concentration in the water volume

The saturation condition of oxygen in water is linearly dependent on the gauge pressure according to Henry's equation in eq. (4.11) as shown in Fig. 4.5. This means that the higher the pressure, the higher is the amount of oxygen which can diffuse in water. To further evaluate

the influence of the gauge pressure on the diffusion of oxygen in the water flow in the pump turbine, the measured oxygen concentration is divided by the concentration at the saturation condition.

In Fig. 4.6 is presented an example of the time solved oxygen concentration measurement divided by the concentration at the saturation condition at the three locations illustrated in Fig. 4.1. For all the investigated operating points, the stability of the oxygen concentration must be verified.

The mean values of the oxygen concentration measured in the spiral case and in the draft tube cone of the machine are illustrated for all the investigated operating points in Fig. 4.7 (a) and (b), respectively. A first discussion on the average value of the oxygen concentration at each measurements location is presented.

#### **Sensor O1 – Cooling discharge inlet**

The average concentration of the cooling discharge is constant for all the investigated operating points and equal to 1.9 ppm. This value is needed to compute the analytical solution of the diffusion problem explained in Sec. 4.3 as it corresponds to the initial condition  $x_{O_2,0}^{liq}$ .

#### **Sensor O2 – Spiral case**

The mean value of the oxygen concentration in the flow in vaneless gap counts for at least 30 % of the concentration at the saturation condition for all the investigated points. Indeed, a significant amount of oxygen diffuses in the water flow through the free-surface in the vaneless gap.

#### **Sensor O3 – Draft tube**

The mean value of the oxygen concentration in the draft tube divided by the concentration at the saturation condition increases with respect to the oxygen concentration in the vaneless gap. The diffusion of oxygen takes place through the water free-surface in the cone of the draft tube which explains the increase of the oxygen concentration. It is noticed that this increase counts between 3 % and 10 % of the saturation condition for  $Fr_d < 2$  while it increases almost 20 % of the saturation condition with respect to the concentration in the spiral case for the operating points at higher densimetric Froude number.

For all measurements at the same densimetric Froude number and cooling discharge condition, the gauge pressure has a limited influence on the oxygen concentration divided by the concentration at the saturation condition, as observed in Fig. 4.7.

The densimetric Froude number has a relevant influence on the oxygen concentration. It increases by increasing the  $Fr_d$  value. It is also noticed that the cooling discharge influences the concentration of oxygen in the water flow: the higher the discharge, the lower is the concentration, accordingly to the theoretical framework developed since by increasing the cooling discharge the maximum oxygen concentration that can be reached in the flow is lower.

## Chapter 4. Air diffusion in the liquid volume

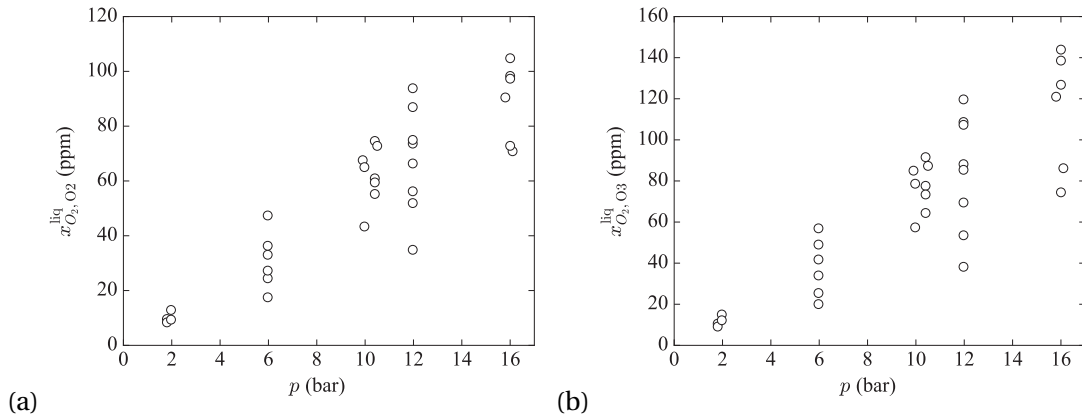


Figure 4.5 – Averaged value of the measured oxygen concentration in the spiral case (a) and in the draft tube (b) as a function of the gauge pressure.

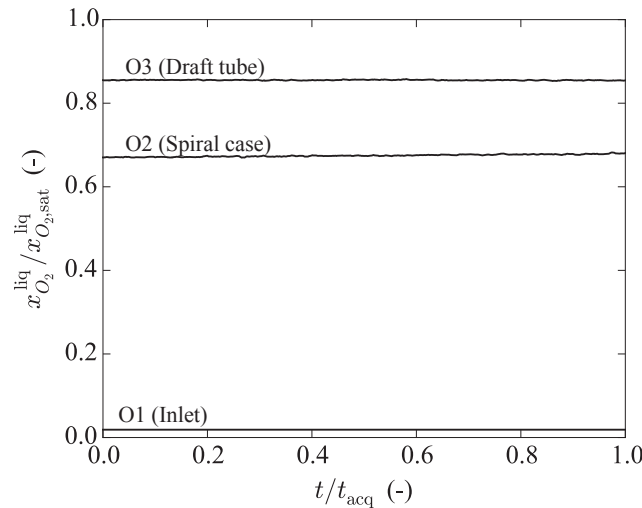


Figure 4.6 – Time solved oxygen concentration divided by the concentration at the saturation condition in the three measurements locations at  $Fr_d = 4$ ,  $p = 10$  bar and  $Q = 40 \text{ l}\cdot\text{h}^{-1}$ .

### 4.5.2 Analytical solution: estimation of the global diffusion coefficients in the vaneless gap and in the cone of the draft tube

The global diffusion coefficients computed by solving the problem illustrated in Sec. 4.4.1 for each  $Fr_d$  value is illustrated in Fig. 4.8 together with the interpolating functions. It is observed that the diffusion coefficient increases by increasing the densimetric Froude number. For  $Fr_d < 4$  the diffusion coefficient has a higher value in the vaneless gap than in the cone while at  $Fr_d = 4$  the value of the coefficient in the cone is higher.

An example of the evolution of the oxygen concentration in time computed by the diffusion equations illustrated in Sec. 4.3 is shown in Fig. 4.9 for  $Fr_d = 2$  and  $Fr_d = 4$ , respectively,

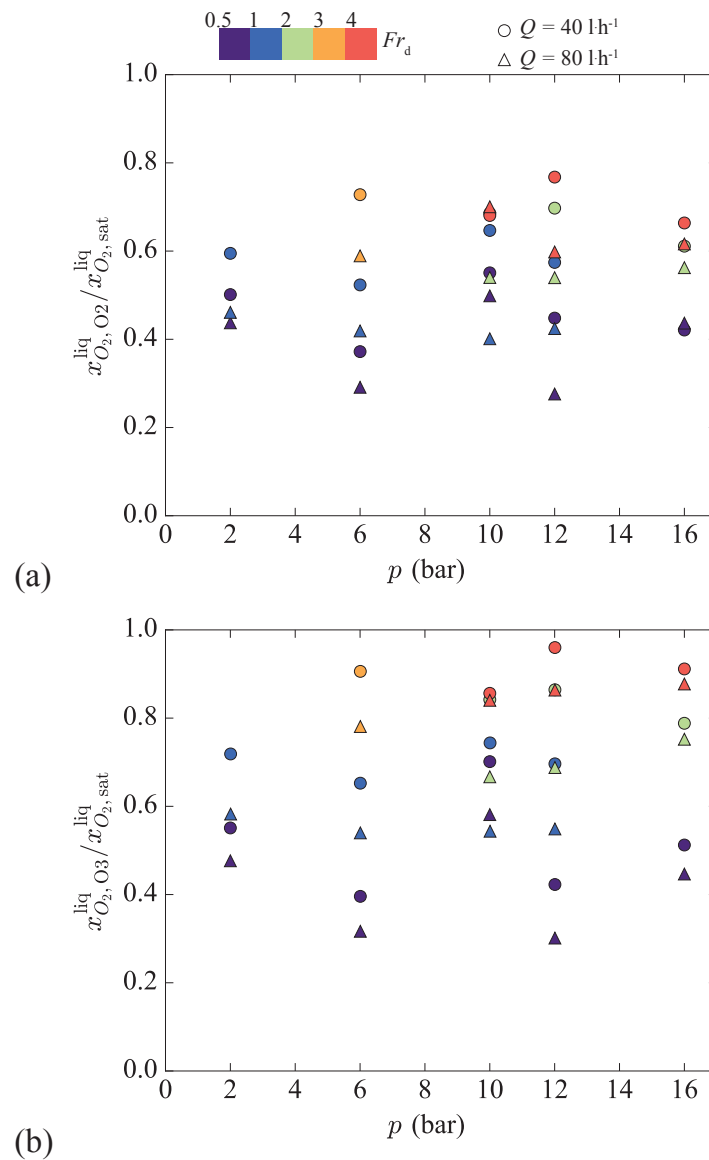


Figure 4.7 – Averaged value of the measured oxygen concentration, divided by the concentration at the saturation condition, in the spiral case (a) and in the draft tube (b) as a function of the gauge pressure.

$p = 16 \text{ bar}$  and  $Q = 80 \text{ l} \cdot \text{h}^{-1}$ . The global diffusion coefficients presented in Fig. 4.8 are employed to compute the evolution in time of the oxygen concentration.

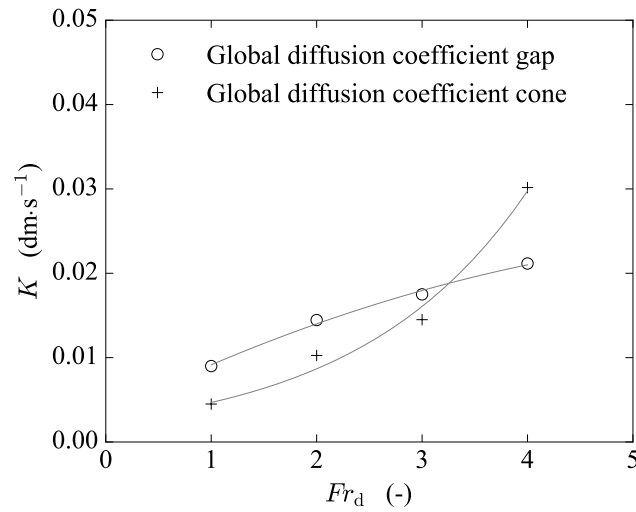


Figure 4.8 – Influence of the densimetric Froude number on the computed diffusion coefficients and interpolating functions.

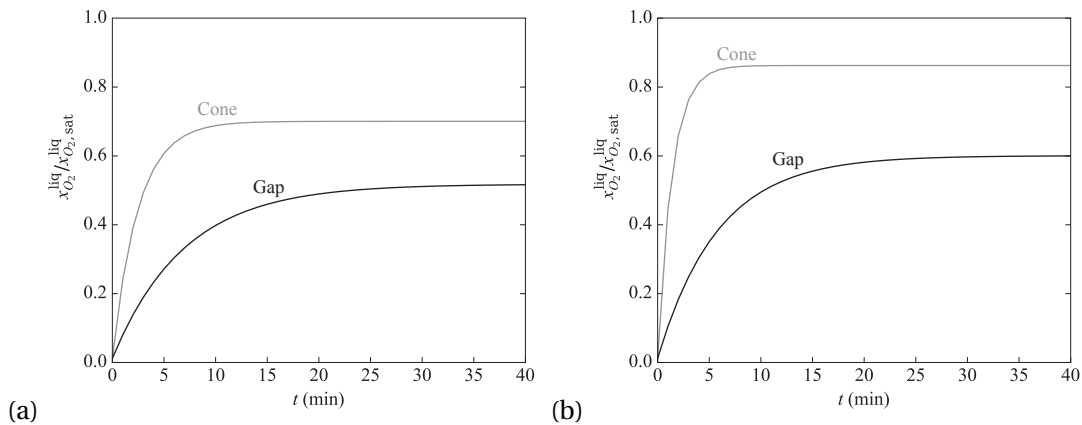


Figure 4.9 – Time history of the oxygen concentration as a result of the theoretical framework developed for  $Fr_d = 2$  (a) and  $Fr_d = 4$  (b),  $p = 16$  bar and  $Q = 80 \text{ l}\cdot\text{h}^{-1}$ .

### 4.5.3 Validation of the theoretical framework with the measurements of the oxygen concentration.

To validate the analytical solution developed in Sec. 4.3, the computed value of the oxygen concentration at the stable condition in both spiral case and draft tube are compared to the measured values at the location O2 and O3, respectively. As can be seen in Fig. 4.10, the experimental data show good agreement with the value computed by the solution of the theoretical framework.

The maximum discrepancy between the measured and the computed oxygen concentration accounts for 12.3 % of the saturation value.



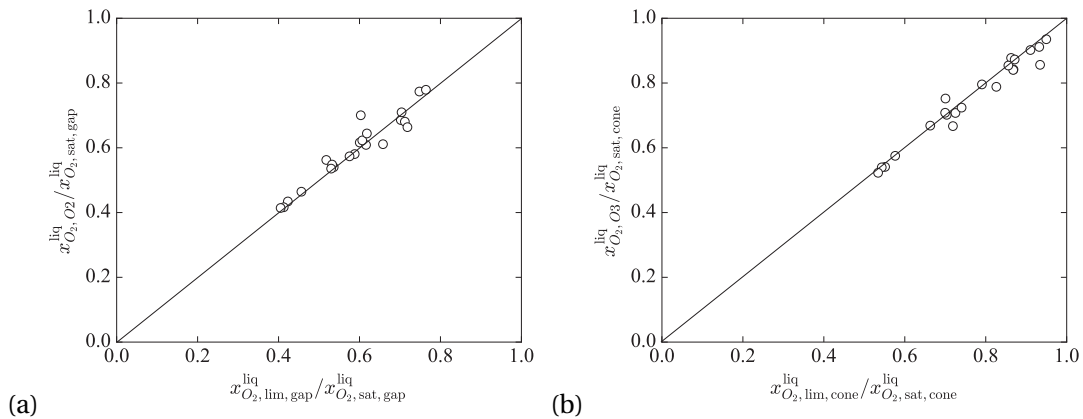


Figure 4.10 – Measured oxygen concentration as a function of the value of the oxygen concentration computed by solving eq. (4.17) at stable condition in the spiral case (a) and in the draft tube (b).

## 4.6 Discussion

### 4.6.1 Influence of the densimetric Froude number on the oxygen concentration

As observed in Fig. 4.7 the densimetric Froude number has a relevant influence on the variation of the oxygen concentration divided by the concentration at the saturation condition in the water volume in both the spiral case and in the draft tube. At higher  $Fr_d$  values an increasing air-water mixing is expected as previously observed by performing high-speed imaging in both vaneless gap and draft tube of the machine [111] and it can explain the increase of the oxygen concentration. The two-phase flow in the vaneless gap at  $Fr_d = 0.5$  is characterized by a bubbly flow and the cooling discharge directly drains in the draft tube cone without passing through the spiral case and the recycling pipe. At  $Fr_d > 0.5$  an air-water mixture is observed in the vaneless gap and the impeller gives a centrifugal force sufficient to push the flow into the spiral case and so through the recycling pipe. This promotes the oxygen mass transfer in water due to the mixing air-water flow. Moreover, the water free-surface in the cone of the draft tube is characterized by a sloshing motion whose amplitude depends on the densimetric Froude number, as observed by [111]. It was previously observed that wave breaking occurs at higher  $Fr_d$  values which further promotes the oxygen diffusion into the water volume.

### 4.6.2 Estimation of the air losses due to the diffusion through the free-surface in the draft tube cone

The measurement of the water level in the cone of the draft tube allows the calculation of the mass flow rate of oxygen diffusing into the water volume according to eq. (4.22). The computed values are validated by the experimental results as illustrated in Fig. 4.11. A fairly good agreement is observed between the measured and the computed values of the mass flow rate.

## Chapter 4. Air diffusion in the liquid volume

---

The mass flow rate of air can be computed according to eq. (4.24) and due to the equivalence of the measured and the computed mass flow rate of oxygen, the air mass flow rate can be rewritten according to eq. (4.25):

$$\dot{m}_{\text{air}} = \frac{p \cdot MM_{\text{air}}}{R \cdot \Theta} \cdot \frac{dV}{dl} \cdot \frac{dl}{dt} \quad (\text{kg} \cdot \text{s}^{-1}) \quad (4.24)$$

$MM_{\text{air}}$  is the air molar mass.

$$\dot{m}_{\text{air}} = \frac{dm_{O_2}}{dt} \cdot \frac{MM_{\text{air}}}{X_{O_2} \cdot MM_{O_2}} = (x_{O_2, O3}^{\text{liq}} - x_{O_2, O1}^{\text{liq}}) \cdot \frac{MM_{\text{air}}}{X_{O_2}} \cdot Q \quad (\text{kg} \cdot \text{s}^{-1}) \quad (4.25)$$

Since the results evidence a fairly good agreement between the measured and the predicted values of the oxygen concentration, the measurement of the oxygen concentrations  $x_{O_2, O3}^{\text{liq}}$  can be replaced by the oxygen concentration at the stable condition  $x_{O_2, \text{lim, cone}}^{\text{liq}}$  computed by solving the theoretical framework illustrated in Sec. 4.3, eq. (4.17)–4.19, and so to predict the air losses as follows:

$$\dot{m}_{\text{air}} = (x_{O_2, \text{lim, cone}}^{\text{liq}} - x_{O_2, 0}^{\text{liq}}) \cdot \frac{MM_{\text{air}}}{X_{O_2}} \cdot Q = f(p, Q, Fr_d) \quad (\text{kg} \cdot \text{s}^{-1}) \quad (4.26)$$

The prediction of the air losses as a function of the densimetric Froude number and of the gauge pressure for the two investigated water cooling discharges is illustrated in Fig. 4.12. It is observed that a higher mass of air is lost by increasing the  $Fr_d$  value and the gauge pressure. It is coherent with the measurements of the oxygen concentration and the model predicting the diffusion of oxygen in the water volume due to the dependency of the oxygen concentration on the saturation condition depending on the gauge pressure and on the global diffusion coefficient depending on the densimetric Froude number. Furthermore, higher air losses are computed by increasing the cooling discharge. The concentration of oxygen in water decreases by increasing the cooling discharge as observed in Fig.4.7 and as predicted by the analytical solution, but, due to the higher discharge exiting the turbine, the air losses are higher.

## 4.7 Conclusion

The performed experimental investigation on the reduced scale physical model of a pump-turbine operating in condenser mode allowed for measurements of the oxygen concentrations, pressure and water level in the draft tube cone. The results showed that the diffusion of oxygen depends on the densimetric Froude number, since the higher the air-water mixing, the higher

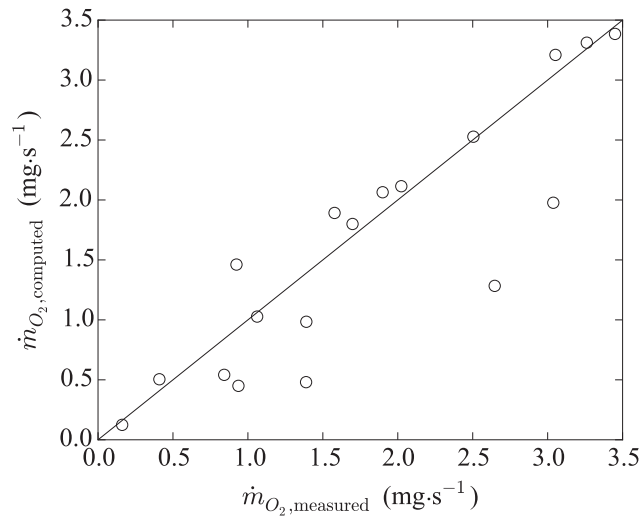


Figure 4.11 – Computed mass flow rate of oxygen by solving eq. (4.22) as a function of the measured value of the oxygen mass flow rate as in eq. (4.23).

is the quantity of oxygen dissolved in water.

An analytical solution of the diffusion equation of oxygen in water is found and applied to the pump-turbine to estimate the global diffusion coefficients of the mass transfer of oxygen in water through the free surfaces in the vaneless gap and in the cone of the draft tube. The global diffusion coefficients were computed as a function of the densimetric Froude number. The higher the densimetric Froude number, the faster is the diffusion of oxygen in water.

The variation of water level in the cone of the draft tube is measured and a theoretical framework on the relationship between the corresponding water volume and air volume variation allows computing the equivalent mass flow rate of oxygen and the mass of air lost. This theoretical solution is validated by the experimental investigation of the oxygen concentration variation between the inlet section and the draft tube cone of the machine.

In light of the presented results, the air losses due to the mass transfer of gases, such oxygen and nitrogen, into water are illustrated and correlated to the operating condition of the machine. The explanation and estimation of the air losses allow controlling the operation in condenser mode of the machine and to developing an optimized start-up of this operating mode for the minimization of the air losses. Furthermore, this might help a further development of the system for the supply of pressurized air and to estimate the power required to compensate the air losses.

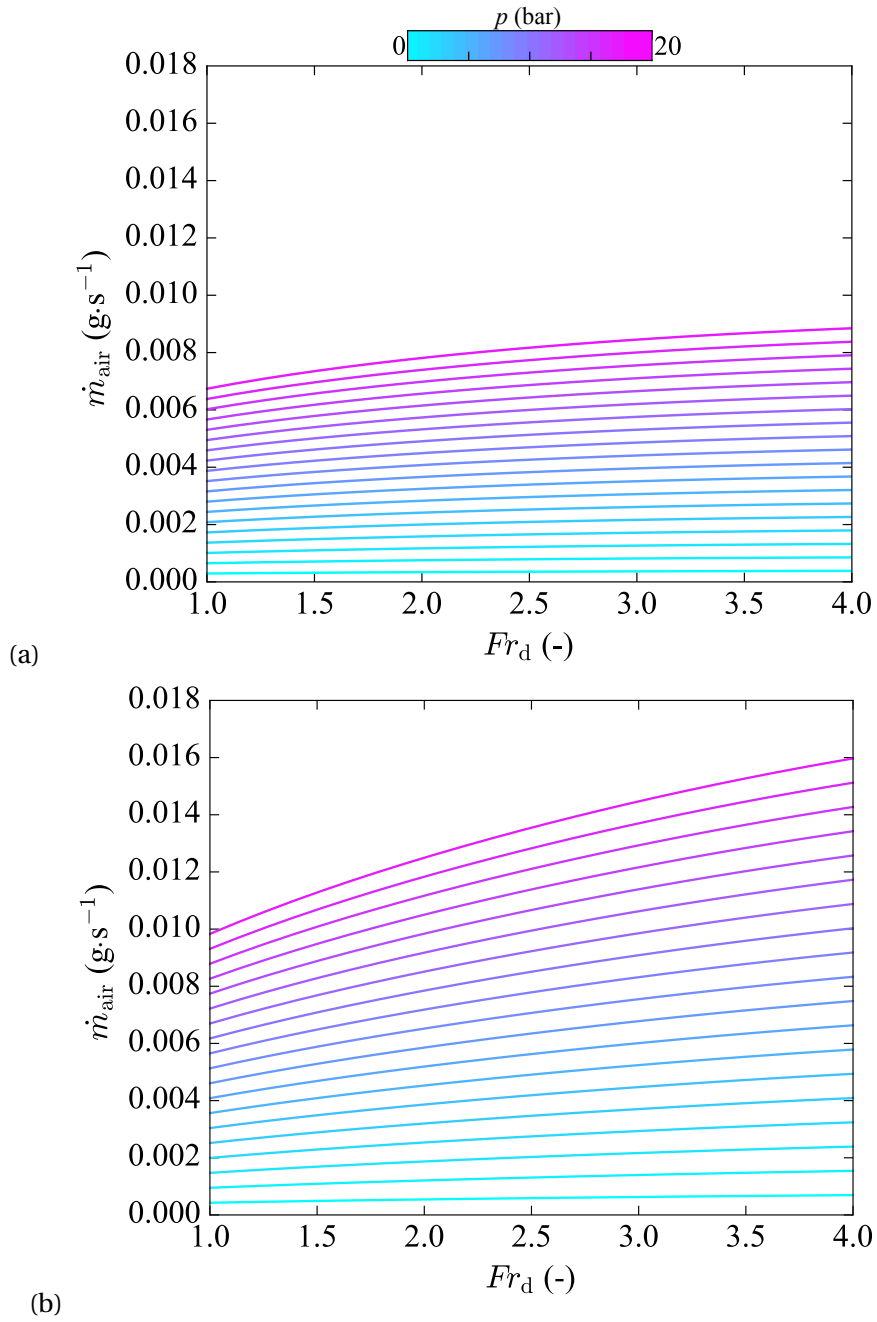


Figure 4.12 – Air losses computed according to eq. (4.26) and iso-pressure line as a function of the densimetric Froude number for  $Q = 40 \text{ l}\cdot\text{h}^{-1}$  (a) and  $Q = 80 \text{ l}\cdot\text{h}^{-1}$  (b).

# 5 Guideline for power consumption calculation

## 5.1 Introduction

In this guideline, a methodology is proposed to compute the power consumption in synchronous condenser mode operation. The power consumption refers to the torque transmitted through the coupling of the runner and the shaft and to the air losses. Other losses are not considered within the scope of this work.

A practical example of the application of this method to a full scale prototype is given.

## 5.2 Methodology

### 5.2.1 Mechanical torque

In chapter 3, a study on the torque and differential pressure coefficient is performed. It is found that these coefficients and the behavior of the flow in machine strongly depend on the densimetric Froude number. Indeed, it is necessary to compute the densimetric Froude number, according to eq. (4.2), to identify the regime (Regime 1,2,3,4) of the flow in machine.

#### Regime 1

For  $Fr_d \leq 0.5$  (Regime 1), a significant influence of the pressure and rotational speed of the impeller on both torque and differential pressure coefficient is observed, as presented in Fig. 3.10. The surrogate model of the differential pressure coefficient as a function of the densimetric Froude number, described in chapter 3, cannot be applied. However, the linearity between the torque and the differential pressure coefficient is respected, as illustrated in Fig. 3.9.

In light of the results achieved in this work, a relation of the torque coefficient and the gauge pressure in the draft tube cone of the machine is proposed to compute the power consumption due to the mechanical torque for  $Fr_d = 0.5$ . A further study should be addressed to verify the

## Chapter 5. Guideline for power consumption calculation

validity of this relation on a broader range of operating parameters and for lower  $Fr_d$  values.

The initial data required are the angular speed of the runner/impeller  $\omega$ , the high pressure diameter of the runner/impeller  $D_e$  and the gauge pressure measured in the draft tube cone  $p$ .

**Step 1:** Calculation of the torque coefficient as a function of the pressure, as illustrated in Fig. 5.1 and as follows:

$$C_T = 0.0025 \cdot C_{\Delta p} = \widetilde{a}_1 + \exp(-\widetilde{b}_1 \cdot p) \quad (-) \quad (5.1)$$

where  $\widetilde{a}_1 = 0.001575$ ,  $\widetilde{b}_1 = 0.00025$  for  $Fr_d = 0.5$ .

**Step 2:** Calculation of the mean mechanical torque of the full scale prototype by respecting the similitude on the torque coefficient:

$$\overline{T}_m = C_T \cdot \rho_{\text{water}} \cdot g \cdot D_e^4 \quad (\text{N} \cdot \text{m}) \quad (5.2)$$

**Step 3:** Calculation of the power consumption:

$$P_T = \omega \cdot \overline{T}_m \quad (\text{W}) \quad (5.3)$$

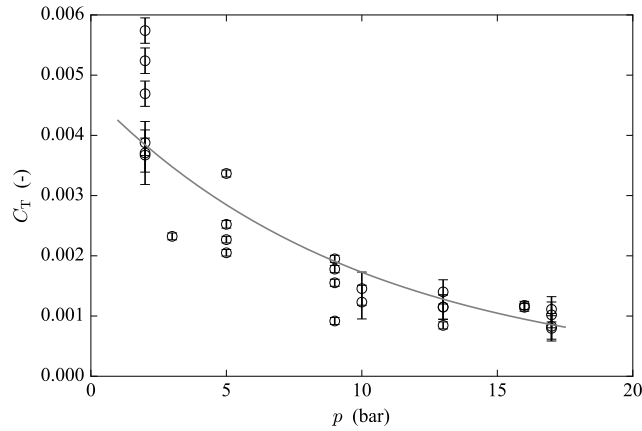


Figure 5.1 – Torque coefficient as a function of the gauge pressure in the draft tube cone and interpolating function for  $Fr_d = 0.5$ .

### Regime 2

As detailed in chapter 3, the torque coefficient significantly fluctuate for  $0.5 < Fr_d \leq 2$  (Regime 2). As shown in Fig. 3.5(b), the torque coefficient fluctuates by increasing 10 times its value in Regime 2, which corresponds to about 700 W fluctuation of the power consumption on the reduced scale model for  $2'000 \text{ min}^{-1}$  rotational speed. On the full scale prototype, significant power swings, up to 20 MW, would be recorded by operating in this regime, oscillations which are dangerous for the mechanical components of the hydraulic unit and for the electric grid

due to the high fluctuation of the active power consumption. Therefore, in light of these results, the operation in Regime 2 should be avoided.

### Regime 3 and 4

For the stable operating condition at  $Fr_d > 2$  (Regimes 3 and 4), the following methodology can be applied to compute the power consumption due to the mechanical torque. The initial data required are the angular speed of the runner/impeller  $\omega$ , the high pressure diameter of the runner/impeller  $D_e$  and the gauge pressure measured in the draft tube cone  $p$ .

**Step 1:** Calculation of the torque coefficient depending on the densimetric Froude number. The torque coefficient can be predicted by using the surrogate model of the differential pressure coefficient in eq. (3.10), and the linearity between the differential pressure coefficient and the torque coefficient presented in Fig. 3.9, as follows:

$$C_T = 0.0025 \cdot C_{\Delta p} = \tilde{a} + \tilde{b} \cdot Fr_d + \tilde{c} \cdot Fr_d^2 \quad (-) \quad (5.4)$$

where  $\tilde{a} = 0$ ,  $\tilde{b} = 0.000125$ ,  $\tilde{c} = 0.0003$  for  $Fr_d < 4.5$  and  $\tilde{a} = 0.0076$ ,  $\tilde{b} = -0.00255$ ,  $\tilde{c} = 0.000575$  for  $Fr_d \geq 4.5$ . The densimetric Froude number is computed according to eq. (4.2).

**Step 2:** Calculation of the mean mechanical torque of the full scale prototype by respecting the similitude on the torque coefficient:

$$\overline{T}_m = C_T \cdot \rho_{\text{water}} \cdot g \cdot D_e^4 \quad (\text{N} \cdot \text{m}) \quad (5.5)$$

**Step 3:** Calculation of the power consumption:

$$P_T = \omega \cdot \overline{T}_m \quad (\text{W}) \quad (5.6)$$

### 5.2.2 Air losses

In chapter 4, an analytical model predicting the air losses due to air diffusion is proposed. Here follows a general methodology to compute the power consumption required to compensate these losses by injecting compressed air in the draft tube. This allows correctly designing the air compressor. The initial data required are the water cooling discharge  $Q$ , the inlet oxygen concentration  $x_{O_2,0}^{\text{liq}}$ , the high pressure radius of the runner/impeller  $R_e$ , the diameter of the draft tube cone at quiescent water level  $D$ , the vaneless gap height  $h_{\text{gap}}$ , the pressure  $p$ , the temperature  $\Theta$  and the angular speed of the runner/impeller  $\omega$ .

**Step 1:** Compute the geometrical area of the free-surface in the draft tube cone and in the vaneless gap:

$$A_{\text{gap}} = 2 \cdot \pi \cdot R_e \cdot h_{\text{gap}} \quad A_{\text{cone}} = \pi \cdot (D/2)^2 \quad (5.7)$$

## Chapter 5. Guideline for power consumption calculation

**Step 2:** Compute the concentration at the saturation condition  $x_{O_2,sat}^{liq}$  as follows in eq. (4.4) depending on the pressure and temperature in the draft tube cone.

**Step 3:** Compute the global diffusion coefficient for the free-surface in the vaneless gap  $K_{gap}$  and in the cone  $K_{cone}$  by using the graph in Fig. 4.8. The densimetric Froude number is computed according to eq. (4.2).

**Step 4:** Compute the oxygen discharge passing through the recycling pipe:

$$Q_{rec} = Q \cdot x_{O_2,lim,gap}^{liq} = Q \cdot \left( \frac{1}{1 + Q/(A_{gap}K_{gap})} x_{O_2,sat}^{liq} + \frac{Q \cdot x_{O_2,0}^{liq}}{A_{gap}K_{gap}(1 + Q/(A_{gap}K_{gap}))} \right) \quad (5.8)$$

**Step 5:** Compute the air mass flow rate lost:

$$\dot{m}_{air} = \left( \frac{1}{1 + Q/(A_{cone}K_{cone})} x_{O_2,sat}^{liq} + \frac{Q_{rec}}{A_{cone}K_{cone}(1 + Q/(A_{cone}K_{cone}))} - x_{O_2,0}^{liq} \right) Q \cdot \frac{MM_{air}}{X_{O_2}} \quad (5.9)$$

**Step 6:** Compute the power consumption to compensate the air losses for an adiabatic compression:

$$P_{air} = \dot{m}_{air} \cdot R_{air} \cdot \Theta \cdot \left( \frac{\gamma}{\gamma - 1} \right) \cdot ((p/p_0)^{(\gamma-1)/\gamma} - 1) \quad (W) \quad (5.10)$$

where  $p_0$  is atmospheric pressure,  $\gamma = 1.4$  is the adiabatic index of air, and  $R_{air} = 287 \text{ J} \cdot (\text{kg} \cdot \text{K})^{-1}$ .

### 5.3 Example

Let's consider a full size prototype with an hydraulic turbine featuring a 4.182 m high pressure diameter, a 0.232 m high vaneless gap and a 2.62 m diameter of the draft tube cone. The submergence level is 60 m and the runner rotates at  $500 \text{ min}^{-1}$ . A  $40 \text{ l} \cdot \text{s}^{-1}$  water discharge is injected for cooling purpose through the labyrinth seals with an initial oxygen concentration  $x_{O_2,0}^{liq} = 2 \text{ ppm}$  at  $\Theta = 289 \text{ K}$ . At this operating condition, the densimetric Froude number is  $Fr_d = 3.42$ .

#### Power consumption due to the mechanical torque

According to eq. (5.4), the torque coefficient computed for  $Fr_d = 3.42$  is  $C_T = 0.005$ . Indeed, according to eq. (5.5) the average mechanical torque is  $\bar{T}_m = 15 \text{ kN} \cdot \text{m}$ . It follows a power consumption  $P_T = 0.8 \text{ MW}$ .

#### Power consumption due to keeping-up air

By following the procedure described in Sec. 5.2, first of all the geometrical area of the vaneless gap and the draft tube cone are computed:  $A_{gap} = 3.31 \text{ m}^2$  and  $A_{cone} = 3.24 \text{ m}^2$ . Secondly, the



concentration is computed:  $x_{O_2, \text{sat}}^{\text{liq}} = 72.8$  ppm and third, the global diffusion coefficients are found:  $K_{\text{gap}} = 0.02$  and  $K_{\text{cone}} = 0.023$ .

The oxygen discharge passing through the recycling pipe is then computed according to eq. (5.8):  $Q_{\text{rec}} = 0.014 \text{ mol} \cdot \text{s}^{-1}$ .

Finally, the computed air losses are  $\dot{m}_{\text{air}} = 0.004 \text{ kg} \cdot \text{s}^{-1}$ , which correspond to a power consumption  $P_{\text{air}} = 865 \text{ W}$ . In Fig. 5.2 are illustrated the power losses related to the keeping-up of compressed air for the prototype taken as example by varying the gauge pressure and the densimetric Froude number.

The power consumption is mainly due to the torque transmitted through the coupling of the runner and the shaft. Therefore, the torque value is still significant due to the friction losses of the fluid-structure interaction in the vaneless gap between the blades of the impeller and the closed guide vanes. Furthermore, it is important to compute the air losses and the related power budget for a proper design of the pressurization system for air supply.

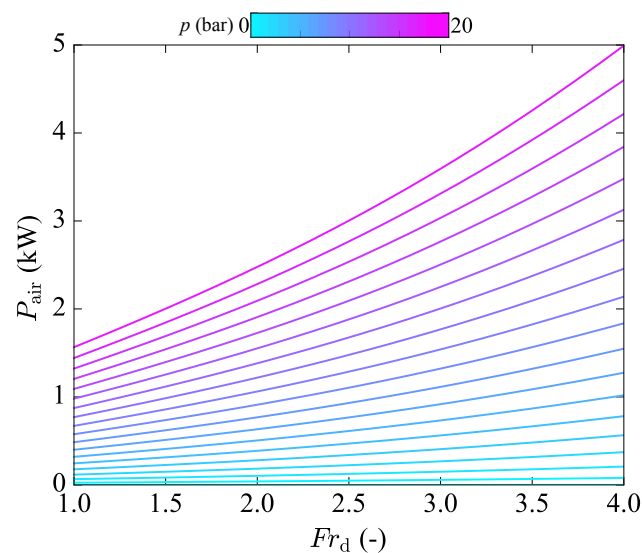


Figure 5.2 – Power consumption due to air losses on iso-pressure lines as a function of the densimetric Froude number.



# Conclusion and perspectives

## Conclusion

Francis-type hydraulic turbines and pump-turbines operating in synchronous condenser mode record significant torque values transmitted to the shaft and air losses, but the origin and the mechanism causing these problems for the machine operation is unclear to date. Here come the need and motivation of performing new investigations to elucidate the flow phenomena in the machine and to tackle the problems of power consumption and the proper design of the air compressor.

In this thesis, the main two-phase flow phenomena occurring in a Francis-type hydraulic turbine or pump-turbine operating in synchronous condenser mode and their influence on the power consumption were investigated. First, these phenomena, namely the sloshing motion of the free-surface in the draft tube cone and the rotating air-water ring in the vaneless gap, were measured to provide a detailed characterization of their behavior for various operating conditions of the machine. Then, the mechanical torque transmitted through the coupling of the runner and the shaft and the air losses due to the mass transfer in the water volume were investigated, and a theoretical framework was established to understand and predict the stability of the operating mode and the energy consumption.

In **chapter 1**, the dynamic characteristics of the sloshing motion of the free-surface were studied. Image acquisition and pressure fluctuations measurements were performed and an image processing method was developed to define the amplitude and frequency of the sloshing motion for various operating conditions of the machine. It was found that the sloshing motion is a resonance phenomenon of the water volume dominated by an azimuthal wavenumber  $m = 1$ . The amplitude of the sloshing depends on the densimetric Froude number. It decreases for higher  $Fr_d$  values because of wave breaking on the free-surface. The frequency variation is likely due to the variation of the turbulence level of the air flow on the water free-surface which depends on the rotational speed of the runner. A complementary experiment by employing a commercial axial fan blowing in a closed cylinder partially filled with water was carried out to further investigate the onset of the sloshing motion of a water volume by the forcing of an air flow. This study confirmed the observation done in the draft tube cone of the turbine in condenser mode and back up the interest of further pursuing fundamental research on this phenomenon to explain the development of the gravity wave excited by a turbulent air flow

above.

In **chapter 2**, the rotating air-water ring in the vaneless gap was investigated for a densimetric Froude number  $Fr_d = 0.5$ . High-speed visualization and pressure measurements were performed to evidence the formation of the air-water ring characterized by a bubbly flow. The size and the velocity field of the bubbles were estimated as a function of the operating parameters of the machine through image processing for the bubble detection and tracking position in the rotating air-water ring. Bubbles size increases for higher pressure causing the decrease of the flow velocity due to the formation of clusters of bubbles. Pressure fluctuation measurements showed a dominant oscillation at  $f/f_b = 0.7$ . A theoretical framework on the harmonic components established the development of diametrical modes of the pressure fields due to the interactions of the rotating and stationary component of the machine, namely the impeller blades and the closed guide vanes, with the rotating air-water ring.

In light of the results achieved in the experimental investigation of the main two-phase flow phenomena occurring in a turbine operating in condenser mode, a detailed study on the interaction of these phenomena and the power consumption of the turbine was carried out. In particular, the perturbation of the resistant mechanical torque and differential pressure caused by the interaction of the impeller blades and the flow structures in the air-water ring was presented in **chapter 3**. A study on the variation of the flow structures in the vaneless gap was performed. High-speed visualization together with measurements of mechanical torque and pressure evidenced the flow structures characterizing the air-water ring for various densimetric Froude number. The flow in the vaneless gap was qualitatively divided into four visually distinct regimes: bubbly flow, periodic flow shrinking, capillary waves and thick air-water mixture. A study on the correlation between the measurements performed for several operating conditions of the machine allowed for the understanding of the impact of the flow regimes on the machine stability and the development of an empirical model predicting the differential pressure coefficient as a function of the operating parameters.

In **chapter 4**, a theoretical framework on the air mass transfer in the water volume of the turbine was developed and empirically validated. To study the oxygen diffusion in the two-phase flows described in chapters 1 and 2, oxygen concentration measurements were performed in the spiral case and in the draft tube of the machine. The validation of the analytical model of the oxygen mass transfer with the experimental measurements allowed computing the global diffusion coefficients in the vaneless gap and in the draft tube cone as a function of the densimetric Froude number. A fairly good agreement is observed between the measurements of air losses and the values predicted by the model. Indeed, the prediction of the air losses due to air diffusion depending on the operating condition of the machine is achieved.

Finally in **chapter 5**, a guideline is proposed to compute the power consumption related to the mechanical torque and to the air losses due to air diffusion. This study shows that the power consumption due to the investigated phenomena is significant on a full-scale prototype operating in synchronous condenser mode, reaching 1-3 MW depending on the operating

conditions.

Synchronous condenser mode has been previously studied in literature but, because of the unusual configuration of the turbine, it has been hard to extensively investigate the flow phenomena and their influence on the power consumption. The results achieved in this thesis contribute to the understanding of the flow behavior in turbines and pump-turbines operating in synchronous condenser mode. In particular, the study shows evidence of the four regimes governing the hydrodynamics of the air-water ring and the dynamics of the sloshing motion in the draft tube. Furthermore, this work contributes to understand the fluid-structure interactions causing the increase of the mechanical torque and its instability, and the mechanism causing air losses to finally predict the proper power budget.

The transposition of the results achieved on the reduced scaled physical model to the full scale prototype resulted successful and effective for several hydro power plants by allowing the reduction of the power consumption and the correct design of the pressurizing system.

The results achieved in this thesis allowed filing a patent about the start-up design and procedure to operate the hydro turbine or pump turbine in synchronous condenser mode by controlling and reducing the pressure and power swings [51].

### Perspectives

The presented work leaves room for further investigations which can be grouped in five main lines of research.

The theoretical framework on the air mass transfer and the empirical model predicting the power consumption have been validated for extensive values of densimetric Froude number and operating conditions of the machine but there are still unexplored operating ranges. It would be interesting to perform further measurements to validate and eventually extend this study by exploring the remaining regions of operation, in particular for  $Fr_d \leq 0.5$ . It would be also of interest to expand both works to other turbine geometries to further verify the accuracy of the similarity law adopted for scaling the investigated two-phase flow phenomena from the reduced scale model to the full scale prototype.

Additional investigations of the sloshing motion of the free-surface in the draft tube can be performed to deeply study the evolution of the free-surface and of the above air wind whirl. New optical tools should be adopted to determine the velocity fields of the air flow. Moreover, it would be interesting to measure or compute by numerical simulation the velocity profile of the water volume before the onset of the sloshing motion. This can lead to a further study on the stability of the flow which could explain the development of the rotating wave. These studies would give an important contribution to understand the physics governing the non-linear sloshing of the free-surface excited by a wind whirl.

The Regime 2 of the flow in the vaneless gap presents instability whose dynamics should be further investigated to fully understand the mechanism causing the onset of the oscillation. Instability analysis can be performed on this flow to clarify the driving phenomenon causing this fluctuation.

A complementary study on the air-water ring could be carried out. The flow regimes 3 and 4 were only qualitatively investigated and they should be more extensively studied by providing their pressure and velocity fields. Due to the high void fraction characterizing the flow of both regions, a new experimental tool should be developed to increase measurements accuracy. Furthermore, numerical simulation of the rotor-stator interactions and the air water ring in Regime 1, as described in chapter 2, could be performed to confirm the experimental and analytical results.

Finally, other minor two-phase flow phenomena were observed in the turbine operating in condenser mode, such as the impingement of droplets on the free-surface or their suction by the runner described by Tanaka [100]. A study of those phenomena should be conducted to complete the description of the flow phenomena occurring during the condenser mode operation and to evaluate their impact on the power and air budget.

# Bibliography

- [1] Synchronous condenser systems. *General Electric - Digital Energy*, 2003.
- [2] The blackout of 2003: The overview. <http://www.nytimes.com/2003/08/15/nyregion/blackout-2003-overview-power-surge-blacks-northeast-hitting-cities-8-states.html>, 2003.
- [3] *JCGM 101:2008 — Evaluation of measurement data – Supplement 1 to the "Guide to the expression of the uncertainty in measurement – Propagation of distributions using a Monte Carlo method"*. BIPM, 2008. Sèvres, France.
- [4] Europe 2020 strategy. <https://ec.europa.eu/info/business-economy-euro/economic-and-fiscal-policy-coordination>, 2015.
- [5] Ren21. 2017. renewables 2017 global status report. (*Paris: REN21 Secretariat*), ISBN 978-3-9818107-6-9, 2016.
- [6] Statistics of hydroelectric installations in switzerland. <http://www.bfe.admin.ch/themen/00490/00491/?lang=en>, 2016.
- [7] V. Aeschlimann, S. Barre, and S. Legoupil. X-ray attenuation measurements in a cavitating mixing layer for instantaneous two-dimensional void ratio determination. *Physics of Fluids*, 23(5):055101, 2011.
- [8] H. Akyildiz and N. Unal. Sloshing in a three-dimensional rectangular tank: numerical simulation and experimental validation. *Ocean Engineering*, 33(16):2135–2149, 2006.
- [9] D. B. Allan, T. A. Caswell, and N. C. Keim. Trackpy v0.2. 2014.
- [10] S. Alligné, C. Nicolet, c. RUchonnet, V. Hasmatuchi, P. Maruzewski, and F. Avellan. Numerical simulation of non-linear self oscillations of a full load vortex rope. *Proceedings of the 3rd Meeting of the IAHR Workgroup in Cavitation and Dynamic Problem in hydraulic Machinery and System*, 2, Brno, Czech Republic:325–338, 2009.
- [11] L. Andolfatto. *Assistance à l'élaboration de gammes d'assemblage innovantes de structures composites*. PhD thesis, École Normale Supérieure de Cachan, France, 2013.

## Bibliography

---

- [12] F. Aureli, A. Maranzoni, P. Mignosa, and C. Ziveri. An image processing technique for measuring free surface of dam-break flows. *Experiments in Fluids*, 50:665–675, 2011.
- [13] M. A. Ayoubi, F. A. Goodarzi, and A. Banerjee. Attitude motion of a spinning spacecraft with fuel sloshing and nutation damping. *The Journal of the Astronautical Sciences*, 58(4):551–568, Oct 2011.
- [14] R. Battino and H. L. Clever. The solubility of gases in liquids. *Chemical Reviews*, 66(4):395–463, 1966.
- [15] R. Battino, T. R. Rettich, and T. Tominaga. The solubility of nitrogen and air in liquids. 13:563–600, 04 1984.
- [16] J. Bendat and A. Piersol. *Random Data: Analysis and Measurement Procedure*. 4th ed., Wiley, Hoboken, NJ, 2010.
- [17] U. Bolleter. Blade passage tones of centrifugal pump. *Vibrations*, 4(3):8–13, 1988.
- [18] G. Bradski and A. Kaehler. *Learning OpenCV*. O'Reilly Media, 2008.
- [19] W. J. Braida and S. K. Ong. Air sparging: Air-water mass transfer coefficients. *Water Resources Research*, 34(12):3245–3253, 1998.
- [20] D. Braisted and C. Brennen. Observations on instabilities of cavitating inducers. *Joint Symposium on the Design and Operation of Fluid Machinery American Society of Mechanical Engineers New York USA*, pages 9–22, 1978.
- [21] D. Broder and M. Sommerfeld. An advanced lif-plv system for analyzing the hydrodynamics in a laboratory bubble column at higher void fractions. *Experiments in Fluids*, 33:826–837, 2002.
- [22] D. Broder and M. Sommerfeld. Planar shadow image velocimetry for the analysis of the hydrodynamics in bubbly flows. *Measurement science and technology*, 18:2513–2528, 2007.
- [23] T. Carlson. The diffusion of oxygen in water. *Journal of the American Chemical Society*, 33(7):1027–1032, 1911.
- [24] O. Ceravola, M. Fanelli, and B. Lazzaro. The behaviour of the free level below the runner of francis turbine and pump-turbines in operation as synchronous condenser. *proceedings of the 10th LAHR-SHMEC Symposium, Tokyo, Japan*, 1:765–775, 1980.
- [25] H. Chanson. Air bubble entrainment in free-surface turbulent flows. *Report CH46/95, Department of Civil Engineering, The University of Queensland, Australia*, 1995.
- [26] H. Chanson and F. Murzyn. Froude similitude and scale effects affecting air entrainment in hydraulic jumps. *Proceedings of World Environmental and Water Resources Congress, Ahupua, USA*, 2008.



- [27] H. Chanson and L. Toombes. Strong interactions between free-surface aeration and turbulence in an open channel flow. *Experimental Thermal and Fluid Science*, 27:525–535, 2003.
- [28] D. Cheng and H. Burkhardt. Template based bubble identification and tracking in image sequences. *International Journal of Thermal Science*, 45:321–330, 2006.
- [29] S. Cochard and C. Ancey. Tracking the free surface of time-dependent flows: image processing for the dam-break problem. *Experiments in Fluids*, 44:59–71, 2008.
- [30] J. J. Cole, D. L. Bade, D. Bastviken, M. L. Pace, and M. Van de Bogert. Multiple approaches to estimating air-water gas exchange in small lakes. *Limnology and Oceanography: Methods*, 8(6):285–293, 2010.
- [31] D. Colombet, D. Legendre, A. Cockx, P. Guiraudand, F. Risso, C. Daniel, and S. Galinat. Experimental study of mass transfer in a dense bubble swarm. *Chemical Engineering Science*, 66:3432–3440, 2011.
- [32] P. Cummings and H. Chanson. Air entrainment in the developing flow region of plunging jets-part1 theoretical development. *Journal of Fluids Engineering*, 119:597–602, 1997.
- [33] P. Cummings and H. Chanson. Air entrainment in the developing flow region of plunging jets-part2 experimental. *Journal of Fluids Engineering*, 119:603–608, 1997.
- [34] A. Dazin, G. Cavazzini, G. Pavesi, P. Dupont, S. Coudert, G. Ardizzon, G. Caignaert, and G. Bois. High-speed stereoscopic piv study of rotating instabilities in a radial vaneless diffuser. *Experiments in Fluids*, 51(1):83–93, Jul 2011.
- [35] S. Dixon and C. Hall. Butterworth-Heinemann, Boston, seventh edition edition, 2014.
- [36] M. Eswaran and U. Saha. Sloshing of liquids in partially filled tanks – a review of experimental investigations. *Ocean Systems Engineering*, 1(2):131–155, 2011.
- [37] M. Farid and O. Gendelman. Response regimes in equivalent mechanical model of strongly nonlinear liquid sloshing. *International Journal of Non-Linear Mechanics*, 2016.
- [38] M. Farid and O. Gendelman. Response regimes in equivalent mechanical model of moderately nonlinear liquid sloshing. *ARXIV*, 2017.
- [39] A. Favrel. *Dynamics of the cavitation precessing vortex rope for francis turbines at part load operating conditions*. PhD thesis, EPFL, 2016.
- [40] A. Favrel, A. Müller, C. Landry, K. Yamamoto, and F. Avellan. Ldv survey of cavitation and resonance effect on the precessing vortex rope dynamics in the draft tube of francis turbines. *Experiments in Fluids*, 57:168, 2016.
- [41] A. Ferreira, G. Pereira, J. Teixeira, and F. Roch. Statistical tool combined with image analysis to characterize hydrodynamics and mass transfer in a bubble column. *Chemical Engineering Journal*, 180:216–228, 2012.

## Bibliography

---

- [42] R. T. Ferrell and D. M. Himmelblau. Diffusion coefficients of nitrogen and oxygen in water. *Journal of Chemical & Engineering Data*, 12(1):111–115, 1967.
- [43] A. Fick. Ueber diffusion. *Annalen der Physik*, 170(1):59–86, 1855.
- [44] J. Friedman. Multivariate adaptive regression splines. *The annals of statistics*, 19(1):1–67, 1991.
- [45] Y. Fu and Y. Liu. Development of a robust image processing technique for bubbly ow measurement in a narrow rectangular channel. *International Journal of Multiphase Flow*, 84:217–228, 2016.
- [46] C. Gabillet, C. Colin, and J. Fabre. Experimental study of bubble injection in a turbulent boundary layer. *International Journal of Multiphase Flow*, 28:553–578, 2002.
- [47] I. P. Gavriluk, I. A. Lukovsky, and A. N. Timokha. Linear and nonlinear sloshing in a circular conical tank. *Fluid Dynamics Research*, 37-6, 2005.
- [48] R. Gonzales and R. Woods. *Digital image processing*. Pearson Education International, 2008.
- [49] G. Rossi and V. Zanetti. Starting in air and synchronous condenser operation of pump-turbines - model research. *Proceedings of the 9th IAHR-SHMEC Symposium, Fort Collins, USA*, 2:337–352, 1978.
- [50] I. G. Rychkov. Reactive power control services based on a generator operating as a synchronous condenser. *Power Technology and Engineering*, 46:405–409, 2013.
- [51] R. Guillaume, P. Y. Lowys, A. Legrand, and P. Girin. Hydraulic installation operating in condenser mode. <https://patentscope.wipo.int/search/en/detail.jsf?docId=WO2017046012>, 2017. Patent WO/2017/046012, IPC F03B 11/00 3/02 (2006.01).
- [52] Y. Hassan. Full-field measurements of turbulent bubbly flow using innovative experimental techniques. *Milestone for Consortium for Advance Simulation of LWRs, US department of Energy*, 2014.
- [53] Y. Hassan, T.K., Blanchat, C. Seeley, and R. Canaan. Simultaneous velocity measurements of both components of a two-phase flow using particle image velocimetry. *International Journal of Multiphase Flow*, 18:371–395, 1992.
- [54] W. Henry. Experiments on the quantity of gases absorbed by water, at different temperatures, and under different pressures. *Phil. Trans. R. Soc. Lond.*, 93:29–274, (1803).
- [55] M. Honkanen, D. Elcock, C. Kuo, Y. Peles, and M. Amitay. Lagrangian tracking of bubbles interacting with pin-fins in a microchannel. *Experiments in Fluids*, 50:1527–1538, 2011.
- [56] B. Hu, M. Langsholt, L. Liu, P. Andersson, and C. Lawrence. Flow structure and phase distribution in stratified and slug flows measured by x-ray tomography. *International Journal of Multiphase Flow*, 67:162 – 179, 2014.

- [57] R. A. Ibrahim. *Liquid Sloshing Dynamics: Theory and Applications*. Cambridge University Press, 2005.
- [58] S. Iliescu and F. Avellan. *Analysis Of Large Scale Hydrodynamic phenomena In Turbine Draft Tubes*. PhD thesis, EPFL, 2007.
- [59] S. Iliescu, G. Ciocan, and F. Avellan. Analysis of the cavitating draft tube vortex in a francis turbine using particle image velocimetry in two phase flow,. *Journal of Fluids Engineering*, 130, 2008.
- [60] Y. Ito, K. Nagata, Y. Sakai, and O. Terashima. Momentum and mass transfer in developing liquid shear mixing layers. *Experimental Thermal and Fluid Science*, 51:28–36, 2013.
- [61] I. Jansson, H. Akerstedt, J.-O. Aidanpää, and T. Lundström. The effect of inertia and angular momentum of a fluid annulus on lateral transversal rotor vibrations. *Journal of Fluids and Structure*, 28:328–342, 2012.
- [62] J.H.Jung, S. Yoon, and C. Lee. Effect of natural frequency modes on sloshing phenomenon in a rectangular tank. *International Journal of Naval Architecture and Ocean Engineering*, 7(3):580–594, 2015.
- [63] E. Jones, T. Oliphant, P. Peterson, et al. SciPy: Open source scientific tools for Python. <http://www.scipy.org>, 2001.
- [64] D. Kang, K. Yonezawa, H. Horiguchi, Y. Kawata, Y., and Tsujimoto. Cause of cavitation instabilities in three-dimensional inducer. *International Symposium on Cavitation, Ann Arbor, MI, USA*, pages 1–8, 2009.
- [65] S. Khodaparast, N. Borhani, and J. Thome. Application of micro particle shadow velocimetry mpsv to two-phase flows in microchannels. *International Journal of Multiphase Flow*, 62:123–133, 2014.
- [66] Y.-N. Kim, J. Kim, G. Park, and H. CHo. Measurement of sliding bubble behavior on a horizontal heated tube using a stereoscopic image processing technique. *International Journal of Multiphase Flow*, 94:156–172, 2017.
- [67] D. King, W. J De Bryun, M. Zheng, and E. S Saltzman. Uncertainties in the molecular diffusion coefficient of gases in water for use in the estimation of air-sea exchange. *Air-Water Gas Transfer*, 01 1995.
- [68] S. S. Kolukula and P. Chellapandi. Nonlinear finite element analysis of sloshing. *Advances in Numerical Analysis*, 2013:1–10, 2013.
- [69] S. Komori, R. Nagaosa, and Y. Murakami. Turbulence structure and mass transfer across a sheared air-water interface in wind-driven turbulence. *Journal of Fluid Mechanics*, 249:161–183, 1993.
- [70] H. Lamb. *Hydrodynamics*. Dover, New York, 1945.

## Bibliography

---

- [71] A. Lamotte, A. Delafosse, S. Calvo, F. Delvigne, and D. Toye. Investigating the effects of hydrodynamics and mixing on mass transfer through the free-surface in stirred tank bioreactors. *Chemical Engineering Science*, 172:125–142, 2017.
- [72] E. T. LAYTON. *From rule of thumb to scientific engineering: James B. Francis and the invention of the Francis Turbine*. Stony Brook, N.Y., State University of New York. Research Foundation, 1992.
- [73] E. Lerner. What’s wrong with the electric grid? *Physics Today*, 2014.
- [74] R. Lindken and W. Merzkirch. A novel piv technique for measurements in multiphase flows and its application to two-phase bubbly flows. *Experiments in Fluids*, 33:814–825, 2002.
- [75] R. L. Miorini, H. Wu, and J. Katz. The internal structure of the tip leakage vortex within the rotor of an axial waterjet pump. *J. Turbomachines*, 134(3) ,031018, 2011.
- [76] N. Mujica and D. P. Lathrop. Hysteretic gravity-wave bifurcation in a highly turbulent swirling flow. *Journal of Fluid Mechanics*, 551:49–62, 2006.
- [77] A. Müller. *Physical mechanisms governing self-excited pressure oscillations in francis turbines*. PhD thesis, EPFL, 2014.
- [78] A. Müller, M. Dreyer, N. Andreini, and F. Avellan. Draft tube discharge fluctuations during self-sustained pressure surge: fluorescent particle image velocimetry in two-phase flow. *Experiments in Fluids*, 54 issue 4:1–11, 2013.
- [79] A. Müller, A. Favrel, C. Landry, and F. Avellan. Fluid-structure interaction mechanism leading to dangerous power swing in francis turbine at full load. *Journal of Fluids and Structure*, 69:56–71, 2016.
- [80] A. Müller, K. Yamamoto, S. Allignè, K. Yonezawa, Y. Tsujimoto, and F. Avellan. Measurement of the self-oscillating vortex rope dynamics for hydroacoustic stability analysis. *Journal of Fluids Engineering*, 138:0212061–8, 2016.
- [81] C. Münch, P. Ausoni, O. Braun, M. Farhat, and F. Avellan. Fluid-structure coupling for an oscillating hydrofoil. *Journal of Fluids and Structure*, 26:1018–1033, 2010.
- [82] A. Nair, N. Pandey, K. Bodke, and M. Laghate. Implementation on analyzing the bubble flows in microchannels using image processing. *Advance Research in Computer Engineering and Technology*, 4,3:802–808, 2015.
- [83] G. M. Odell and L. S. G. Kovaszny. A new type of water channel with density stratification. *Journal of Fluid Mechanics*, 50(3):535–543, 1971.
- [84] P. Painmanakul, J. Wachirasak, M. Jamnongwong, and G. Hebrard. Theoretical prediction of volumetric mass transfer coefficient for designing an aeration tank. *Engineering Journal (Eng. J.)*, 13(3):13–28, Sep. 2009.

- [85] S. Pasche. *Dynamics and optimal control of self-sustained instabilities in laminar and turbulent swirling flows: application to the part load vortex rope in Francis turbine*. PhD thesis, EPFL, 2018.
- [86] J. Pei, H. Dohmen, S. Yuan, and F-K. Benra. Investigation of unsteady flow-induced impeller oscillations of a single-blade pump under off-design conditions. *Journal of Fluids and Structure*, 35:89–104, 2012.
- [87] A. Presas, D. Valentin, E. Egusquiza, C. Valero, and U. Seidel. Dynamic response of a rotating disk submerged and confined. influence of the axial gap. *Journal of Fluids and Structure*, 62:332–349, 2016.
- [88] D. Ray. Blackout of 2003: Description and responses. *ed. Power Systems Engineering Research Centre (PSERC)*, 2003.
- [89] M. Reclari, M. Dreyer, S. Tissot, D. Obreschkow, F. Wurm, and M. Farhat. Surface wave dynamics in orbital shaken cylindrical containers. *Physics of Fluids*, 26, 5:0521041–11, 2014.
- [90] R. Roy. Turbulent subcooled boiling flow experiments and simulation. *Journal of Heat Transfer*, 124:73, 2002.
- [91] A. Royon, E. Gaudin, A. Cartellier, and E. Hopfinger. Sloshing and drop formation conditions in cylindrical liquid propellant tanks. *Proceeding of the 4th International Conference on Launcher Technology, Liege, Belgium*, 2002.
- [92] A. Royon, E. Hopfinger, and A. Cartellier. Liquid sloshing and wave breaking in circular and square-base cylindrical containers. *Journal of Fluid Mechanics*, 577:477–494, 2007.
- [93] N. Ruchonnet, C. Nicolet, and F. Avellan. Hydroacoustic modeling of rotor stator interaction in francis pump-turbine. *IAHR Int. Meeting of WG on Cavitation and Dynamic Problems in Hydraulic Machinery and Systems*, 2006.
- [94] A. Sauret, F. Boulogne, J. Cappello, E. Dressaire, and H. Stone. Damping of liquid sloshing by foams. *Physics of Fluids*, 27, 2015.
- [95] B. Smirnov and S. Berry. Growth of bubbles in liquid. *Chem Cent Journal*, pages 9–48, 2015.
- [96] W. H. Snyder. Similarity criteria for the application of fluid models to the study of air pollution meteorology. *Boundary-Layer Meteorology*, 3:113–134, 1972.
- [97] W. Soh, Y. Yuen, and B. Khoo. The entrainment of air by water jet impinging on a free surface. *Experiments in Fluids*, 39-1:498–506, 2005.
- [98] Y. Song, K.-A. Chang, Y. Ryu, and S. Kwon. Experimental study on flow kinematics and impact pressure in liquid sloshing. *Experiments in Fluids*, 54(9):1–20, 2013.

## Bibliography

---

- [99] G. Sridhar and J. Katz. Drag and lift forces on microscopic bubbles entrained by a vortex. *Physics of Fluids*, 7:389–399, 1995.
- [100] H. Tanaka, K. Matsumoto, and K. Yamamoto. Sloshing motion of the depressed water in the draft tube in dewatered operation of high head pump-turbines. *Proceedings of the XVII IAHR Symposium on hydraulic machines and cavitation, Beijing, China*, 1:121–130, 1994.
- [101] A. Tassin, C. Li, S. Ceccio, and L. Bernal. Velocity field measurement of cavitating flows. *Experiments of Fluids*, 20:125–130, 1995.
- [102] N. W. Taylor. Diffusion in and through solids. by r. m. barrer. *The Journal of Physical Chemistry*, 46(4):533–534, 1942.
- [103] K. Thomanek, O. Zielinski, H. Sahling, and G. Bohrmann. Automated gas bubble imaging at sea floor - a new method of in situ gas flux quantification. *Ocean Science*, 6:549–562, 2010.
- [104] J. Thomas. Managing relationships between electric power industry restructuring and grid reliability. *Technical workshops on competition and reliability in North American energy markets, Canada: Natural Resources Canada*, 37(1), 2005.
- [105] S. Tissot. *OrbShake Bioreactors for Mammalian Cell Cultures: Engineering and Scale-up*. PhD thesis, EPFL, 2011.
- [106] S. Torii and W. Yang. Melt-particle mixing in gas-stirred ladles with through flow. *Experiments in Fluids*, 20:125–130, 1992.
- [107] Z. Trad, C. Vial, J. Fontaine, and C. Larroche. Mixing and liquid-to-gas mass transfer under digester operating conditions. *Chemical Engineering Science*, 170:606–627, 2017.
- [108] Y. Tsujimoto, Y. Yoshida, Y. Maekawa, S. Watanabe, T., and Hashimoto. Observations of oscillating cavitation of an inducer. *Journal of Fluids Engineering*, 119, 1997.
- [109] O. Uzol, Y. C. Chow, J. Katz, and C. Meneveau. Unobstructed piv measurements within an axial turbo-pump using liquid and blades with matched refractive indices. *Experiments in Fluids*, 33:909–919, 2002.
- [110] E. Vagnoni, L. Andolfatto, and F. Avellan. On the sloshing free surface in the draft tube cone of a francis turbine operating in synchronous condenser mode. *Journal of Physics: Conference Series*, 813(1):012034, 2017.
- [111] E. Vagnoni, L. Andolfatto, R. Guillaume, P. Leroy, and F. Avellan. Rotating air-water ring in the vaneless gap of a pump-turbine operating in condenser mode. *International Journal of Multiphase Flow*, 105:112–121, 2018.

- 
- [112] E. Vagnoni, A. Favrel, L. Andolfatto, and F. Avellan. Experimental investigation of the sloshing motion of the water free-surface in the draft tube of a francis turbine operating in synchronous condenser mode. *Experiments in Fluids*, 59(6):95, 2018.
- [113] D. Valentine and J. Frandsen. Nonlinear free-surface and viscous-internal sloshing. *Journal of Offshore Mechanics and Arctic Engineering*, 127:141–149, 05 2005.
- [114] S. van der Walt, J. Schonberger, J. Nunez-Iglesias, F. Boulogne, J. Warner, N. Yager, E. Gouillart, and T. Yu. scikit-image: image processing in python. *PeerJ* 2:e453, 2014.
- [115] M. Venkatasubramanian. Analyzing blackout events: Experience from the major western blackouts in 1996. ed. *Power Systems Engineering Research Centre (PSERC)*, 2003.
- [116] C. Vessaz, L. Andolfatto, F. Avellan, and C. Tournier. Toward design optimization of a pelton turbine runner. *Structural and Multidisciplinary Optimization*, 55 issue 1:37–51, 2017.
- [117] F. Viola, P. Brun, B. Dollet, and F. Gallaire. Foam on troubled water: capillary induced finite-time arrest of sloshing waves. *Physics of Fluids*, 28:091701, 2016.
- [118] H. Wang, F. Murzyn, and H. Chanson. Interaction between free-surface, two-phase flow and total pressure in hydraulic jump. *Experimental Thermal and Fluid Science*, 64:30–41, 2015.
- [119] K. Yamamoto. *Hydrodynamics of Francis turbine operation at deep part load condition*. PhD thesis, EPFL, 2017.
- [120] A. Zaruba, E. Krepper, H. Prasser, and E. Schleicher. Measurement of bubble velocity profiles and turbulent diffusion coefficients of the gaseous phase in rectangular bubble column using image processing. *Experimental Thermal and Fluid Science*, 29:851–860, 2005.
- [121] J. Zhang, Z. Gao, Y. Cai, H. Cao, Z. Cai, and Y. Bao. Power consumption and mass transfer in a gas-liquid-solid stirred tank reactor with various triple-impeller combinations. *Chemical Engineering Science*, 170:464–475, 2017.
- [122] X. Zhang. An algorithm for calculating water surface elevations from surface gradient image data. *Experiments in Fluids*, 21:43–48, 1996.
- [123] X. Zhou and X. Sun. *Measurement and Modeling of the Liquid-phase Turbulence in Adiabatic Air-water Two-phase Flows with a Wide Range of Void Fractions*. PhD thesis, The Ohio State University, 2014.
- [124] A. Zobeiri. *Investigations of Time Dependent Flow Phenomena in a Turbine and a Pump-Turbine of Francis Type: Rotor-Stator Interactions and Precessing Vortex Rope*. PhD thesis, EPFL, 2009.





**ELENA VAGNONI**

Born in Pesaro (Italy) on April 6<sup>th</sup> 1989.

**Education**

- 2014 – 2018                    **PhD in Mechanics**  
 Laboratory for Hydraulic Machines at EPFL (Switzerland).  
 Thesis: Two-phase flow phenomena in hydraulic turbines and pump-turbines operating in synchronous condenser mode.
- 2011 – 2013                    **M.Sc. in Mechanical Engineering**, Mark: 110/110 *with honors*  
 Politecnico di Milano (Italy)  
 Thesis: An experimental investigation on the flow mechanism causing performance breakdown in cavitating axial turbomachines.
- 2008 – 2011                    **Bachelor Degree in Mechanical Engineering and Diploma ASPRI (Alta Scuola Politecnica)**, Mark: 110/110 *with honors*  
 Politecnico di Milano (Italy)
- 2003 – 2008                    **Diploma in Classical Studies**, Mark: 100/100  
 LICEO MAMIANI (Pesaro, Italy)

**Work experiences**

- 2014 – 2018                    **Doctoral assistant**  
 Laboratory for Hydraulic Machines at EPFL (Switzerland) and General Electric – Renewable Energies, Grenoble (France).
  - Experimental investigation of two-phase flows, free surfaces and air mass transfer in hydraulic machines. Development of post-processing methods for data analysis, imaging and modeling.
  - Teaching activities as assistant in Bachelor/Master classes and supervisor of Bachelor and Master projects.
- 2014 (6 month)                **Scientific assistant**  
 Laboratory for Hydraulic Machines at EPFL (Switzerland).
  - Experimental investigation of the velocity fields and comparison with numerical simulations of a micro-turbine for energy recovery stations in water utility networks for the project DuoTurbo CTI as a member of SCCER-SoE.
- 2014 (1 month)                **Teacher of the Cavitation course**  
 Istituto di Osteopatia mROI, Sesto San Giovanni, Milano (IT)
- 2013 (10 month)               **Visiting graduate student**  
 Laboratory of Fluid Dynamics at Johns Hopkins University (USA)
  - Study on the impact of cavitation on the performance of a marine water-jet pump in the framework of a research project sponsored by the US Office of Naval Research.

**Extra academic experiences**

- 2010 – 2012                    **SHELL ECO MARATHON EUROPE and Formula ATA Electric & Hybrid Italy**  
 Driver of *Apollo* solar vehicle. Politecnico di Milano team *Mecc-Sun*.  
 World record achieved: 1108 km/kWh (equivalent to 9757 km/liter).

## Curriculum Vitae

---

### Training programs

- Oct. 2016      **PhD School 2016 SCCER-SoE/NRP70** (Leukerbad, Switzerland)  
Understanding the transition needed to reach the Energy Strategy 2050
- Oct. 2015      **PhD School 2015 SCCER-SoE/NRP70** (Grimsel Hospiz, Switzerland)  
Reaching the Swiss Energy Strategy 2050 targets for Hydro-power
- Sept. 2015     **Python advance learning** (EPFL, Switzerland)

### Language

Mother tongue: ITALIAN

Professional proficiency: ENGLISH, FRENCH

Limited proficiency: SPANISH, GERMAN

### Awards

- 2013 Scholarship grant awarded by Politecnico di Milano for stages abroad.
- 2012 Scholarship grant awarded by Politecnico di Milano for Master of Science students.

### Peer-reviewed publications

- E. Vagnoni, L. Andolfatto, R. Guillaume, P. Leroy and F. Avellan, "Oxygen diffusion through air-water free surfaces in a pump-turbine operating in condenser mode," submitted to Int. Journal of Multiphase Flow (2018).
- J. Delgado, E. Vagnoni, D.I.C. Covas, F. Avellan, "Assessment of pressure fluctuations induced by off-design operation in a pump running as turbine," submitted to Renewable Energy Journal (2018).
- E. Vagnoni, L. Andolfatto, R. Guillaume, P. Leroy and F. Avellan, "Interaction of a rotating two-phase flows with the torque stability of a reversible pump-turbine operating in condenser mode," submitted to Int. Journal of Multiphase Flow (2018).
- E. Vagnoni, L. Andolfatto, A. Favrel and F. Avellan, (2018), "Experimental investigation of the sloshing motion of the water free-surface in the draft tube of a Francis turbine operating in synchronous condenser mode," Experiments in Fluids, 59(6):95. doi: 10.1007/s00348-018-2552-x
- E. Vagnoni, L. Andolfatto, S. Richard, C. Münch-Alligné and F. Avellan, (2018), "Hydraulic performance evaluation of a micro-turbine with counter rotating runners by experimental investigation and numerical simulation," Renewable Energy Journal 126, 943-953. doi: 10.1016/j.renene.2018.04.015.
- E. Vagnoni, L. Andolfatto, R. Guillaume, P. Leroy and F. Avellan, (2018), "Rotating air-water ring in the vaneless gap of a pump-turbine operating in condenser mode," Int. Journal of Multiphase Flow 105, 112-121. doi: 10.1016/j.ijmultiphaseflow.2018.03.022.
- D Tan, Y Li, I Wilkes, E Vagnoni, RL Miorini, J Katz, (2015), "Experimental Investigation of the Role of Large Scale Cavitating Vortical Structures in Performance Breakdown of an Axial Waterjet Pump," Journal of Fluids Engineering 137 (11), 111301.

**Conference papers**

- E. Vagnoni, L. Andolfatto, R. Guillaume, P. Leroy and F. Avellan, (2018) “Air-Water Ring in the Vaneless Gap of a Reversible Pump-Turbine Operating in Condenser Mode,” 10<sup>th</sup> International Cavitation Symposium (CAV2018), Baltimore USA.
- E. Vagnoni, L. Andolfatto, A. Favrel and F. Avellan, (2017), “On the sloshing free surface in the draft tube cone of a Francis turbine operating in synchronous condenser mode,” *Journal of Physics: Conference Series* 813 (1), 012034.
- E. Vagnoni, L. Andolfatto, C. Münch-Alligné and F. Avellan, (2015), “Experimental evaluation of the velocity profiles and performance of a counter rotating micro-turbine by 2D Laser Doppler Velocimetry,” E-Proceedings of the 6<sup>th</sup> IAHR International Meeting of the Workgroup on Cavitation and Dynamic Problems in Hydraulic Machinery and Systems, Ljubljana, Slovenia.
- E. Vagnoni, L. Andolfatto, J. Delgado, C. Münch-Alligné and F. Avellan, (2015), “Application of Laser Doppler Velocimetry to the development of a counter rotating micro-turbine,” E-proceeding of the 36<sup>th</sup> IAHR World Congress, The Hague, The Netherlands.



